Characterizing dental enamel's mechanical properties from milli- to nanometer length scales

Vom Promotionsausschuss der
Technischen Universität Hamburg-Harburg
zur Erlangung des akademischen Grades
Doktor-Ingenieurin (Dr.-Ing.)
genehmigte Dissertation

von
Siang Fung Ang
aus Penang, Malaysia
2012

Gutachter:

1. Gutachter: Prof. Dr. rer. nat. Gerold A. Schneider (TU Hamburg-Harburg)

2. Gutachter: Prof. Dr. habil. Michael M. Morlock (TU Hamburg-Harburg)

Tag der mündlichen Prüfung: 13. Juli 2012

Abstract

Understanding the structure-property relationship of enamel is a basis to improve restorative and preventive dentistry. This work is the first to systematically characterize enamel according to its hierarchical levels: single crystallite fiber (0^{th} level), multiple crystallite fibers (1^{st} level), multiple rods (2^{nd} level) and bulk enamel (3^{rd} level). Spherical indentation and compression tests were used to characterize enamel's elastic/inelastic transition; the values decrease from 17 GPa to 0.4 GPa with increasing hierarchical levels. This is attributed to increased volume of defects as well as weak phases surrounding each crystallite fiber and rod. Similarly, the elastic moduli were measured as up to 115 GPa for 0^{th} level but 30 GPa for 3^{rd} level.

Both interrod and enamel rod regions showed creep under constant load, a quality to reduce stresses. The measured creep response could be described by a series of creep compliance elements such as spring and dashpot. The inelastic energy dissipation in the interrod regions was found to be statistically significantly higher than in the enamel rod regions, possibly due to higher protein unfolding activities at the protein sheaths.

Sub-10 μm fracture was investigated under AFM and SEM. The mode I crack tip toughness (K_{I0}) was quantified as 0.5-1.6 MPa$\sqrt{m}$ by measuring the crack-opening-displacement (COD) profile under AFM coupled with Irwin's 'near-field' solution. The crack-closure stress at the crack tip was computed as 163-770 MPa with a cohesive zone length and width of 1.6-10.1 μm and 24-44 nm based on the Dugdale-Muskhelishvili (DM) crack model [Dugdale 1960; Goodier and Field 1963; Hahn and Rosenfield 1965; Hahn 1976; Muskhelishvili 1953]. Toughening elements such as crack bridges and microcracks were observed to occur across different length scales: the bridges are from ≈85

nm to ≈3 μm and the microcracks are from 100-500 nm to ≈6 μm. Their formations were fostered by the weak phases surrounding each rod and crystallite fiber as well as the abrupt change of crystallite orientations at the intrarod/interrod boundaries.

Summarized, enamel's elastic moduli and elastic/inelastic transition for 0^{th}-3^{rd} hierarchical levels were quantified. Both enamel rod and interrod regions creep under constant load but the interrod regions are able to dissipate higher irreversible energy compared to the enamel rod regions. The K_{I0}, the bridging stresses and size of the cohesive zone at the crack tip were calculated. Crack bridging and microcracks from micro- to nanometer scales were observed.

References:

- D S Dugdale. Yielding of steel sheets containing slits. J Mech Phys Solids, 8(2):100-4, 1960.
- J N Goodier and F A Field. Fracture of solids. Interscience, New York, 1963.
- G T Hahn and A R Rosenfield. Local yielding and extension of a crack under plane stress. Acta Metall, 13(3):293-306, 1965.
- H G Hahn. Bruchmechanik: Einfuehrung in die theoretischen Grundlagen. Teubner, Stuttgart, 1976.
- N I Muskhelishvili. Some basic problems of the mathematical theory of elasticity. Noordhoff, Gronigen, 1953.

Acknowledgement

This thesis was written mainly based on the outcome of the research project I worked on during my employment at the Institute of Advanced Ceramics, Hamburg University of Technology, Germany. For the sponsor of the research project German Research Foundation (Deutsche Forschungsgemeinschaft) I wish to express my gratitude for their financial support.

My profound appreciation goes to my supervisor, Prof. Dr. rer. nat. Gerold A. Schneider, who is the head of the Institute of Advanced Ceramics for his valuable guidance and also detailed and constructive comments to each of my written works before publications. His support for my participation in various national and international conferences and workshops has helped my exposure to valuable scientific learning and exchanges.

To Prof. Michael V. Swain and Prof. Dr.med.dent. M.S. Arndt Klocke I owe my sincere thanks too. Despite the distances, they have been supportive in providing ideas and concepts for my research. Prof. Dr. Klocke and his contacts have been kind in providing human teeth for the experimental works too. I also warmly thank Prof. Dr. habil. Michael M. Morlock for being the second evaluator of my thesis.

My warm thanks also go to my fellow colleagues in the Institute of Advanced Ceramics for the many fun and enlightening moments. These are especially for Dr. rer. nat. Hans Jelitto, Andrea Engert, Rodrigo Pacher Fernandes, Henry Ekene Mgbemere and Dieter Schmidt for often prompt scientific brainstorming, discussions, equipment constructions and for Sascha Maisel for his proofreading support. Bärbel Rademacher deserves a special mentioning too because she knows the administrative processes by

heart and has been efficient in providing the right support. To my students Emily Lea Bortel, Damien Rembelski, Philip Remmecke, Anja Schulz and Mahnaz Saadatmand I thank them for the valuable mutual learning experiences.

Lastly, my heartfelt gratitude is extended to my family and close friends who have been my major moral support of all times by being there for me despite the ebb or flow. With a warm heart, I dedicate this thesis to them.

Contents

1. Introduction

Enamel is the hard outer coating protecting the soft dentin interior in teeth. It is the hardest part of the human body. These critical load bearing tissues often survive in the oral environment millions of loading cycles in the form of compression, wear and torsion where the critical stress could range up to 2.5 GPa [1]. Its functional success is a desired feature for loading structures. However, a deep understanding of enamel's structure-property relationship is essential before the principles could be applied to advanced structural materials design. Besides, in clinical perspective, a better understanding of enamel's structure-property relationship provides a basis for improvements in restorative as well as preventive dentistry.

Teeth enamel's resilience is also somewhat surprising. 90% by volume of its structure consists of biological apatite crystallites that are as brittle as soda-lime glass (enamel's apatites extracted from de-proteinization have an average fracture toughness of $\approx$1.0 MPa$\cdot\sqrt{m}$ [2] whereas the fracture toughness of soda-lime glass has been measured as 0.7-1.2 MPa$\cdot\sqrt{m}$ [3]), the rest constituents are compliant organics (as soft as skin) and water [4]. After decades of extensive study of their functionality and structure-property relationship [5], it is today still a rather controversial area. Firstly, enamel is traditionally considered as having little chances to deform and its fracture absorbs relatively low energy compared to the underlying dentin [6]. But the fact is that enamel seldom fails catastrophically except in extreme trauma conditions. Recent studies have

even shown that enamel is able to imply toughening mechanisms after crack-initiation [7–9]. Secondly, it is speculated that proteins contribute to energy absorption leading to enamel's toughness [10]. Modeling [11] studies and experimental results from protein molecules in bone [12, 13] support this argument but there is little such microstructure-specific experimental evidence in enamel. Some even claim that the existence of very low amount of enamel proteins 'likely do not play any major structuring function' [14]. Thirdly, calculations show that the levels of hierarchical structure inside the materials does not necessarily correlate to the excellence of mechanical properties [15, 16], whereas some show that tailoring the elementary building blocks at nanoscale is indeed essential for the strength to achieve theoretical values [11]. Lastly, enamel's properties often show a wide variation of values [1].

Therefore, this study is dedicated to improve the fundamental understanding of enamel's structure-property relationship. What are enamel's mechanical properties in relation to its length scales? Does the small amount of proteins play a crucial role in dissipating energy? What is the correlation between enamel's multiple hierarchical levels of structure with its mechanical properties and its role in maintaining the structural integrity? The main characterization tools in this study are nanoindentation and atomic force microscopy.

Although the overall teeth survival could also be due to the synergy of the co-existence between enamel and dentin, the graded junctions between these tissues and/or the shape of the teeth, this study focus to explore the multi-scale properties of enamel itself to understand its secrets of functionality. If enamel itself has not been a high-performing structure, it could not have survived as the outermost coating layer of an important loading structure, teeth.

2. Theoretical Basis

In this chapter, the theoretical basis of the materials, the equipments and the relevant analyses are explained. In Chapter 2.1, the hierarchical structure of enamel, its formation process and its compositions are summarized. The analysis of nanoindetation data is detailed in Chapter 2.2. In Chapter 2.3, the basic principles of fracture mechanics for brittle solids (such as linear elastic fracture mechanics and the non-linear processes around the crack tip) are explained.

2.1. Enamel

A detailed literature review is done to understand the structure, the development process and the compositions of human enamel.

2.1.1. The hierarchical structure of human enamel

A longitudinal section of a human tooth is shown in Fig. 2.1 (a). Enamel rods are closely packed and extend from DEJ to near enamel surface (Fig. 2.1 (b)), estimated to be 6-12 μm below the tooth surface [17]. The rods are embedded in a network of interrod structures (Fig. 2.1 (c)). The diameter of the rods increases from ≈3 μm in the

inner enamel to ≈ 6 µm in the outer enamel [17]. Enamel rods are partially demarcated by organics.

Each rod as well as the interrod regions consist of apatite crystallite fibers of 24-35 nm in thickness and 55-90 nm in width [18, 19]. They have irregular outline (Fig. 2.1 (d) and (e)) as they are pressed against each other during crystallites growth [14]. The crystallites are 40-50 µm long, and some researchers believe that they span over the entire thickness of the enamel layer [14]. Each crystallite is enveloped by an ≈1 nm thick organic layer [18].

The crystallographic axis of the crystallite fibers lies along their longitudinal axis [20], Whereas the orientation of crystallite fibers relative to the rod axis depends on its location around and inside a rod (Fig. 2.2). Within a rod, crystallites are mostly oriented along the rod axis, but the further away their locations from the rod edge with U-shaped organic sheath, the more the deviation of their orientation in comparison to rod axis. This variation of orientation is up to 50 degrees and has been observed in a previous study [21]. The crystallite orientations inside the interrod region are significantly different from the adjacent crystallites inside rods and could deviate to up to 90° [9].

The alternating bright and dark bands in enamel (marked by yellow dotted lines in Fig. 2.1) are called the bands of Hunter and Schreger [22–24]. This optical phenomenon is caused by changes in orientations between adjacent groups of enamel rods (Fig. 2.3). They mainly occur in the inner two thirds of the enamel and are also called rod decussations, where enamel rods bend to the left and right and have different local orientations while extending from DEJ towards the direction of enamel surface.

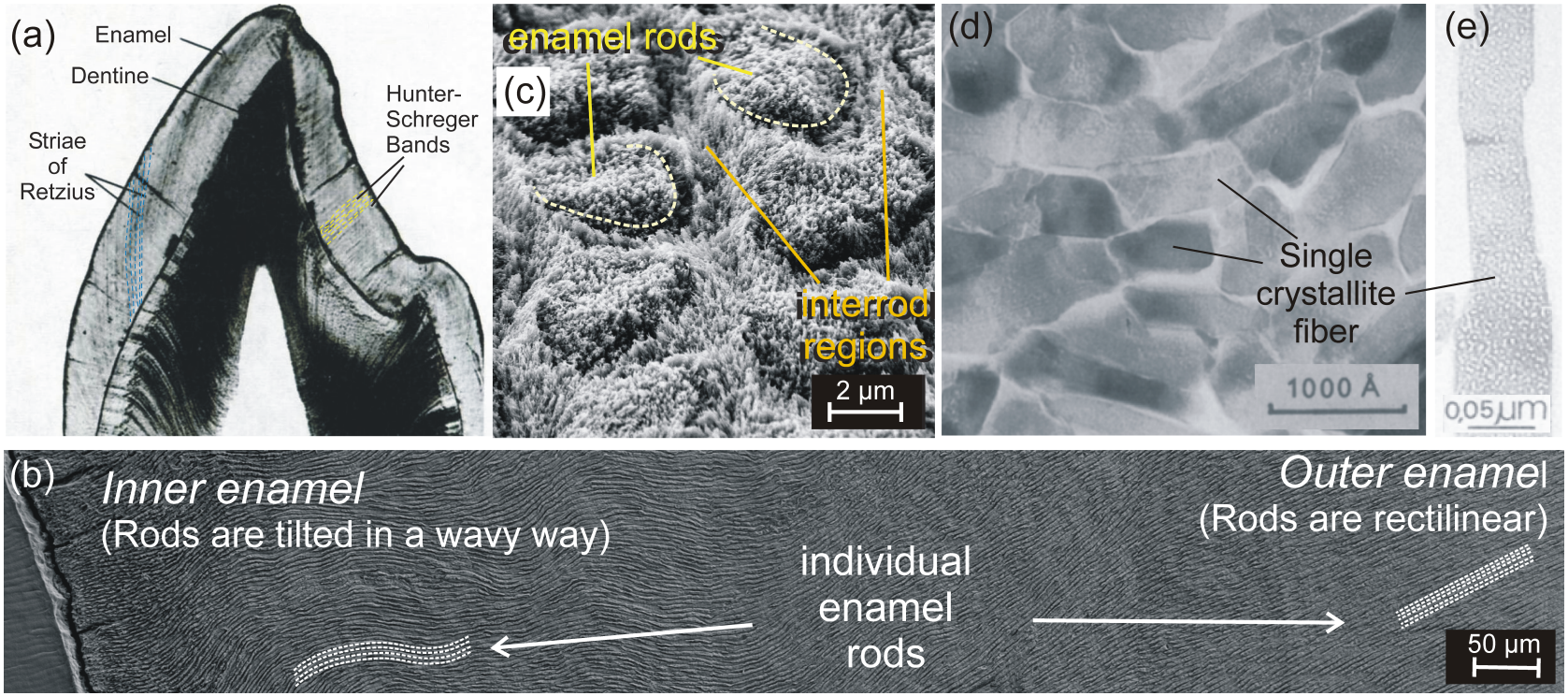

Figure 2.1.: The structure of enamel. (a) A longitudinal section of a tooth and its Hunter-Schreger bands (for magnification, see Fig 2.3) and the lines of Retzius [17]. (b) Enamel rods are closely packed and span from inner enamel to outer enamel region. The rods in the inner region are more intertwoven. (c) The enamel rods and the interrod region. (d) The cross sections of enamel crystallite fibers [18]. (e) Enamel crystallite fibers are at least 100 µm long and have irregular outline [25].

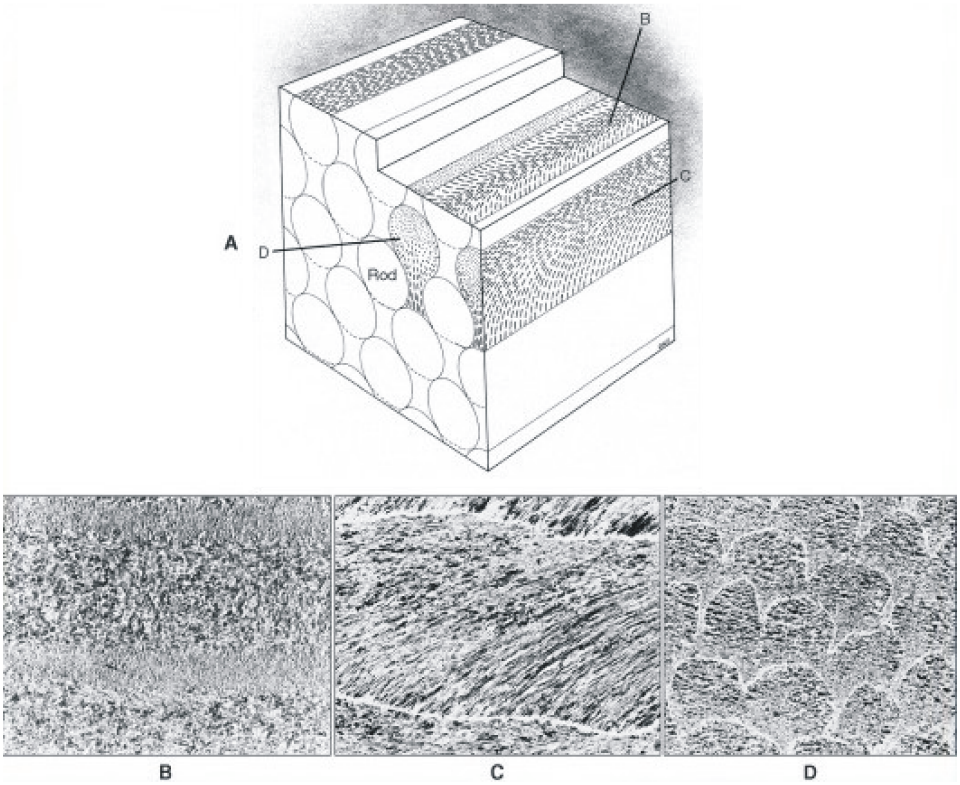

Figure 2.2.: Crystallite fiber orientations inside enamel rods. Figure A shows a 3 dimensional illustration. Figure B-D shows TEM images of the 3 faces in A [14, 21].

The series of dark lines (some are marked by blue dotted lines) in Fig. 2.1 (a) are called the striae of Retzius [26]. These are light microscope manifestation due to rhythmic swelling and shrinking of the rod diameter [17]. These intervals are about 4 μm in width. They are largely attributed to a weekly rhythm in enamel formation [26]; some suggest that each line of Retzius separates different cohorts of cells that are grown side by side [14]. The lines of Retzius end at the enamel surface as shallow trenches known as Perikymata, visible on newly erupted teeth [27].

Since enamel is a hierarchical-structured material, its structure can be described in terms of a 0^{th} to 3^{rd} hierarchical level, where the smaller structural elements compose bigger structural level and so forth [15, 16]. The ≈50 nm diameter apatite crystallite fibers are the mineralized structural elements of the 0^{th} hierarchical level. Groups of

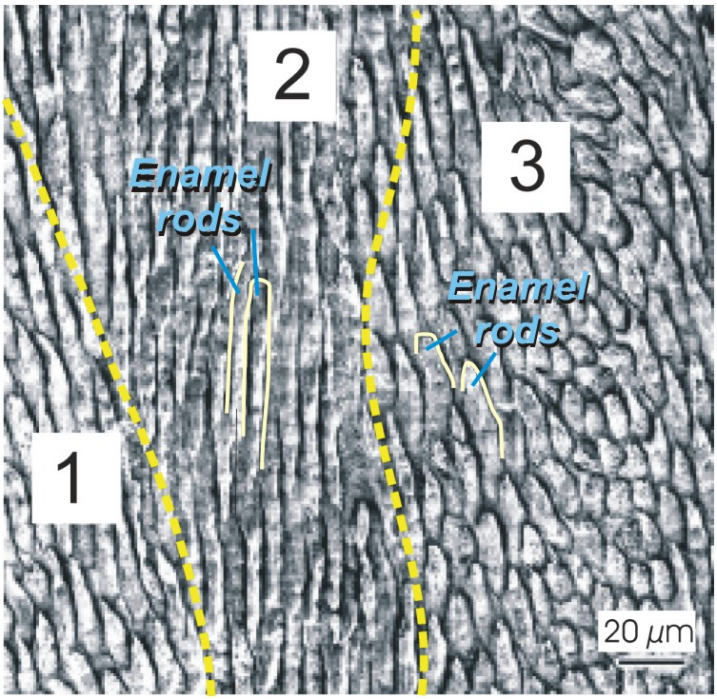

Figure 2.3.: An SEM image illustrates three adjacent Hunter-Schreger bands [14]. Each Hunter-Schreger band represents a group of enamel rods of similar local orientation but different from those in the adjacent Hunter-Schreger bands.

apatite crystallite fibers are bundled together within one enamel rod or in the interrod region as the 1st hierarchical level. The enamel rods are grouped to form the 2nd level in Hunter-Schreger bands in the inner enamel rod region. The rods within each band have the same local orientation but different from the orientation of enamel rods inside the adjacent Hunter-Schreger bands. Multiple Hunter-Schreger bands form the 3rd hierarchical level as bulk enamel.

2.1.2. Enamel formation

This section is summarized from Chapter 7 - Enamel: Composition, Formation and Structure in the book Ten Cate's Oral Histology by Antonio Nanci [14]. In this chapter, italic forms are used for all scientific terms relevant to enamel formation because these are generally non-familiar terms for materials scientists.

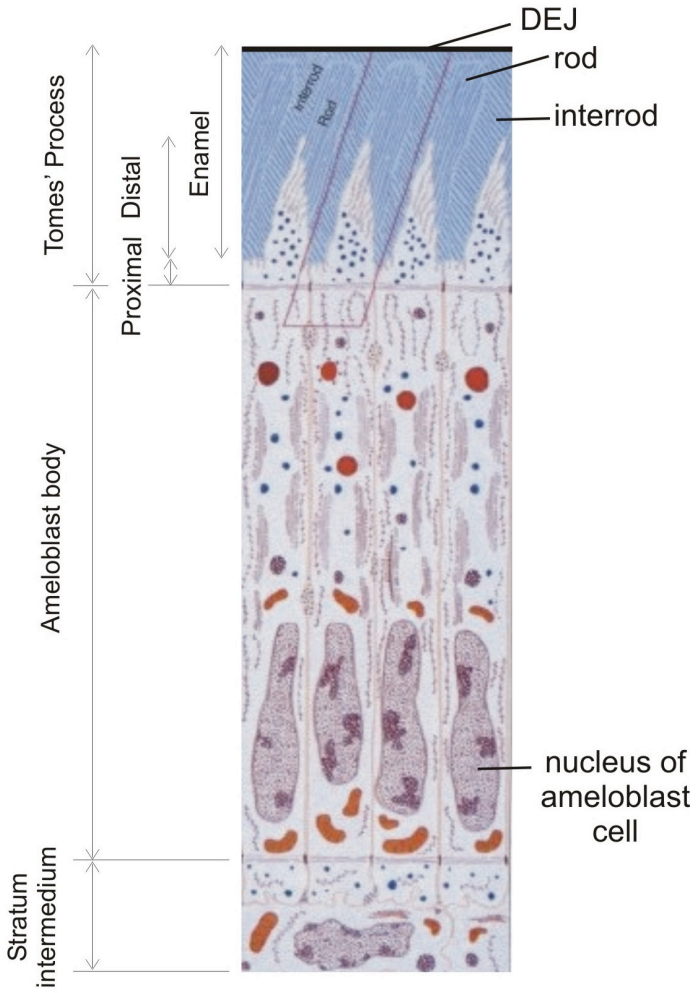

Figure 2.4.: A schematic representation of four ameloblast cells in a section along their long axis, showing (from bottom to top) stratum intermedium (believed to be closely related to the development of ameloblasts), ameloblasts' bodies, ameloblasts' proximal portion of Tomes' Process (ppTP), ameloblasts' distal portion of Tomes' Process (dpTP) and the growing enamel layer. [14].

The process of enamel formation is called *amelogenesis*. *Ameloblasts* are cells from which tooth enamel develops. *Ameloblasts* (Fig. 2.4) are compartmentalized into body and *Tomes' process*. Mineral deposition is accomplished at Tomes' Process and begins at the dentinoenamel junction (DEJ) and ends at the outer enamel, constantly pushing the *ameloblasts* away from the DEJ. The non-secreting end of ameloblast cells are attached to the *stratum intermedium*. Crystallite formation is accompanied by enamel protein secretion (discharge) out of *ameloblasts* and are segregated at two sites: (i) around the

periphery of the *ameloblasts* on the *ppTP* (proximal portion of Tomes' Process) and (ii) along the face of the *dpTP* (distal portion of Tomes' Process) (Fig. 2.4). The crystallites growth at *ppTP* forms *interrod* regions whereas those at *dpTP* forms *rods*. The formation of initial and final enamel layers are formed by the *ppTP* surfaces only (without *dpTP*) and therefore contain no enamel rods. After crystallite formation, enamel then hardens by the growth in width and thickness of pre-existing crystallites while the matrix proteins and enamel fluid diminish (maturation stage). During the maturation stage, no new crystallites are formed.

The proteins identified in enamel include *ameloblastins*, *enamelins*, *amelogenins* (90% of the proteins), *tuftelins*, *enamelysin*, *KLK4*, *amelotin* and *Apin*.

Based on the biochemical characteristics, enamel proteins *ameloblastin* and *enamelin* are believed to guide the formation of enamel crystals. They undergo rapid extracellular processing and have short half lives. Therefore, their small amount does not necessarily mean that they are produced in small amounts but might actually mean that they do not accumulate over long periods. Those found in the deeper enamel are mostly degraded fragments whereas those near enamel's surface are more intact.

Amelogenin makes up 90% of enamel proteins. They are believed to form 'nanospheres' surrounding crystallites along their axis. Based on the biochemical characteristics and their distribution, they are believed to regulate growth in thickness and width of crystallites. They are hydrophobic and are rich in *proline*, *histidine* and *glutamine*. They undergo extracellular processing by enzymes into smaller fragments, *tyrosine*- and *leucine*-rich *amelogenin* polypeptide comprises the bulk of the final organic matrix.

Enamelysin and *KLK4* are involved in the extracellular processing and degradation of the enamel matrix. *Enamelysin* is involved in the short-termed processing of the newly secreted matrix, whereas *KLK4* acts as a digestive enzyme especially during the

maturation stage. The role of *tuftelins* in the enamel matrix is still unclear.

The enamel proteins *amelotin* and *apin* are associated with the modulating surfaces between ruffled-ended and smooth surfaces of *ameloblasts* during maturation stage. The cyclic modulations between creation, decline and recreation of a ruffle-ended borders or smooth surfaces of *ameloblasts* is hypothesized to maintain good pH conditions for mineralization and matrix degrading processes.

Amelogenesis can take as long as 5 years to complete, and about two thirds of the formation time is dedicated to the maturation stage. After the maturation stage, the tooth awaits eruption through gum bed into the oral cavity.

2.1.3. Compositions of human enamel

Human enamel contains ≈96% by weight of mineral [28], individual values range from 93.6-98.5% [29–39]. 0.05-8% of its composition is organic matters [35, 39–47], averaging at approximately 0.5% [28]. The rest of the composition is water. By taking the density of minerals, organic matters and water as 3.0, 1.4 and 1.0 g/cm^3, the % by volume for these constituents are calculated as 90%, 2% and 8% (Tab. 2.1) [4, 28].

Table 2.1.: Approximate content of main constituents of sound human enamel [4, 28].

Constituent	**% by weight**	**Density (g/cm^3)**	**% by volume**
Mineral	96	3.0	90
Organic matter	1	1.4	2
Water	3	1.0	8

2.1.3.1. Minerals

The major elements in human enamel is calcium and phosphorus; it also contains carbonate, sodium, magnesium, chlorine and potassium [29, 30, 33, 35, 37, 39–41, 43, 48–63] (Tab. 2.2) . Up to 40 trace elements were detected in human enamel including strontium, zink, sulfur, silicon, aluminium and fluorine [28].

Table 2.2.: Approximate content of major and minor inorganic constituents of sound human enamel (% by weight) [28].

Constituent	**Concentration range** (% by weight)	**Average** (% by weight)
Ca	34.6 - 38.2	36.6
P	16.3 - 19.2	17.7
CO_3	2.4 - 4.2	3.2
Na	0.17 - 1.16	0.67
Mg	0.04 - 0.68	0.35
Cl	0.16-0.7	0.35
K	0.018 - 0.1	0.04

It is very common in the literature to equate the mineral in enamel to the synthetic hydroxyapatite with a stoichiometric chemical formula $Ca_5(PO_4)_3OH$ with a molar ratio of Ca/P=1.67. However, strictly speaking, enamel's inorganic component has a range of Ca/P ratio of 1.8-2.3 and contains a significant amount of other minor elements (Tab. 2.2). More importantly, recent analysis [64, 65] showed that the hydroxyl content (OH^-) in biological apatite (from bone) is just 0-20% of those in synthetic stoichiometric hydroxyapatite. Therefore, it is inappropriate to name the mineral in enamel as 'hydroxapatite'. The name 'apatite' is however acceptable. High resolution TEM images observed sets of lattice striations with 8.17 Å intersecting at 60 ° angles in enamel crystallites, indicating its crystal structure composed of accumulated rhombic unit cells

[66].

The mineral in enamel is sometimes called carbonated apatite. It is worth mentioning that the exact configuration of the carbonate substitution into the crystallite structure is a controversial topic. A critical review by Leventouri showed that the present proposed model of carbonate substitution in the lattice of B-type carbonate hydroxyapatites remains unresolved because the proposed carbonate substitution models resulted from a limited number of samples [67]. Additional experiments on biological and synthetic apatites are necessary to determine the exact crystal structure of minerals in enamel.

2.1.3.2. Organic matters

Sound human enamel contains only ≈1% of organic matter by weight. Of these, ≈57% are peptides/proteins and ≈43% are lipids [68]. Proteins, which are also known as polypeptides are organic compounds made of amino acids arranged first in linear chains (primary structure), which further form secondary, tertiary and quaternary structures. Lipids are molecules including fats, waxes and sterols among others.

Researchers have not successfully investigated the sequence of amino acids in enamel, let alone of their architecture at secondary and tertiary level. This is due to the difficulties of sample preparation of very small amount of organic matter from enamel. Several studies have attempted to characterize the proteins in enamel. The types of acid amino determined are mainly proline, glycine, glutamic acid, histidine and leucine [42, 69–73]. Hydroxyproline is also detected in mature enamel which is believed to be indicative of the presence of collagen type I [74].

2.1.3.3. Water

It is generally agreed that two types of water exists in human enamel, loosely bound water and firmly bound water [28].

The loosely bound water is presumed to occur in the pores, adsorbed on the crystallite surfaces, and is associated with organic matrix [75–78]. It can be nearly reversibly removed by heating at 100-140 °C or exchanged with etanol or D_2O [35, 38, 40, 48, 77–80]. Such loss has no significant effect on the crystallographic properties of mineral. The published values of loosely bound water are 0.3-3.5% by weight, averaging at approximately 1.3% [35, 36, 38–40, 48, 75–77, 79–83]. It has been shown that determination of the content of loosely bound water is highly influenced by the experimental condition such as relative humidity, temperature and pressure [83].

Heating above 150 °C causes an irreversible loss of firmly bound water [38, 40, 76–79, 81, 84]. The loss of firmly bound water causes changes in crystallographic properties [37, 48, 77, 85] and therefore is believed to associate with mineral itself [35, 40, 48, 76, 77, 81]. Since heating above 150 °C might cause loss of other materials too, the reported values of 1.3-3.5% by weight [35, 38, 40, 75–77, 79–81] should be considered as an upper estimate [28]. The firmly bound water could occur in the form of HPO_4^{2-} (structurally incorporated water) or OH^- (constitutional water) ions [28]. The structural water is estimated at 1-2% [77, 80].

2.1.4. Bovine enamel

Bovine enamel were used to substitute human enamel in some studies due to their structural similarities [86, 87]. For instance, AFM and electron microscopy characterization show that the rod and crystallite fiber diameters do not have significant discrepancy

from those in human enamel [88, 89]. The diameter of bovine enamel rod ranges from 3.7-8.8 μm and the diameter of the crystallite fiber is ≈50 nm [88, 89]. Detailed microstructure of bovine enamel are available in the long article of Glimcher et al. [89]. Even the gradual change of crystallite fiber orientation within one enamel rod in bovine enamel is very similar to human enamel.

2.2. Analysis of Nanoindentation Data

In nanoindentation tests, a force-controlled loading profile can be applied. An example of a loading curve is shown in Fig. 2.5 (a). The recorded data are force (P), penetration depth (h_t) and time (t). An example of a resulted load-penetration curve is shown in Fig. 2.5 (b). The recorded data can be used to calculate the elastic modulus, hardness, indentation stress-strain curve, energy dissipation, creep and stress relaxation, as outlined in the following subtopics.

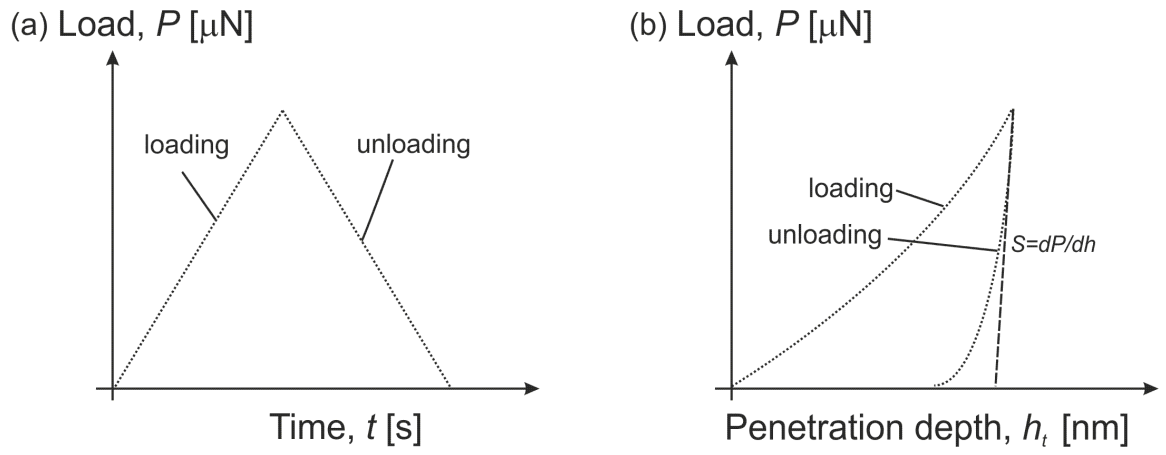

Figure 2.5.: (a) A nanoindentation P-t loading profile and (b) the resulted P-h_t curve.

2.2.1. Elastic modulus and hardness

Although Berkovich geometry tip is widely used in the field of nanoindentation, its triangular-shaped tip can only produce constant equivalent strain value [90]. A spherical indenter has the advantage that the indentation strain increases with the penetration depth [90]. Fig. 2.6 shows a schematic diagram of a spherical indenter in contact with a specimen surface. The projected indentation contact area A can be related to the indentation radius a, the indenter radius R and the contact depth h_c with

$$A = \pi a^2 = \pi \left(2Rh_c - h_c^2\right). \tag{2.1}$$

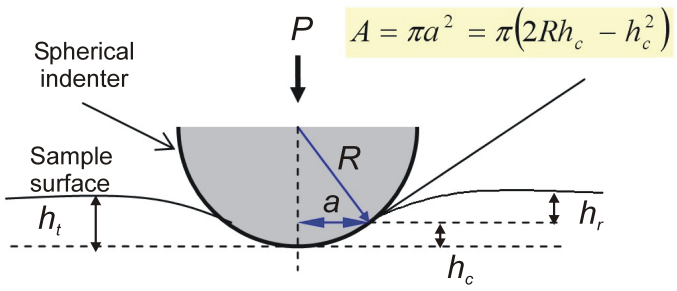

Figure 2.6.: A schematic diagram of an elastic contact between an ideal stiff spherical indenter and the surface of an indented specimen.

The elastic contact of a spherical indenter on an elastically isotropic material can be described by [91]:

$$h_t = \left(\frac{9}{16}\right)^{1/3} \left(\frac{P}{E_r}\right)^{2/3} \left(\frac{1}{R}\right)^{1/3}, \tag{2.2}$$

with h_t the total penetration depth, P the applied load, E_r the reduced elastic modulus.

The indenter radius of a spherical indenter can be calculated by doing indentation on a standard materials with known E_r (for example a fused quartz). The measured

data can be used to plot h_t versus $P^{2/3}$. The initial regime of the curve will be linear if two conditions are fulfilled - the material is still elastic and the tip of the indenter is spherical. Therefore, if the initial portion of the h_t versus $P^{2/3}$ is linear, the slope could be used to calculate R, which is a useful method for spherical indenter tip calibration. The indenter with the known radius can then be used to probe a material with unknown properties. Plotting the h_t versus $P^{2/3}$ of the initial loading curve will lead to a linear curve as long as the contact is elastic. The slope can be subsequently be used to calculate the E_r of that material.

Oliver and Pharr [92] showed that E_r can also be calculated from the unloading curve. Firstly, the initial portion of the unloading curve in Fig. 2.5 is fitted to calculate the stiffness S as

$$S = \frac{dP}{dh}. \tag{2.3}$$

The residual depth h_r in Fig. 2.6 for a paraboloid indenter (whose behavior is the same as that of a spherical indenter in the limit of small displacements) can be estimated as

$$h_r = \frac{3}{4}\frac{P_{max}}{S}. \tag{2.4}$$

The contact depth h_c is

$$h_c = h_t - \frac{3}{4}\frac{P_{max}}{S}. \tag{2.5}$$

For a spherical indenter of known R, the h_c can be used to calculate A from Eq. (2.1). E_r can then be calculated by

$$E_r = \frac{S}{2}\sqrt{\frac{\pi}{A}}. \tag{2.6}$$

E_r for the unloading curve of a spherical indentation can alternatively be calculated as follows [93]. When a spherical indenter is unloaded from the maximum applied load, the indenter is unloaded elastically from a spherical impression. Eq. (2.2) can be used to fit the unloading curve in Fig. 2.5. By plotting h_t vs $P^{2/3}$, the slope Q can be derived. Differentiating the equation $h_t = QP^{2/3}$ gives $dh_t/dP = (2/3)QP^{-1/3}$. By inserting the P as the load upon unloading and the derived Q, the stiffness $S = 1/(dh_t/dP)$ can be calculated. Subsequently, the h_c and E_r can be calculated from Eq. (2.5) and Eq. (2.6) respectively.

The elastic modulus of the specimen can be calculated by considering the compliance of the specimen and the indenter tip combined in series,

$$\frac{1}{E_r} = \frac{(1-\nu_i^2)}{E_i} + \frac{(1-\nu_p^2)}{E_p} \tag{2.7}$$

where E_i, ν_i and E_p, ν_p are elastic moduli and poisson's ratio of the indenter and specimen respectively.

The hardness, H is defined as the resistance against plastic deformation. For materials loading beyond its elastic/inelastic transition, H can be calculated by

$$H = \frac{P_{max}}{A}. \tag{2.8}$$

Often, the shape of the indenter can be pre-calibrated with a standard material, for example fused quartz to get a function of the area versus contact depth (A=f(h_c)) described in the reference [92]. Therefore, while the indenter radius is unknown, the

stiffness fitted from the unloading curve and the recorded h_t can be used to calculate h_c according to Eq. (2.5). The h_c can be used to calculate A from the calibrated function of A=f(h_c). Subsequently, E_r and H can be calculated from Eq. (2.6) and (2.8). With available calibrated $A - h_c$ functions, the calculation of E_r and H can usually be calculated with a single click on the commercial nanoindentation software and is commonly called 'Oliver-Pharr method' [92].

2.2.2. Indentation stress-strain curve

In the elastic regime of spherical indentation, which is usually the case for the onset of loading [94]:

$$h_c = \frac{h_t}{2} \tag{2.9}$$

With the known indenter radius, the indentation area A can be calculated from Eq. (2.1). According to Tabor [95], the indentation stress is represented by the mean contact pressure, P_m:

$$P_m = \frac{P}{A}. \tag{2.10}$$

By assuming $h_t \ll R$, substituting Eq. (2.1) (2.2) and (2.9) into Eq. (2.10) gives for the elastic regime

$$P_m = \left(\frac{4E_r}{3\pi}\right)\frac{a}{R}. \tag{2.11}$$

Hence, plotting P_m versus a/R can be interpreted as indentation stress-strain curve (Fig. 2.7). The slope of the first linear region can be used to calculate E_r. The point when the curve starts to deviate from the linear stress-strain relationship is named

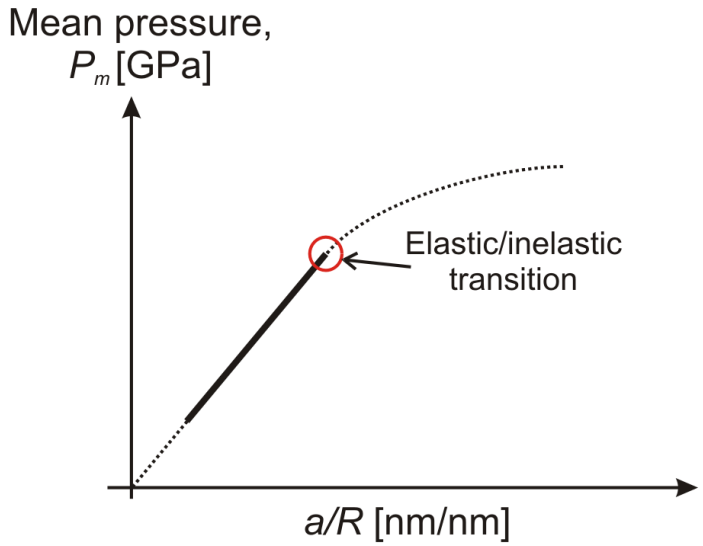

Figure 2.7.: An indentation stress-strain curve. The stress when the curve deviates from the initial linear relationship is named 'elastic/inelastic transition'.

'elastic/inelastic transition' (Fig. 2.7).

From Eq. (2.7), if we neglect the term $(1-\nu_i^2)/E_i$ as it is ≈10 times smaller than in the $1/E_r$, E is within ±10% of E_r for 20 GPa$<E_r<$120 GPa and $0.23<\nu<0.28$. Therefore in our case it is justified to approximate $E \approx E_r$ in Eq. (2.11). This gives

$$P_m \approx E\left(\frac{4}{3\pi}\right)\frac{a}{R} \tag{2.12}$$

and we identify the indentation strain as

$$\text{Indentation strain} \approx \left(\frac{4}{3\pi}\right)\frac{a}{R} \tag{2.13}$$

This is different to the definition used for metals [95] where

$$\text{Indentation strain} \approx 0.2\frac{a}{R} \tag{2.14}$$

To avoid the ambiguity arising from the definition of indentation strain, the indentation stress-strain curves throughout this article are plotted as P_m versus a/R.

2.2.3. Energy dissipation

The calculation of energy dissipation from a nanoindentation curve is described previously by He and Swain [96]. The mechanical work done is the product of applied force and the resultant displacement. Therefore, the area under the loading curve and the dwell period until point B (Fig. 2.8) corresponds to the total mechanical work done to the sample during the indentation, U_T. Similarly, the area under the unloading curve corresponds to the elastic energy, U_E recovered from the work. The inelastic energy dissipation, U_{Inel}, can be calculated from the difference between the U_T and U_E (which is the area covered inside the loading, the dwell region and the unloading curves):

$$U_{Inel} = U_T - U_E \tag{2.15}$$

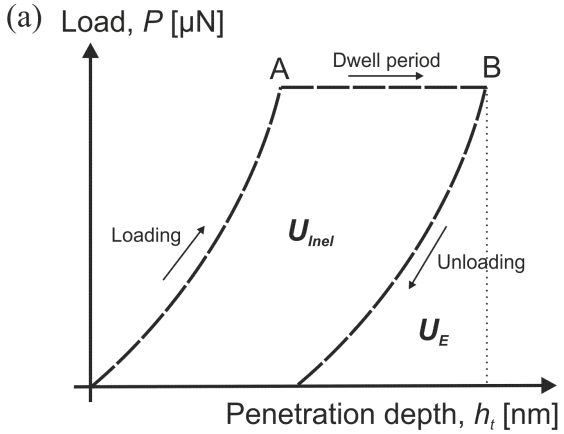

Figure 2.8.: A schematic drawing of the$P$-h_t curve for nanoindentation. The loading profile includes a dwell region from A to B by holding at a constant load. The areas representing U_E, the elastic energy recovered and U_{Inel}, the inelastic energy dissipated are shown too.

The '*Inelasticity index*' is defined as the ratio of the inelastic to total energy for an indentation [96] by

$$Inelasticity\ index = \frac{U_{Inel}}{U_T} \cdot 100\% \tag{2.16}$$

2.2.4. Creep

Creep here refers to the displacement induced during holding at maximum load in Fig. 2.8. For similar stress levels, this creep response can be used to compare the resistance of materials against time-dependent indentation deformation.

2.2.5. Creep compliance

The mathematical problem of creep response during indentation is solved in reference [94, 97, 98]. For a constant load holding after a step change of load from 0 to P_{max},

$$h_t^{\frac{3}{2}} = \frac{3}{8\sqrt{R}} P_{max} J(t) \tag{2.17}$$

with $J(t)$ the creep compliance function. Viscoelastic deformation can be modeled as a spring (that describes elastic deformation), in series with a slider (instantaneous inelastic deformation), a dashpot (viscoplastic process) and one or more Kelvin-Voigt bodies (a spring parallel with a dashpot) (viscoelastic processes) (Fig. 2.9). The corresponding compliance function $J(t)$ [99] is

$$J(t) = C_0 + c_v t + \sum_{j=1}^{n} C_j \left[1 - exp\left(-\frac{t}{\tau_j}\right)\right] \tag{2.18}$$

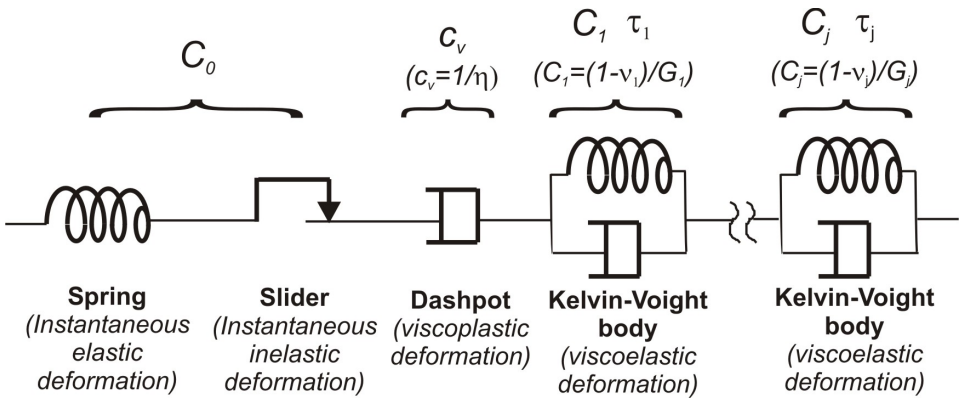

Figure 2.9.: The material's deformation of the dwell region in (a) can be modeled by several elements connected in series: a spring, a slider, a dashpot and Kelvin-Voigt bodies. The parameters involved are compliance C_0 (which is a function of both instantaneous elastic and inelastic responses), c_v ($1/c_v$ gives the viscosity of the dashpot η), and the compliance and time constants of Kelvin Voigt bodies C_j, τ_j ($C_j = \frac{1-\nu_j}{G_j}$).

with C_0 the compliance constant that is related to the elastic and inelastic instantaneous behavior elastic modulus and hardness ($C_0 = f(E, H)$) , c_v the viscosity η with $c_v = 1/\eta$, C_j and τ_j are compliance constants and the retardation time of the j$^{\text{th}}$ Kelvin-Voigt body. C_j can be related to the shear moduli G_j and Poisson's ratio ν_j by $C_j = \frac{1-\nu_j}{G_j}$.

An instantaneous step change of load from 0 to P_{max} is difficult to realize. Usually, the load must be increased from 0 to P_{max} by applying a ramp loading at constant loading rate. Therefore, a ramp correction factor, ρ_j [98] is included into the Kelvin-Voigt bodies in Eq. (2.18) where

$$\rho_j = \frac{\tau_j}{t_R}\left[exp\left(\frac{t_R}{\tau_j}\right) - 1\right] \tag{2.19}$$

with t_R the time for the load to increase from $P = 0$ to P_{max}.

Similarly, the term $c_v t$ in Eq. (2.18) for dashpot is modified as $c_v(t - t_R/2)$, assuming the indenter penetration during the t_R equals to the indenter penetration that resulted from an average force of $P_{max}/2$. Therefore, the creep compliance function for

a ramp-hold indentation testing can be described by

$$J(t) = C_0 + c_v\left(t - \frac{t_R}{2}\right) + \sum_{j=1}^{n} C_j\left[1 - \rho_j exp\left(-\frac{t}{\tau_j}\right)\right],\ j = 1,\ 2, ...\ n... \tag{2.20}$$

Summarized, the time-dependent response for a spherical indentation's dwell period in Fig. 2.8 can be approximated by a combination of a spring, a slider, a dashpot and one or more Kelvin-Voigt bodies connected in series (Fig. 2.8) as [99]

$$h_t^{\frac{3}{2}} = \frac{3P_{max}}{8\sqrt{R}}\left(C_0 + c_v\left(t - \frac{t_R}{2}\right) + \sum_{j=1}^{n} C_j\left[1 - \rho_j exp\left(-\frac{t}{\tau_j}\right)\right]\right)\ \ j = 1,\ 2, ...\ n... \tag{2.21}$$

2.2.6. Stress relaxation

The data for the dwell period in Fig. 2.8 can be used to calculate stress relaxation behavior. Firstly, the stiffness, S upon unloading at point B in Fig. 2.8 can be calculated, as described under Section 2.2.1. h_c can then be calculated according to Eq. (2.5). It has been previously shown that the ratio of the h_c and h_t for enamel is almost a constant [100]. Therefore, the ratio of the h_t/h_c at point B in Fig. 2.8 is calculated and is used to estimate h_c for every data point for the dwell period based on the known h_t . The indentation area is then calculated based on Eq. (2.1). The mean pressure, P_m is calculated by (2.10)

Although the load is constant during the dwell period in Fig. 2.8, the increase in indentation area leads to a change of P_m. A possibility to perform fitting for the relation of P_m versus t is by using the Kohlrausch-Williams-Watts (KWW) model [100, 101]

$$P_m(t) = P_{m0} \cdot exp\left[-\left(\frac{t}{\tau}\right)^{\beta}\right] \tag{2.22}$$

KWW model is an empirical decay function which is used to describe the relaxation of a material property [102]. $P_m(t)$ is the value of P_m at time t, starting with the maximum value of the instantaneous stress P_{m0} at $t = 0$. The effective relaxation time constant τ is the dimension with the parameter of time, the larger the τ, the longer the system needs before it reaches equilibrium. β is the power law component with values in the range of $0 \leq \beta \leq 1$ that describes the deviation of the system from the usual exponential function. The smaller the β, the more stretched is the decay function horizontally. When β=1, the usual exponential function is recovered and the model is called Debye or Maxwell (DM) relaxation model [103]

$$P_m(t) = P_{m0} \cdot exp\left[-\left(\frac{t}{\tau}\right)\right] \tag{2.23}$$

2.3. Fracture Mechanics

This section presents some basics of fracture mechanics of brittle solids. Analytical solutions used to describe the stress distribution and displacement around a crack tip of an ideal isotropic Hookean material are outlined. The cohesive zone model that describes the non-linear process at the crack tip is also presented.

2.3.1. Linear elastic fracture mechanics

Fracture mechanics is used to predict how or whether a crack in a material grows under an applied stress. A classic paper by Griffith in 1921 served as a breakthrough of

the theory of fracture mechanics [104]. Griffith realized that the fracture of glass involves a fracture strength much lower than the theoretical stress needed to break the atomic bonds, and that the breaking stress of glass fibers is not a constant value but increases with decreasing fiber diameter. He proposed that pre-existing flaws (or cracks) in the material as the reason of the low and variable experimental fracture strength values. The applied stress is concentrated at the crack tip and breaks the local atomic bonds; this process involves the conversion of the elastic energy to surface energy when new crack surface is created [104]. Griffith experimentally verified the following equation on glass [104]:

$$\sigma_f \sqrt{a} = \sqrt{\frac{2E\gamma}{\pi}} \tag{2.24}$$

where σ_f is the fracture strength, $2a$ is the length of the initial flaw introduced to the specimen, E the elastic modulus of the specimen and γ is the surface energy.

Griffith's work received very little attention by the engineering community until the early 1950's for the following reason: (i) For usual structural material such as steel, the fracture energy is orders of magnitude higher than γ (ii) Many usual structural materials demonstrate noticeable plastic deformation at the crack tip that makes the assumption of a linear elastic medium at the crack tip unrealistic [105]. These led Irwin [106] and Orowan [107] independently to propose that the γ term in Eq. (2.24) should be replaced with the fracture energy Γ where

$$\Gamma = 2\gamma + w_p \tag{2.25}$$

with w_p the dissipative energy due to plastic deformation.

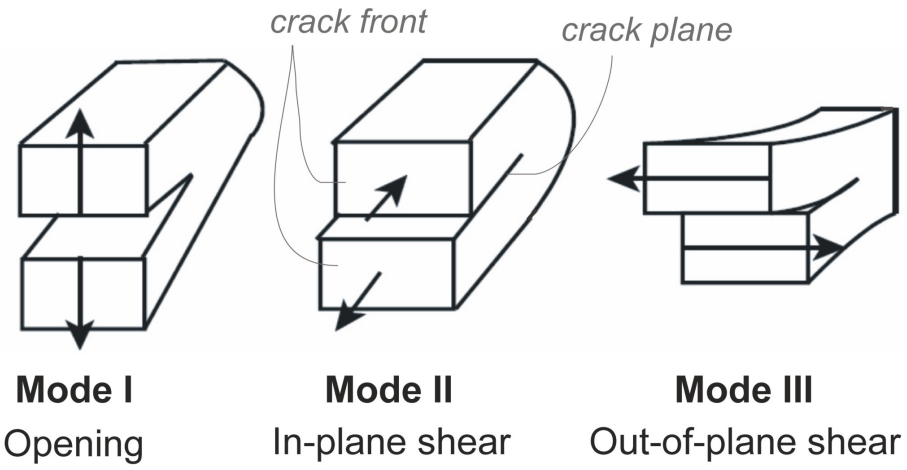

Figure 2.10.: The three fracture modes.

Another important contribution of Irwin is his introduction of the concept of a stress intensity factor K to predict the stress state near a crack tip caused by remote stresses [108]. Before we proceed to the analytical solutions developed by Irwin where K appeared, it is useful to first present three basic modes of fracture (Fig. 2.10) [109, 110]. Mode I fracture is a tensile mode separation where the traction forces act to open crack surfaces directly apart from each other. Mode II fracture is a shear mode separation where the traction forces are parallel to the crack plane but perpendicular to the crack front. Whereas mode III fracture is a shear mode separation where the traction forces act parallel to the crack plane and also parallel to the crack front. The stress intensity factors for mode I II and III crack are designated as K_I, K_{II} and K_{III} respectively.

For an ideal isotropic Hookean material, Irwin's 'near-field' solutions have been developed as analytical solutions to describe the stresses (σ_{ij}) and displacements (u_i) around a tip of a slit-like crack subjected to a remote applied load σ_A (Fig. 2.11) with a key assumption that the crack walls behind the crack tip are free of other tractions such as crack bridging, or that region behind the crack tip which is subjected to closure stress is reasonably small in comparison to the other dimensions [109, 110]. Irwin crack-tip

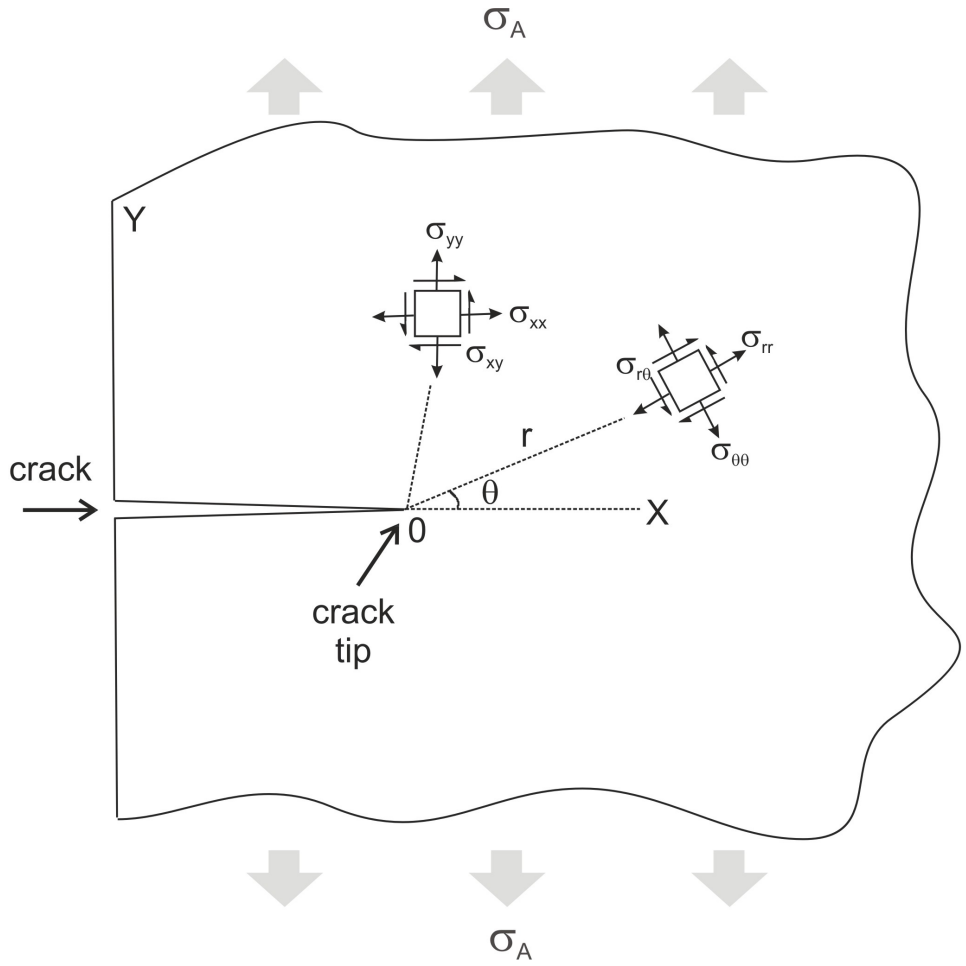

Figure 2.11.: 2-D stress tensor in polar and Cartesian coordinates centered at a slit-like crack tip.

solutions for an isotropic homogeneous material of the three fracture modes in relation to the coordinate system shown in Fig. 2.11 are listed below ($K_{I,II,III}$ are stress intensity factors of mode I, II or III cracks, E is the elastic modulus, ν is the poisson's ratio [109, 110]):

Mode I:

$$\begin{Bmatrix} \sigma_{xx} \\ \sigma_{yy} \\ \sigma_{xy} \end{Bmatrix} = \frac{K_I}{\sqrt{2\pi r}} \begin{Bmatrix} cos(\theta/2)[1 - sin(\theta/2)sin(3\theta/2)] \\ cos(\theta/2)[1 + sin(\theta/2)sin(3\theta/2)] \\ sin(\theta/2)cos(\theta/2)cos(3\theta/2) \end{Bmatrix} \tag{2.26a}$$

$$\begin{Bmatrix} \sigma_{rr} \\ \sigma_{\theta\theta} \\ \sigma_{r\theta} \end{Bmatrix} = \frac{K_I}{\sqrt{2\pi r}} \begin{Bmatrix} cos(\theta/2)[1 + sin^2(\theta/2)] \\ cos^3(\theta/2) \\ sin(\theta/2)cos^2(\theta/2) \end{Bmatrix} \tag{2.26b}$$

$$\sigma_{zz} = \nu'(\sigma_{xx} + \sigma_{yy}) = \nu'(\sigma_{rr} + \sigma_{\theta\theta}) \tag{2.26c}$$

$$\sigma_{xz} = \sigma_{yz} = \sigma_{rz} = \sigma_{\theta z} = 0 \tag{2.26d}$$

$$\begin{Bmatrix} u_x \\ u_y \end{Bmatrix} = \frac{K_I}{2E}\sqrt{\frac{r}{2\pi}} \begin{Bmatrix} (1+\nu)[(2\kappa - 1)cos(\theta/2) - cos(3\theta/2)] \\ (1+\nu)[(2\kappa + 1)sin(\theta/2) - sin(3\theta/2)] \end{Bmatrix} \tag{2.26e}$$

$$\begin{Bmatrix} u_r \\ u_\theta \end{Bmatrix} = \frac{K_I}{2E}\sqrt{\frac{r}{2\pi}} \begin{Bmatrix} (1+\nu)[(2\kappa - 1)cos(\theta/2) - cos(3\theta/2)] \\ (1+\nu)[-(2\kappa + 1)sin(\theta/2) + sin(3\theta/2)] \end{Bmatrix} \tag{2.26f}$$

$$u_z = -(\nu" z/E)(\sigma_{xx} + \sigma_{yy}) = -(\nu" z/E)(\sigma_{rr} + \sigma_{\theta\theta}) \tag{2.26g}$$

Mode II:

$$\begin{Bmatrix} \sigma_{xx} \\ \sigma_{yy} \\ \sigma_{xy} \end{Bmatrix} = \frac{K_{II}}{\sqrt{2\pi r}} \begin{Bmatrix} -sin(\theta/2)[2 + cos(\theta/2)cos(3\theta/2)] \\ sin(\theta/2)cos(\theta/2)cos(3\theta/2) \\ cos(\theta/2)[1 - sin(\theta/2)sin(3\theta/2)] \end{Bmatrix} \tag{2.26h}$$

$$\begin{Bmatrix} \sigma_{rr} \\ \sigma_{\theta\theta} \\ \sigma_{r\theta} \end{Bmatrix} = \frac{K_{II}}{\sqrt{2\pi r}} \begin{Bmatrix} sin(\theta/2)[1 - 3sin^2(\theta/2)] \\ -3sin(\theta/2)cos^2(\theta/2) \\ cos(\theta/2)[1 - 3sin^2(\theta/2)] \end{Bmatrix} \tag{2.26i}$$

$$\sigma_{zz} = \nu'(\sigma_{xx} + \sigma_{yy}) = \nu'(\sigma_{rr} + \sigma_{\theta\theta}) \tag{2.26j}$$

$$\sigma_{xz} = \sigma_{yz} = \sigma_{rz} = \sigma_{\theta z} = 0 \tag{2.26k}$$

$$\begin{Bmatrix} u_x \\ u_y \end{Bmatrix} = \frac{K_{II}}{2E}\sqrt{\frac{r}{2\pi}} \begin{Bmatrix} (1+\nu)[(2\kappa + 3)sin(\theta/2) + sin(3\theta/2)] \\ -(1+\nu)[(2\kappa - 3)cos(\theta/2) + cos(3\theta/2)] \end{Bmatrix} \tag{2.26l}$$

$$\begin{Bmatrix} u_r \\ u_\theta \end{Bmatrix} = \frac{K_{II}}{2E}\sqrt{\frac{r}{2\pi}} \begin{Bmatrix} (1+\nu)[-(2\kappa-1)sin(\theta/2)+3sin(3\theta/2)] \\ (1+\nu)[-(2\kappa+1)cos(\theta/2)+3cos(3\theta/2)] \end{Bmatrix} \tag{2.26m}$$

$$u_z = -(\nu" z/E)(\sigma_{xx}+\sigma_{yy}) = -(\nu" z/E)(\sigma_{rr}+\sigma_{\theta\theta}) \tag{2.26n}$$

Mode III:

$$\sigma_{xx} = \sigma_{yy} = \sigma_{rr} = \sigma_{\theta\theta} = \sigma_{zz} = \sigma_{xy} = \sigma_{r\theta} = 0 \tag{2.26o}$$

$$\begin{Bmatrix} \sigma_{xz} \\ \sigma_{yz} \end{Bmatrix} = \frac{K_{III}}{\sqrt{2\pi r}} \begin{Bmatrix} -sin(\theta/2) \\ cos(\theta/2) \end{Bmatrix} \tag{2.26p}$$

$$\begin{Bmatrix} \sigma_{rz} \\ \sigma_{\theta z} \end{Bmatrix} = \frac{K_{III}}{\sqrt{2\pi r}} \begin{Bmatrix} sin(\theta/2) \\ cos(\theta/2) \end{Bmatrix} \tag{2.26q}$$

$$u_x = u_y = u_r = u_\theta = 0 \tag{2.26r}$$

$$u_z = (4K_{III}/E)\sqrt{r/2\pi}[(1+\nu)sin(\theta/2)] \tag{2.26s}$$

and

$$\kappa = \begin{cases} (3-\nu)/(1+\nu), \ \nu' = 0, \ \nu" = \nu, & \text{(plane stress)} \\ (3-4\nu), \ \nu' = \nu, \ \nu" = 0, & \text{(plane strain)} \end{cases} \tag{2.26t}$$

A fracture criterion for mode I cracks is now postulated as:

$$K_I \geq K_{Ic}. \tag{2.27}$$

K_{Ic} is a critical stress intensity factor and is a material's characteristic resistance to fracture. If the remote applied stress σ_A (as shown in Fig. 2.11) leads to a stress intensity K_I and if the fracture criterion in Eq. (2.27) is fulfilled, the crack can grow. It

can be shown that Eq. (2.27) is equivalent to Eq. (2.24). Similar fracture criterions can be determined for mode II and model III cracks too with $K_{II} \geq K_{IIc}$ and $K_{III} \geq K_{IIIc}$. It has been shown that the stress intensity factor K can also be related to the remote applied stress σ_A as [111]:

$$\sigma_A = \frac{K}{Y\sqrt{a\pi}} \tag{2.28}$$

where Y is a constant determined by the specimen's dimensions and geometry. Corresponding to this, the fracture criterion for mode I crack can also be written as

$$\sigma_A \geq \frac{K_{IC}}{Y\sqrt{a\pi}}. \tag{2.29}$$

Similar fracture criterions are also applicable to mode II and III cracks. For some materials, the fracture resistance (critical stress intensity factor) increases with crack extension. This gives rise to the characteristic resistance-curve behavior [8, 9].

2.3.2. Cohesive zone model

So far we have considered the fracture mechanics as linear elastic, with the assumption that the non-linear processes at the crack tip are confined within a very small dimension compared to the crack size. There is a need to better describe the separation process represented so far by the term fracture energy Γ. Besides, the infinite stress at the crack tip when r approach zero is unrealistic. This led to the development of the concept of a cohesive zone model that describes the non-linear separation process at the crack tip.

Barrenblatt modeled the separation process at the crack tip by considering two separating crack surfaces connected with an array of non linear springs [112] (Fig. 2.12). As the separation of the crack planes, u increases, the traction in the springs first

increases in a linear manner (following Hooke's law), then increase in a non-linear manner until it achieves a maximum traction σ_0. After that, the traction decreases to 0 at the separation of $u = \delta$, which marks the end of the cohesive zone. Beyond δ, the cohesive stress σ becomes negligible. The area under the traction-separation curve represents the work of separation and is equal to the fracture energy Γ,

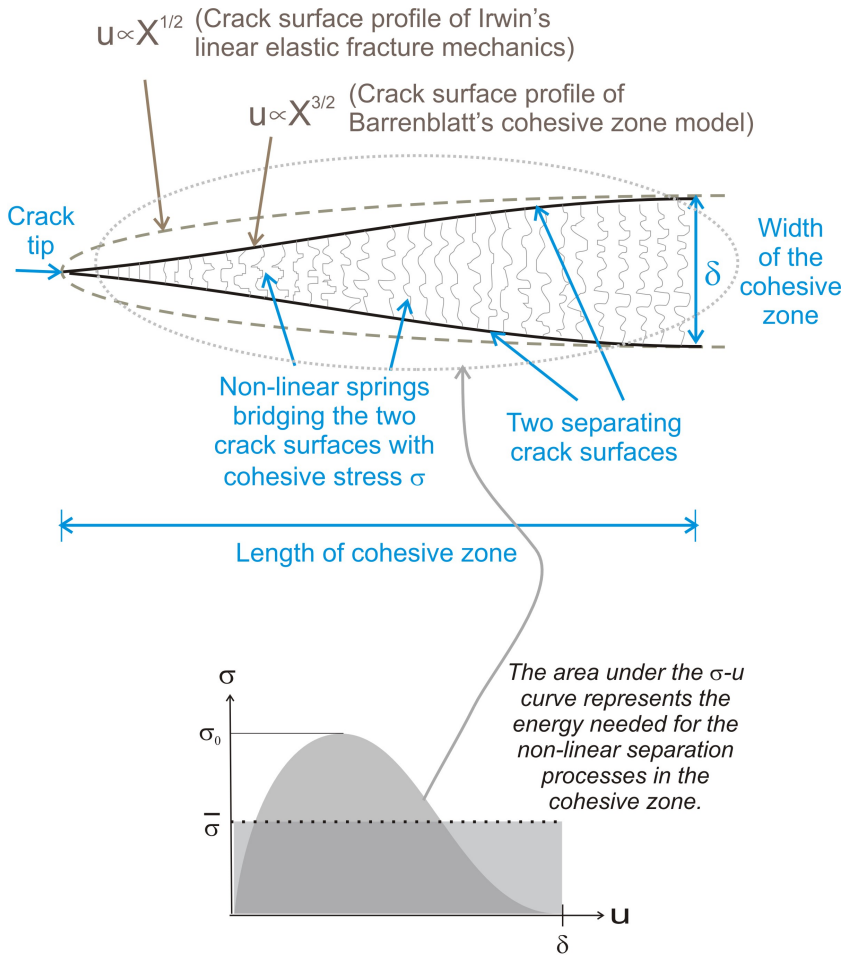

Figure 2.12.: Cohesive zone model, which describes the non-linear separation processes at the crack tip. Upper drawing: Crack profile of Barrenblatt's cohesive zone model (solid curve) relative to Irwin's linear elastic fracture mechanics (dashed curve). Barrenblatt [112] modeled the cracking process in a cohesive zone as an array of non-linear springs joining two crack surfaces. Lower drawing: The traction-separation curve when two crack planes separate. When the crack separation u becomes bigger than δ, the cohesive stress σ becomes negligible. The horizontal dotted line shows the average traction $\overline{\sigma}$ when the material is assumed as perfectly plastic.

$$\Gamma = \int_0^\infty \sigma(u)du \tag{2.30}$$

For simplicity, the traction-separation curve is often idealized as perfectly plastic where the traction has a constant value at $\overline{\sigma}$ and therefore $\Gamma = \overline{\sigma} \cdot \delta$. A load-displacement solution for a cohesive zone with a constant traction is described in more details in Chapter 5.2.2.

3. Size-dependent elastic/inelastic behavior over mm and nm length scales

Enamel's hierarchical structure has made the analysis of its mechanical behavior complex. A profound understanding of the structure-behavior relationships necessitates its mechanical characterization at all hierarchical levels. Characterization at the nanoscale helps to probe local origins of macroscale responses. Characterization at all length scales may provide guidance as to how enamel translates the strengths derived from nanostructures and hierarchical structures to macroscale robustness. However, current research on enamel lacks a comprehensive assessment of the mechanical properties on most important hierarchical length scales which are namely: 'bulk enamel' (0.5-2 mm), 'multiple rods' (≈50 μm), 'multiple crystallite fibers' within one rod (≈5 μm) and 'single crystallite fiber' (≈50 nm). Indentation with spherical tipped indenters enables determination of properties at these various length scales because of the geometrical self similarity and the ability to select indenters with varying radii.

In this study, human and bovine enamel's stress-strain behavior with uni-axial compression at millimeter length scale and spherical indentation with indenter radii of

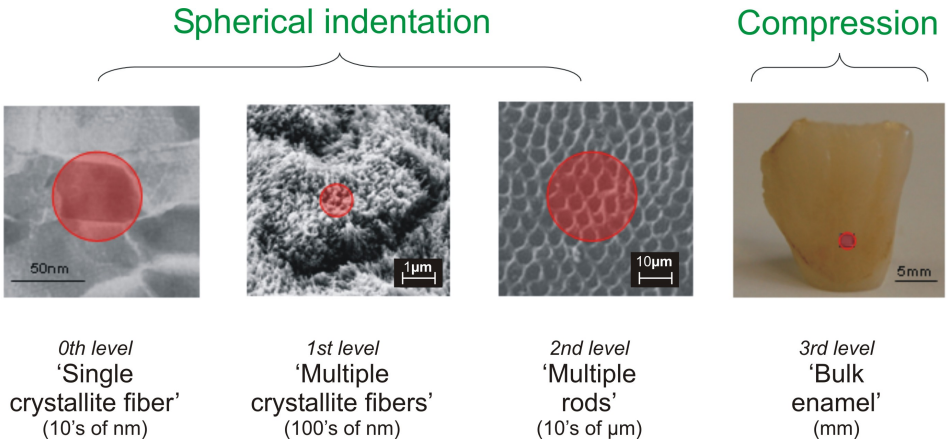

Figure 3.1.: Spherical indentation tests and uni-axial compression are used to probe the elastic/inelastic transition of enamel from 0^{th} to 3^{rd} level of its hierarchical structures, corresponding to contact areas of 'single crystallite fiber' [18], 'multiple crystallite fibers' within one enamel rod, 'multiple rods' [113] and 'bulk enamel'.

3mm, 8.3 μm, 63 nm are quantified. The corresponding contact areas are bulk enamel, several rods, multiple apatite crystallites and finally approximately one apatite crystallite (Fig. 3.1). Besides the elastic response we are interested in the limit of elastic deformation which corresponds to an elastic/inelastic transition.

This chapter is based on the following published articles:

- Ang, S. F.; Bortel, E. L.; Swain, M. V.; Klocke, A.; Schneider, G. A. **Size-dependent elastic/inelastic behavior of enamel over millimeter and nanometer length scales.** *Biomaterials*, 31(7), 1955-1963 (2010).
- Ang, S. F.; Scholz, T.; Klocke, A.; Schneider, G. A. **Determination of the elastic/plastic transition of human enamel by nanoindentation.** *Dental Materials*, 25(11), 1403-1410 (2009).

3.1. Materials and methods

3.1.1. Materials

For uni-axial compression tests, permanent bovine mandibular incisors were used due to their larger size and amount of enamel compared to human teeth. Bovine enamel also shows very similar microstructure with human enamel in terms of rod size and shape [88, 114]. Rectangular prisms were first cut from the labial side of bovine incisors, as shown in the upper inset in Fig. 3.2. With the upper surface bonded by double-sided tape on a holder, the lower surface was first polished with an abrasive paper of grit 4000, followed by diamond suspensions of down to 1 μm. The polishing steps were then repeated for the upper surface.

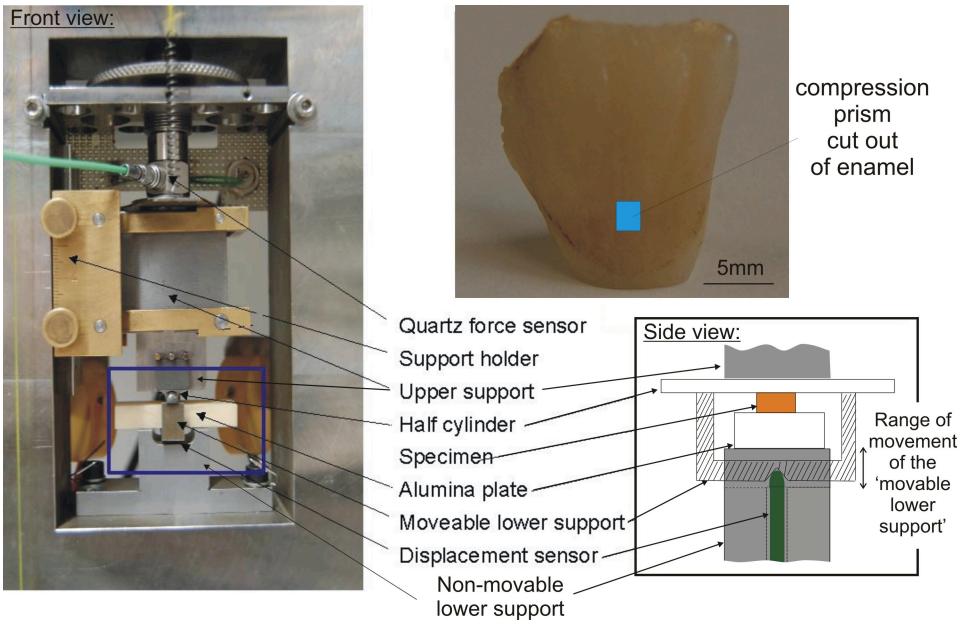

Figure 3.2.: Uni-axial compression device. Upper inset shows the portion of labial bovine enamel cut out for sample preparation. Lower inset shows the side view of the equipment parts for compression tests.

Human third molar teeth were utilized for the nanoindentation. After disinfection in 0.1 wt% thymol, the teeth were stored in Hank's Balanced Salt Solution (HBSS,

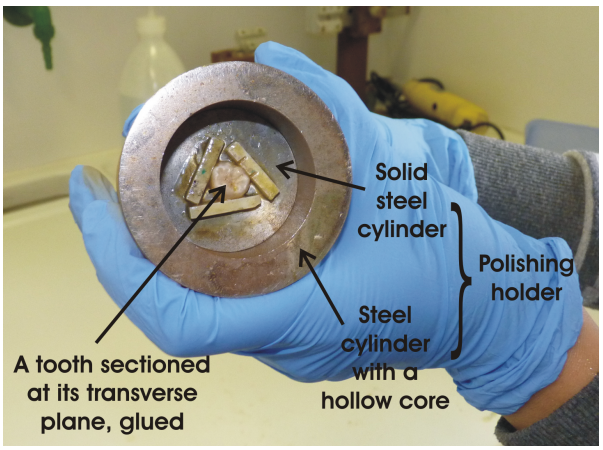

Figure 3.3.: A tooth sectioned at its transverse plane was glued on a polishing holder, which consists of a solid steel cylinder core and a hollow cylinder.

Invitrogen, USA) before sample preparation in order to minimize near surface demineralization and, subsequently, a change in mechanical properties [115]. The teeth were cut at the junction between crown and root and the root was discarded. The tooth surface facing the root was then glued onto a solid steel cylinder which was to be attached inside a steel cylinder with a hollow core (Fig. 3.3). The steel cylinder with a hollow core acted as the polishing holder and also maintained the plane parallelism of the polished surface. The cuspal region of the tooth was first polished with an abrasive paper of grit 4000. It was further polished with diamond suspensions to 0.25 μm. The final polishing step was performed with silica suspension of 0.06 μm (Mastermet 2, Bühler, Germany). The polished tooth was then glued face-up on a magnetic plate with wax for subsequent investigation with AFM and nanoindentation. The polished tooth surface was investigated in regions where enamel rods were oriented parallel to the nanoindentation direction.

Synthetic polycrystalline hydroxyapatite was used for comparison purposes in nanoindentation tests. The materials were provided from the Department of Materials Science and Engineering, University of Illinois at Urbana-Champaign with purity of >99.9 % and grain size of around 1 μm. The polishing steps were the same as those for the human third molar teeth.

3.1.2. Methods

Two methods are used in this study: uni-axial compression tests and nanoindentation.

3.1.2.1. Uni-axial compression

The principal experimental setup for the uni-axial compression is shown in Fig. 3.2, modified from a previous experimental setup by Jelitto et al. [116]. The equipment parts for uni-axial compression are mounted in a very rigid metal frame. The force exerted on the sample is controlled manually. A quartz force sensor (quartz dynamic load cell 9212, Kistler Instrumente GmbH, Germany) of high sensitivity (-11.3 pC/N) and minimal drift is used to measure the exerted force. The sample is loaded to a maximum force of 3 kN. A half cylinder, held to the upper support by magnets, is placed in between the upper support and the sample to rectify possible lack of plane parallelism of compressed sample surfaces. The displacement of the upper support is transferred via a movable lower support to an inductive position encoder (1-Weta1/2 mm, HBM, Germany) with linearity error of $<\pm 0.3$ %, which is programmed to measure over a distance of ± 100 µm.

An alumina sample of approximately 4-5 mm^2 in area and 1.5 mm in thickness is used to calibrate the effect of equipment deformation under compression. It is assumed that the compressibility of alumina is negligible up to 3 kN with a pressure of 150 MPa, and the generated force-displacement response represents the equipment deformation under loading. (For the calibration curve please refer to Appendix A.1. The calibration has an uncertainty of <2 µm.) All force-displacement curves with specimens had this equipment deformation subtracted before the stress-strain curves were computed. Compression of $2\times2\times2$ mm^3 aluminum cubes ($AlMgSi_{0.5}$) showed reproducible (0.2 %)

yield stress and displayed similar values shown in the material data sheet (≈160 MPa). The uncertainty of displacement of ±2 μm is ±10 % of 20 μm displacement used in the calculation of elastic modulus, and ±2 % of the 100 μm total displacement shown in Fig. 3.5(a).

3.1.2.2. Nanoindentation

The nanoindentation experiments were performed using a Triboscope indenter system (Hysitron, USA) mounted with a diamond spheroconical indenter tip (Hysitron, USA). 3 indenters were used in this study: R=8.3 μm, R=0.86 μm and R=63 nm. The R=63 nm indenter is a cube corner indenter for which the tip is assumed to be reasonably spherical at very low penetration depth (h_t<10 nm). The indenter radii calibration is explained in Appendix A.2.

All indentation tests on human enamel were done at ambient conditions. Each series of indentations was finished within 8 hours. Using the 8.3 μm indenter, one human third molar was studied with indentation loads of 5 mN and 11 mN. The indentations were placed in the middle of the enamel rods. With the 0.86 μm indenter, the synthetic HAP was studied with indentation loads to 2 mN. Using the R=63 nm indenter, three human third molars and the HAP sample were studied with indentation loads to 0.4 mN. The indentations on enamel using the R=63 nm indenter were placed at four specific micro structural locations, namely: 'head', 'center', 'neck' and 'tail' of the rods (Fig. 3.4). All indentation tests consisted of one loading and unloading cycle in 20 s. All resultant curves consisted of 8000 data points. The load-displacement data were used to derive the indentation stress-strain curves. The reduced elastic moduli were calculated using Eq. (2.2) (and, as explained in Chapter 2.2.2, when $h_t \ll R$, Eq. (2.11) is equivalent to Eq. (2.2)). The indentation hardness, H, a measure of the material's

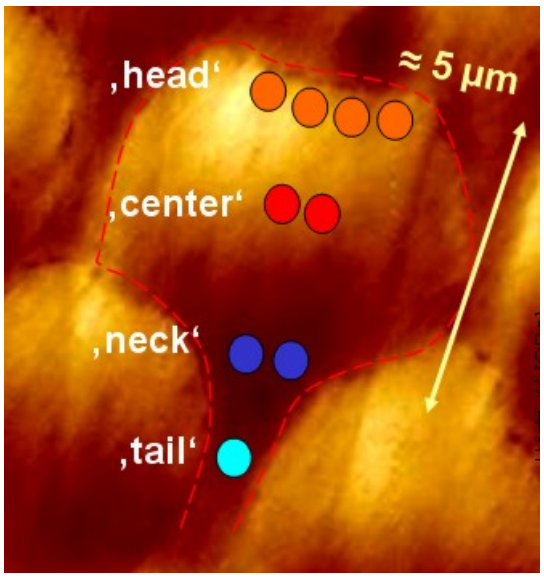

Figure 3.4.: The R=63 nm indenter was used to make indents on 4 regions inside enamel rods: ‘head’, ‘center’, ‘neck’ and ‘tail’.

resistance against permanent deformation is computed from Eq. (2.8) according to the experimental protocol described by Oliver and Pharr [92].

To observe any potential cracking in the enamel from nanoindentation tests, indentations using the R=63 nm indenter with 1 mN load were made. AFM with a high resolution tip (nominal tip radius<10 nm) was used to investigate the topography of the indented enamel surface [117].

3.2. Results

The equipment deformation effect of the compression equipment is calibrated and is outlined in Appendix A.1. The radii of the 3 indenters used in this study were calibrated as 8.3±0.9 µm, 0.86±0.03 µm and 63±11 nm respectively and is explained in Appendix A.2. For simplification, these indenters are called R=8.3 µm indenter, R=0.86 µm indenter and R=63 nm indenter.

After the final polishing steps, the achieved 'surface roughness' for the bovine enamel rectangular prisms for compression test is <5 μm. The 'surface roughness' here refers to the distance of the highest peak and the lowest valley of the contacted surface during tests. Due to the difficulties involved in specimen preparation, only stress-strain curves of one satisfactory sample with a dimension of ≈2×2 mm^2 in area and ≈1 mm in thickness is presented in this article. Many samples had pre-existing cracks (observed under a light microscope) or were too thin after appropriate roughness was achieved. After polishing for nanoindentation samples (both human enamel and synthetic HAP), the achieved surface roughness, RMS (calculated by the equipment software) is <1 nm over an area of >1×1 μm^2. RMS is calculated based on the equation $RMS = \sqrt{(\sum(Z_i)^2)/N}$ where Z_i are the measured heights of every pixel and N is the total number of measured heights (pixels).

The stress-strain curves from two uni-axial compression loadings, together with indentation stress-strain curves of enamel are plotted in Fig. 3.5 (a), (c) and (d). (The corresponding $P - h_t$ curves are shown in Appendix B.1.) The data from spherical indentation tests on enamel by Staines et al. [118] using R=3.125 mm indenter were extracted and re-plotted as P_{m} versus a/R in Fig. 3.5 (b). The limit of elastic range is approximated when the curve deviates from linearity.

For macroscopic compression of bovine 'bulk enamel', the stress-strain curve of the first loading indicates a limit of elastic range at around ≈400 MPa. The initial stress-strain curve firstly exhibits a linear elastic response with a compression modulus of ≈30 GPa, then deformed inelastically with decreased stiffness (Fig. 3.5 (a)). It reached the maximum stress of around ≈680 MPa without ultimate catastrophic fracture. Instead, it exhibited progressive damage with a jagged curve behavior at nearly constant stress at ≈680 MPa. This is followed by another jagged curve at a lower stress level at ≈580 MPa. Upon unloading followed by immediate reloading, the specimen first deformed

elastically at a decreased elastic modulus of ≈14 GPa, reached a similar limit of elastic range as in the first loading, and was able to attain similar ultimate strength achieved in the first loading.

For indentation tests on enamel, the limits of elastic range were observed as ≈0.9 GPa for 'multiple-rod'(a≈90 μm with the R=3 mm indenter, h_t≈3 μm) [118], 1.6 GPa for 'multiple-crystallite-fiber' (a≈250 nm with the R=8.3 μm indenter, h_t≈7 nm), 6-17

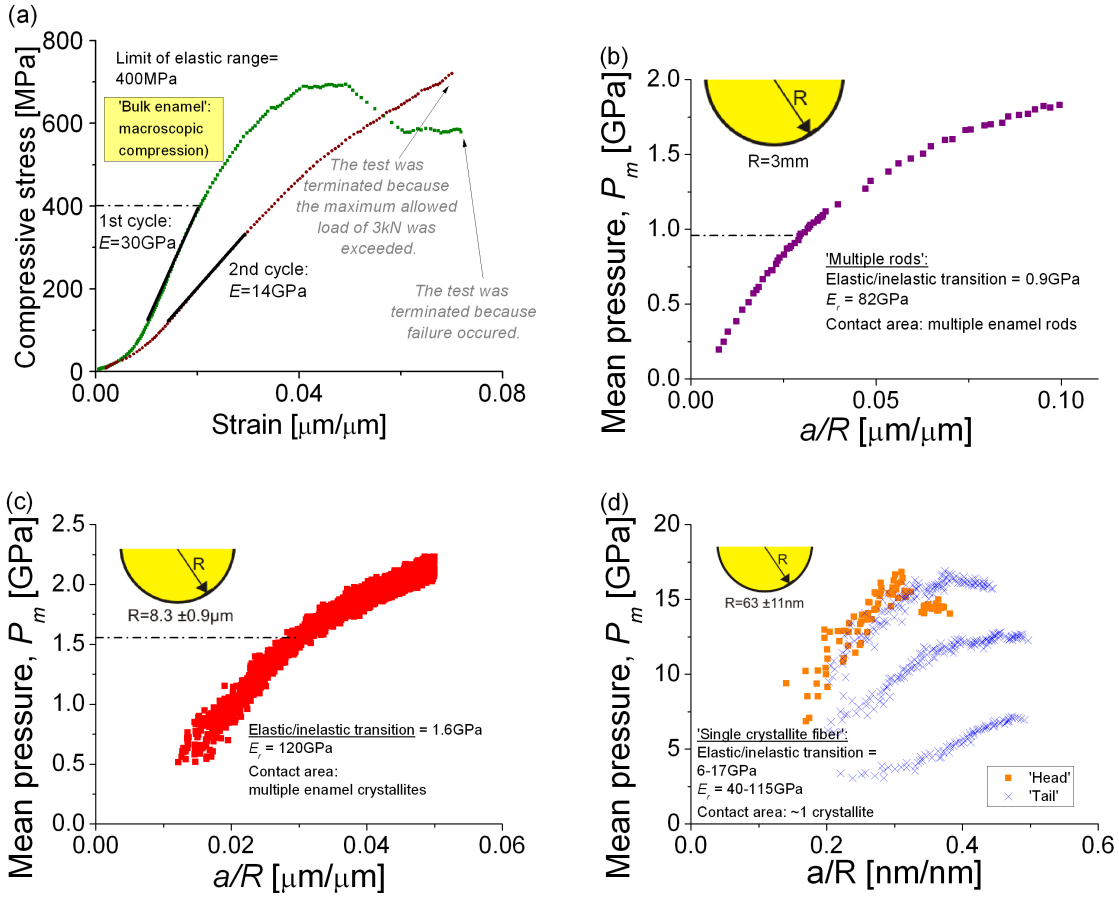

Figure 3.5.: Enamel's stress-strain curves. (a) Uni-axial compressive stress-strain curves for bovine enamel. Indentation stress-strain curves of human enamel with (b) R=3 mm indenter [118] (c) R=8.3 μm indenter and (d) R=63 nm indenter. Depending on the contact areas, these length scales corresponds to (a) 'bulk enamel' (b) 'multiple rods' [118], (c) 'multiple crystallite fibers' and (d) 'single crystallite fiber'. The curves in Fig. (c) and (d) do not start from zero because data of h_t<1 nm are associated with noise and are discarded.

GPa for 'single-crystallite' with a contact area of approximately one crystallite fiber (a=20 nm with the R=63 nm indenter, h_t≈3-10 nm) (Fig. 3.5 (b)-(d)). The calculated reduced elastic moduli are E_r=82 GPa (R=3 mm indenter), E_r=120 GPa (R=8.3 μm indenter) and E_r=76±18 GPa (R=63 nm indenter). Fig. 3.5 (c) is a collective response from all indentations with the R=8.3 μm indenter. Due to the large number of indentation curves with the R=63 nm indenter at all 4 regions inside enamel rods, only some of these indentation stress-strain curves were plotted in Fig. 3.5 (d) to illustrate overall behaviors. The indentation stress-strain curves in Fig. 3.5 (b)-(d) first deformed elastically, and then appeared to soften.

Under the R=63 nm indenter, the collective mean values and the standard deviations of reduced elastic moduli, indentation hardness and the elastic/inelastic transition of enamel of all regions are 76±18 GPa, 5.7±0.3 GPa and 12±3 GPa.

The synthetic HAP specimen show mean values of E_r=120±6 GPa, H=10±1 GPa and an elastic/inelastic transition=11±2 GPa with the R=0.86 μm indenter. For

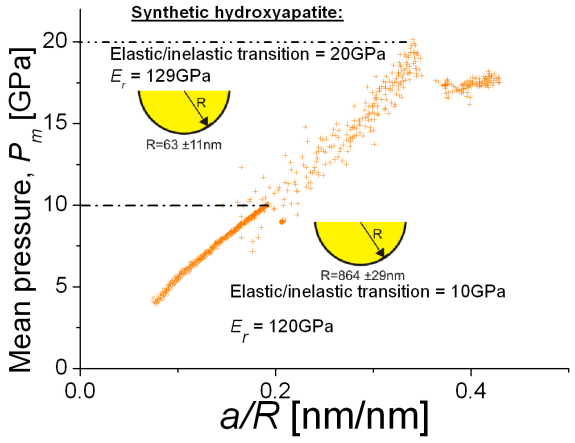

Figure 3.6.: Indentation stress-strain curves of synthetic HAP with R=0.86 μm indenter and R=63 nm indenter. (The extensive curves beyond the elastic/inelastic transition were not shown here because they no longer fulfill the assumed elastic behavior and are unrealistic to be used to calculate P_m versus a/R using Eq. (2.11).)

nanoindentation with the R=63 nm indenter, the synthetic HAP specimen show mean values of E_r=129±13 GPa, H=10±1 GPa and a elastic/inelastic transition=20±2 GPa. Examples of the indentation stress-strain curves are shown in Fig. 3.6. (The corresponding $P - h_t$ curves are shown in Appendix B.2.) With the same R=63 nm indenter the E_r and the elastic/inelastic transition of the synthetic HAP are about 40% higher than the average values of enamel.

3.3. Discussion

To illustrate the size-dependence of the elastic/inelastic transition, it is plotted versus the contact radius for both enamel and synthetic HAP in Fig. 3.7. The elastic/inelastic transition of HAP (≈7 GPa), probed by using R=10 µm indenter by He and Swain [119] is also included in the figure. With the reported reduced elastic modulus of HAP of 130 GPa, the elastic/inelastic transition of ≈7GPa and R=10 µm introduced into Eq. (2.11), the contact radius is calculated as ≈1270 nm. The elastic/inelastic transitions of enamel are always smaller than of synthetic HAP for contact radii up to 1000 nm. With increasing length scale, the elastic/inelastic transition of both materials decrease. Such behavior in synthetic HAP is attributed to an indentation size effect based on geometrically necessary dislocations [120, 121]. The underlying reason of such behavior in enamel is more complex due to its heterogeneous and hierarchical structure.

For the smallest contact radii of ≈20 nm, the length scale of 'single crystallite fiber', the enamel data scatter strongly, but the highest elastic/inelastic transition is close to the value of the nearly pure HAP (Fig. 3.7). It can be concluded therefore that in some of these measurements in enamel the indenter measures the mechanical response of a single apatite crystallite. In addition it can be concluded that even at these very

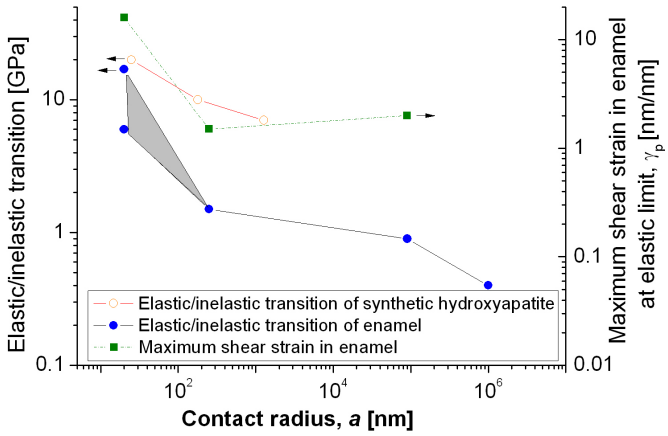

Figure 3.7.: Decreasing limit of elastic/inelastic transitions of enamel and synthetic HAP with increasing length scales. (The scattering of enamel's elastic/inelastic transitions at the contact radii of ≈20 nm shows that even at these very small length scales, the response may not always only include apatite crystallites within the enamel.) The right hand side Y-axis is the maximum shear strain in enamel at the elastic limit calculated according to Eq. (3.2).

small contact radii, the response may not always only include apatite crystallites within the enamel.

The lower elastic/inelastic transition values, down to approximately 6 GPa for contact radii of 20 nm, is likely to be related to the organic material separating the apatite crystallites, and will be discussed in more detail later. The next measured length scale 'multiple crystallite fibers' corresponds to contact radii of ≈250 nm which means that the mechanical probing involves multiple crystallite fibers and is within one rod. The corresponding elastic/inelastic transition of 1.6 GPa shows only limited scatter of ±0.1 GPa. Hence, enamel appears to be very homogeneous at this length scale. The next length scale 'multiple rods' corresponds to a contact radius of ≈90 µm which means that the mechanical probing averages over multiple rods. The corresponding elastic/inelastic transition is only 0.9 GPa, which is again small, but still double the value of the compression test. Therefore it is very obvious that every hierarchical structure of enamel has a different mechanical response. Possible non-linear mechanisms of inelastic

deformation are extension and breakage of protein layers, interfacial slippage, viscoelastic effects, all of which may lead to rotations of the apatite crystallites or cracks in them. These will be considered later based on the experimental findings.

Fig. 3.8 shows a plot of the elastic/inelastic transition versus reduced elastic modulus measured for the length scale of 'single crystallite fiber' (R=63 nm indenter) for all four specified regions ('head', 'center', 'neck', 'tail') inside the enamel rod structure. It is obvious that the elastic/inelastic transitions even within the same region in the rod scatter considerably. This is not caused by measurement errors because measurements with the same indenter on synthetic HAP showed a maximum of 10% standard deviations from the mean values. On the other hand an approximately linear relationship is observed between the elastic limit values and the reduced Young's modulus. Because all measurements were performed within rod units, changes of the apatite crystallite orientation or compositional changes might result in these strong variations. While variations of Young's modulus of synthetic HAP between 127 and 162 GPa have been shown [122], they do not explain the very low E_r values measured. In addition, large E_r variations were measured at the same locations inside the rods, with similar apatite crystallite orientations observed [14, 21]. Therefore, it is most probable that compositional changes or the volume fraction of mineral/protein are the source of the observed variations. Applying the equation from Ji and Gao [11], the measured modulus, E, can be related to the volume fractions of minerals, V_{m}.

$$V_m = \frac{-\left(4E_mE - G_p\rho^2E\right) + \sqrt{\left(4E_mE - G_p\rho^2E\right)^2 + 16G_p\rho^2E_m^2E}}{2G_p\rho^2E_m} \tag{3.1}$$

with E_{m} the elastic modulus of the minerals, G_{p} the shear modulus of protein and ρ the aspect ratio of the crystallites. Since $E \approx E_r$ as explained in Section 2.2.1, we used E=40-115 GPa (Fig. 3.8), G_{p}=0.1 GPa [123], ρ=100 and E_{m}=129 GPa (Fig. 3.6), and

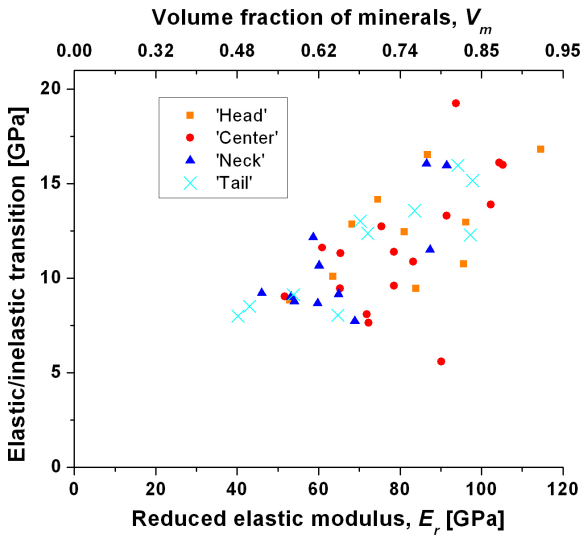

Figure 3.8.: Elastic/inelastic transition versus reduced elastic modulus, E_{r} (bottom x-axis) and V_{m} (top x-axis) for four regions inside enamel rods ('head', 'center', 'neck', 'tail') (R=63 nm). There is seemingly a linear correlation between both properties.

found that the involved V_{m} ranged from 0.48 to 0.93, as plotted in Fig. 3.8. When ρ=30 [124] is assumed, V_{m} is found to range from 0.79-0.98. Despite the influence of the assumed ρ on the calculated V_{m}, it is obvious that pronounced nanoscale heterogeneity in enamel prevails at lengths scales of 40 nm. Such nanoscale heterogeneity has been proposed as an effective energy dissipation strategy in bio-mineralized tissues [125].

Possible mechanisms for non-linear deformation in enamel

In this section, possible mechanisms for non-linear deformation in enamel which are non-linear extension of protein layers, viscoelasticity and cracking are discussed.

Non-linear extension of protein layers

On the possible causes of the observed elastic/inelastic transition in enamel, non-linear extension of protein layers is hypothesized to occur before the others such as crystallite frictional sliding and cracking. The maximum shear strain in the protein

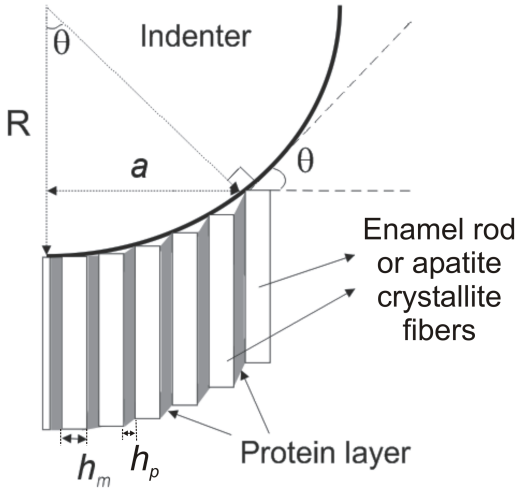

Figure 3.9.: Schematic illustration of enamel deformation induced by a spherical indenter. It is assumed that the deformation is completely due to the shear deformation of the protein layer.

layer, γ_{p} can be calculated using a model [126, 127] (Fig. 3.9):

$$\gamma_p = \frac{(h_m + h_p)\, tan\theta}{h_p} \tag{3.2}$$

with the maximum shear strain γ_{p} in the protein layer, h_{m} and h_{p} the thickness of the enamel rod or crystallite and protein layer depending on the length scales investigated, θ the contact angle between the indenter and the surface (Fig. 3.10). Since $\tan\theta = a/R$,

$$\gamma_p = \frac{(h_m + h_p)}{h_p} \frac{a}{R} \tag{3.3}$$

Using the above model for multiple enamel rods of h_{m}=5 µm and a protein layer in between them of h_{p}=70 nm the corresponding γ_{p} is calculated as ≈2 for the elastic limit with the 3 mm radius indenter [118]. For indentation involving multiple enamel crystallites within one enamel rod, h_{m}=50 nm is the thickness of one crystallite and h_{p}=1 nm is the thickness of the protein layer. The corresponding γ_{p} at the elastic

limit for R=8.3 μm indenter and R=63 nm indenter are calculated as ≈1.5 and ≈16 respectively. These values are plotted as the second Y-axis in Fig. 3.7. In order to estimate a reasonable elastic stretching limit for proteins in enamel tropocollagen is used as a reference. The strain limit of covalent bond stretching (after that molecular fracture occurs) in a single tropocollagen molecule is 0.5 [128]. This is consistent with macroscopic tensile stress-strain measurements on protein tissues such as horn (mainly keratin), tendon and ligament (mainly collagen), where the tensile strain limit is usually 0.5 or less [5, 129, 130]. The above calculated values are much higher than this elastic limit of 0.5. As a consequence it is very probable that the outermost protein layer at the border of the contact especially near the sample surface already deforms non-linearly or even breaks before the elastic/inelastic transitions of enamel were detected by the indentation tests. Shear deformation of protein layers and seemingly breakage of some protein backbone between crystallites under indentation has been identified in a cross-sectional TEM view below a 500mN Berkovich indent in enamel [131].

Viscoelasticity

The influence of viscoelasticity is also considered. In the compression test, the decreased elastic modulus in the second loading is unlikely to be dominated by any viscoelastic effect. In a viscoelastic structure, the first loading would squeeze out the soft substance inside the channels between inorganic minerals, as illustrated in a previous study [132]. Before its recovery, a structure would show stiffer behavior upon second loading and not decreased elastic modulus, observed in Fig. 3.5 (a).

In a recent nanoindentation study by Guidoni et al. [133], the creep displacement of enamel shows a displacement rate of 0.33 nm/s under a constant load of 5 mN using a Berkovich indenter. Such a creep effect is expected to be less significant for the blunter 8.3 μm spherical, with which the limit of elastic range happens within the first second of

the present experiment. For the cube corner indenter, a creep response of 0.5 nm/s was recorded under a constant load of 5 mN on atmospherically dry enamel [133]. Even at such a high load (5 mN), the creep response accounted for only <20 % of the displacement involved in this study when the limit of elastic range is observed. Therefore, the effect of creep when the load is smaller than 25 μN (the load when the elastic/inelastic transition is observed in enamel with R=63 nm indenter) is expected to be insignificant.

Cracking

Detailed investigations of the enamel surface with high resolution AFM around 1 mN indentations by the R=63 nm indenter (a cube corner indenter) did not reveal any kind of surface cracking within the resolution of our system (not shown here). This is probably also true for the indentation by R=8.3 μm indenter which is blunter. The E_{r} by R=8.3μm indenter is high (E_r=120 GPa) and may also be an indication of the absence of cracking. For R=3 mm indenter, it is unclear whether the lower E_r (82 GPa) in comparison to the R=8.3 μm indenter and R=63 nm indenter is due to cracking or the presence of thicker protein sheath for shearing. Nevertheless, all the indentation stress-strain curves (length scale <200 μm) exhibited elastic/plastic behaviors. This may also be assisted by the constraint provided by the surrounding elastic material around the indentation contact area. In contrast, the stress-strain curve on a macroscopic scale (length scale>1 mm) showed elastic/micro-crack induced damage behavior, which is most probably due to the cracking in enamel. Based on our findings, it appears that when a small volume is involved, plastic deformation is the major form of deformation when enamel exceeds the limit of elastic range. Whereas when a big volume is involved, micro-crack induced damage happens beyond the elastic limit.

A map of elastic/inelastic regions for enamel is proposed in Fig. 3.10. After a certain length scale, for example at a contact radius of 1 mm, when the stress increases,

the elastic region is followed directly by micro-crack induced damage. At the smaller studied length scale, when stress increases, the elastic region of enamel is followed by the plastic region, which might be caused by frictional sliding between crystallites, protein detachment from crystallites or deformation inside apatite crystallites, since the proteins are not able to carry the load. If very high stress happened at these small length scales, micro-crack induced damage will ensue. The boundary between the plastic and the micro-crack induced damage regions for length scales of <100 μm are estimated based on the experimental data of synthetic hydroxyapatite as the following. The data of the first 'pop-in' phenomena (increased displacement under constant load) of synthetic hydroxyapatite were extracted by doing nanoindentation with R=63 nm indenter and R=0.86 μm (Fig. 3.6), and with R=10 μm [119]. It has been experimentally observed that the first 'pop-in' of brittle materials are associated with initiation of dislocations [117, 134]. In another study, it has been reported that the first'pop-in' appeared to occur when a median crack is nucleated [135]. The subsequent 'pop-ins' of synthetic hydroxyapatite, when happened, followed closely after the first pop-ins and might be caused by crack initiation [117]. So, these values are deemed reasonable to approximate as enaml's plastic to micro-crack induced damage behavior of enamel and is plotted in Fig. 3.10. Nevertheless, the real transition of enamel's plastic deformation to micro-crack induced damage might be lower due to imperfection in biological apatite.

The behavior of enamel even at macroscopic scale showed desirable characteristics for a load-bearing structure. As shown in Fig. 3.5 (a), the bovine enamel rectangular prism is deformed in a progressive damage manner, which was also observed earlier in the compressive stress-strain curves of bone [136]. The load-bearing capability was observed to remain even beyond the ultimate strength, indicating the inherent crack damage tolerance of the structure instead of failing catastrophically. The stress-strain response associated with the second loading shows a decreased elastic modulus, which

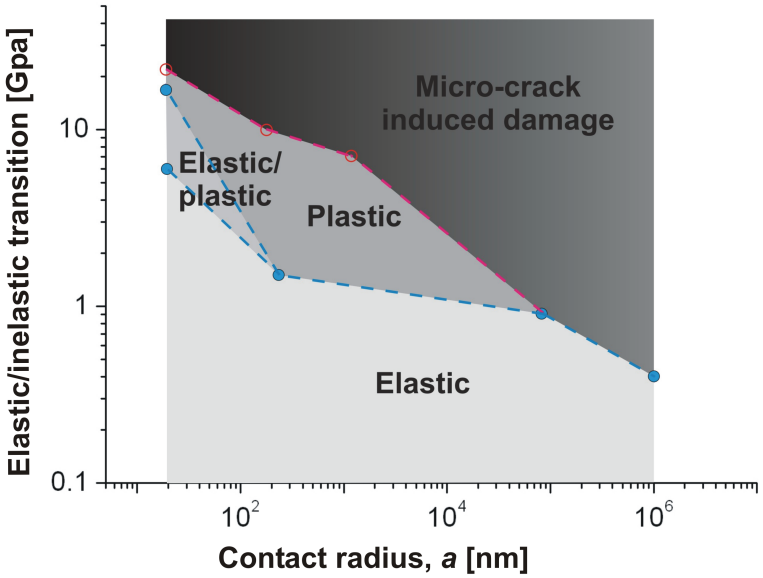

Figure 3.10.: A map of regions of the most probable deformation behaviors of enamel: elastic, plastic or micro-crack induced damage behavior. At the smallest investigated length scale, plastic behavior ensued after elastic deformation. However, for the biggest investigated length scale, micro-crack induced damage occurs beyond the elastic limit. (The boundary of plastic to micro-crack induced damage transition is estimated from the 'pop-in' phenomena of synthetic hydroxyapatite (explained in the text.)

could be attributed to substantial microcrack damage resulting from the first loading.

3.4. Conclusions

A comprehensive assessment of the elastic/inelastic behaviors in enamel for the different lengths scales is presented (Fig. 3.10). At the smallest length scale, plastic deformation occurs beyond the elastic/inelastic transition, and is unlikely to be caused by proteins alone. At the biggest length scale, micro-crack induced damage ensued after the elastic/inelastic transition was reached. The elastic/inelastic transition of enamel is 0.4-17 GPa from millimeter to nanometer length scales. These length scales encompass

essential hierarchical levels of enamel which are 'bulk enamel' (a≈1 mm), 'multiple rods' (a≈90 μm), 'multiple crystallite fibers' (a≈250 nm) and 'single crystallite fiber' (a≈20 nm). The macroscopic compression test results show that enamel is capable to deform in a progressive damage (saw tooth) manner in the inelastic region and also retain its load bearing capability beyond the ultimate strength. The contact loading at the 40 nm length scale revealed local heterogeneity.

4. Comparison of Mechanical Behavior of Enamel Rod and Interrod Regions

Dental enamel is able to maintain its structural integrity under mechanical loading conditions in the oral environment. It is often said that proteins and peptides contribute to the toughness of bio-mineralized materials (dentin, bone, enamel, nacre) through their extensive non-linear deformation. Indeed, energy loss occurs when a protein or peptide is stretched even at very small strains [137]. The interrod regions of enamel are relatively protein-rich compared to the enamel rod region and are therefore expected to exhibit hysteresis, higher inelastic energy dissipation, greater displacement under constant load (creep), lower viscosity and a higher relaxation time for stress relaxation. Previous studies comparing the enamel rod and the interrod regions showed that the elastic modulus and hardness in the enamel rod region are higher than in the interrod regions [138, 139]. The differences observed by Habelitz et al. may be a result of different crystallite orientations in the two regions [138]. In comparison, Ge et al. observed 50% higher elastic modulus and hardness in the enamel rod compared to the interrod region [139]. To date no emphasis was placed on the time-dependent property comparisons of these two regions, which may be attributed primarily to proteins but not the minerals

present.

This study aims to probe the mechanical property differences of enamel rod and interrod regions in enamel, with a focus on the contribution of organics. We used spherical indentation with ≈1 μm radius tip to perform nanoindentation on enamel in a liquid environment. Single loading-unloading curve tests were used to calculate the elastic modulus, hardness and energy dissipation for the enamel rod and interrod regions. In addition, in creep tests at constant load, energy dissipation, the viscosity and stress relaxation behaviors for both regions were determined.

This chapter is based on the following published manuscripts:

- Ang, S. F.; Saadatmand, M.; Swain, M. V.; Klocke, A.; Schneider, G. A. **Comparison of mechanical behaviors of enamel rod and interrod regions in enamel.** *Journal of Materials Research*, 27(2), 448-456 (2012).

4.1. Materials and methods

4.1.1. Materials

Human third molar teeth were utilized for the nanoindentation. After extraction, the teeth were disinfected in 0.1 wt% thymol before storing in Hank's Balanced Salt Solution (HBSS, Invitrogen, USA). The teeth were cut and polished as described in Section 3.1.1 except that the final step of polishing is now with the diamond suspensions of 0.05 μm diamond suspensions (Buehler, Germany). The polished tooth was then glued face-up on a steel plate with wax for subsequent investigation with nanoindentation. The polished tooth surface was investigated in regions where enamel rods were oriented parallel to the nanoindentation direction.

4.1.2. Methods

The nanoindentation experiments were performed using a Triboscope indenter system (Hysitron, USA) mounted on an AFM Dimension controlled by Nanoscope VI (Veeco, Santa Barbara, CA). The sphero-conical indenter (Hysitron, USA) has a long shaft (suitable to perform nanoindentation in liquid) and has a diamond tip of ≈1 μm radius. The indenter tip radii calibration procedure is explained in the Appendix A.2.

All indentation tests on human enamel were done in distilled water. Each series of indentation tests were completed within 12 hours. Distilled water was chosen over HBSS as the liquid medium because salt layer would otherwise be built on the sample surface (observed with AFM scanning). Habelitz et al. investigated the effect of storing dental enamel in de-ionized water for one day - the measured reduced elastic modulus and hardness seem to be lower after storage but still lies within the error range of the measurements on a fresh sample [115]. Therefore, the use of distilled water in the current experiment within 12 hours is not expected to cause significant change of mechanical properties.

One tooth was used for each indentation loading profile in Fig. 4.1 (a) and (b). For each loading profile, 5 indentations were done each for the enamel rod and for the interrod regions on the teeth. The interrod region could be recognized by the <3 nm depressions due to polishing effect. The loading profiles are:

The load-unload profile (Fig. 4.1 (a)): (i) P=0 μN to P=500 μN in 10 s (ii) P=500 μN to P=0 μN in 10 s.

The load-hold-unload profile (Fig. 4.1 (b)): (i) P=0 μN to P=5 μN in 10 s (ii) Holding at P=5 μN for 60 s (iii) P=5 μN to P=500 μ N in 10 s (iv) P=500 μN for 180 s (v) P=500 μN to P=0 μN in 10 s.

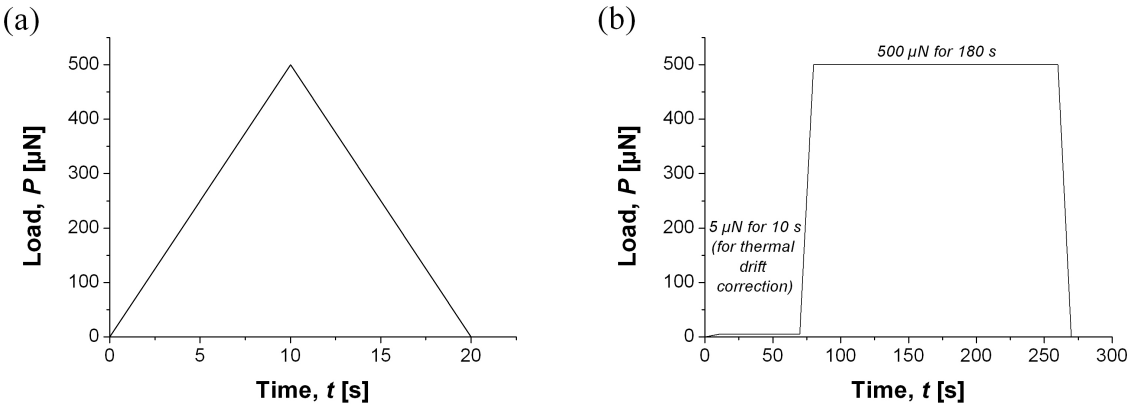

Figure 4.1.: The load-time curves (a) of the load-unload and (b) the load-hold-unload loading profiles.

The resultant curves from both loading profiles consist of 8000 data points. The load-hold-unload profile involves a holding period of 180 s, and therefore, step (ii) (holding at P=5 μN for 60 s) is necessary for the manual thermal drift correction. It is assumed that holding at such a low load at step (ii) does not cause increasing depth and the change in depth over time in this period is due to thermal drift. The thermal drift (nm/s) is calculated and is assumed to be linear. These drifts were then subtracted from step (iii), (iv) and (v) above to remove the thermal drift contribution during this dwell period. This methodology to remove thermal drift contribution has proven to be robust by applying the same loading function and the subsequent correction on sapphire. The 'creep' of sapphire surface after this correction methodology is <2 nm . Since sapphire should not exhibit creep under this loading profile and in room temperature, this <2 nm displacement represents the displacement uncertainty of the correction.

The analyses of the mechanical properties was carried out as described in Section 2.2. The reduced elastic modulus, $E_{r,loading}$ is calculated based on Eq. (2.2). $E_{r,unloading}$ is calculated based on Eq. (2.6) where the unloading curve is fitted as elastic unloading from a spherical impression, described in Section 2.2.1. The hardness H is calculated from Eq. (2.8). The calculation of elastic energy recovery (U_E), inelastic energy dissi-

pation (U_{Inel}), inelasticity index are described in Section 2.2.3. The analysis regarding creep, creep compliances (C_0 and η) and stress relaxation are detailed in Section 2.2.4 - 2.2.6.

For statistical analysis, p-values are calculated to determine whether the differences of two regions are significant. For a significant level of 0.05, when the p-value$<$0.05, the mechanical properties of both regions are statistically significantly different.

4.2. Results

The indenter radii for the used long shaft indenter was calibrated to be R=889±19 nm (explained in Appendix A.2). The polished enamel samples have a surface roughness of $<$1 nm. The thermal drift for the step loading profile measurements was measured to be 0.4-0.8 nm/s.

For the load-unload measurements, the maximum penetration depth is h_t=26-30 nm and corresponds to a contact radius of a≈200 nm. For the load-hold-unload measurements, the maximum penetration depth is h_t=47-57 nm and corresponds to a contact radius of a≈250 nm. All load-penetration depth curves of the enamel rod and the interrod regions for both loading profiles are shown in Fig. 4.2 (a) and (b).

The mechanical properties probed at enamel rod and interrod regions by using the load-unload profile (Fig. 4.1 (a))and the calculated p-values are summarized in Table 4.1. The reduced elastic modulus $E_{r,loading}$ and $E_{r,unloading}$ of the enamel rod regions (86.3±5.9 GPa and 109.4±4.8 GPa) are significantly higher than those in the interrod region (78.2±3.9 GPa and 103.0±3.4 GPa). The hardness in both regions show statistically significant difference too (H_{rod}=5.2±0.4 whereas $H_{interrod}$=4.8±0.2). (Note: An overlapping of both standard deviations (STD) here might lead to an assumption that

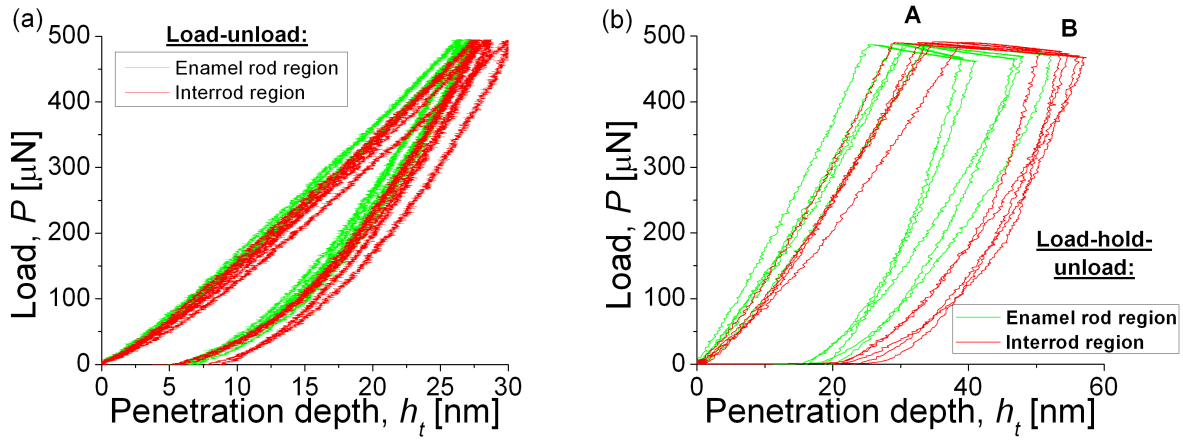

Figure 4.2.: (a) All load-penetration depth curves under (a) the load-unload profile (b) and the load-hold-unload profile. For each loading profile, the number of measurements in each region is 5. The 'A' and 'B' in (b) denote the beginning and the end of the holding period at P_{max}=500 μN.

both average values must be not statistically different. Usually, both average values show no statistically difference if their standard error bars (not STD) overlap. The standard error bars of both values could be calculated by using the formula SE=STD/$\sqrt{5}$ and gives 0.2 and 0.1 for both hardness respectively. Hence, the two error bars do not overlap and an statistical test has shown that the corresponding p-value is <0.05, thus being statistically significant different.) The elastic energy recovery of the enamel rod region ($U_{E,rod}$=3924±131×10^{-6} nJ) is statistically significantly lower than in the interrod region ($U_{E,interrod}$=4097±89×10^{-6} nJ). The inelastic energy dissipation and the inelasticity index of both regions do not show statistically significant differences. The inelasticity energy dissipation is 2408±150×10^{-6} nJ in enamel rod region and is 2567±345×10^{-6} nJ in interrod region. The inelasticity index of the enamel rod and interrod regions are 38±2 and 38±4 respectively.

The mechanical properties probed at enamel rod and interrod regions by using the load-hold-unload profile (Fig. 4.1 (b)) and the calculated p-values are summarized in Table 4.2. The inelastic energy dissipation in both regions show statistically significant

difference: the dissipation in the enamel rod region (9315±1500×10^{-6} nJ) is statistically significantly lower than in the interrod region (12656±1297×10^{-6} nJ). The values of the elastic energy recovery, the inelasticity index and the creep do not show statistically significant difference.

Table 4.1.: Mechanical properties probed from the load-unload profile (Fig. 4.1 (a)).

	$E_{r,loading}$ [GPa]	$E_{r,unloading}$ [GPa]	H [GPa]	U_E [×10^{-6} nJ]	U_{Inel} [×10^{-6} nJ]	*Inelasticity index* [%]
Rod (N=5)	86.3±5.9	109.4±4.8	5.2±0.4	3924±131	2408±150	38±2
Interrod (N=5)	78.2±3.9	103.0±3.4	4.8±0.2	4097±89	2567±345	38±4
p-value	0.033	0.039	0.046	0.040	0.369	0.839

Table 4.2.: Mechanical properties probed from the load-hold-unload profile (Fig. 4.1 (b)).

	U_E [×10^{-6} nJ]	U_{Inel} [×10^{-6} nJ]	*Inelasticity index* [%]	Creep [nm]
Rod (N=5)	4766±1076	9315±1500	66±5	16±3
Interrod (N=5)	5194±850	12656±1297	71±5	21±5
p-value	0.504	0.005	0.172	0.111

	$\mathbf{1}/C_\mathbf{0}$ [GPa]	η [× 10^{12} Pa · s]	P_{m0} [GPa]	τ [s]
Rod (N=5)	37±7	6.4±2.2	4.2±0.4	443±87
Interrod (N=5)	31±8	4.5±1.4	3.4±0.7	423±148
p-value	1.000	0.133	0.079	0.801

For the analysis of creep compliances, the data from point A to point B of Fig. 4.1 (b)) are plotted as h_t versus t to be analyzed with different combinations of spring, slider, Kelvin-Voigt bodies and dashpot using Eq. (2.21). Two example curves of h_t versus t, each for enamel rod and interrod region are plotted in Fig. 4.3 (a). When

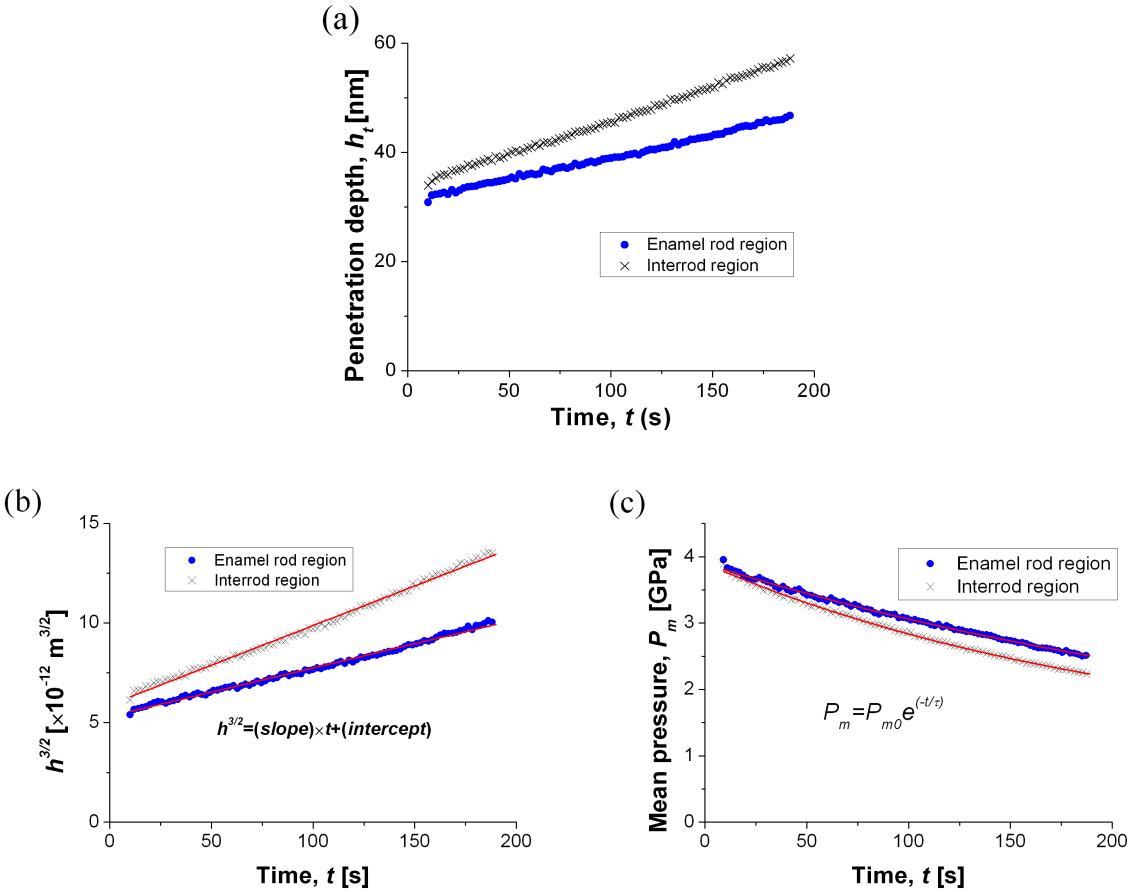

Figure 4.3.: Two example curves of h_t versus t under constant load of 500 µN, each for enamel rod and interrod region and the corresponding (b) ${h_t}^{3/2}$ versus t (to calculate C_0, η according to Eq. (4.1) and (c) P_m versus t (to calculate the effective relaxation time constant according to DM model in Eq. (2.23)). The red solid lines in (b) and (c) are the fitted curves according to the formula shown in the graphs.

Kelvin-Voigt bodies were included in the analysis, the creep compliance and the time constant were negative, thus unrealistic. The best fit was the combination of a spring, a slider and a dashpot with R^2>0.99 (R^2=1 means perfect fitting) with the equation

$$h_t^{\frac{3}{2}} = \left[\frac{3P_{max}}{8\sqrt{R}} \cdot \frac{1}{\eta}\right] t + \frac{3P_{max}}{8\sqrt{R}} \left[C_0 - \frac{t_R}{2\eta}\right] \tag{4.1}$$

Plotting $h^{3/2}$ versus t yields a linear equation, where the slope $\left[\frac{3P_{max}}{8\sqrt{R}} \cdot \frac{1}{\eta}\right]$ is first

used to calculate the viscosity η whereas the intercept $\frac{3P_{max}}{8\sqrt{R}}\left[C_0 - \frac{t_R}{2\eta}\right]$ is used to calculate C_0 according to Eq. (4.1). The example of such curve fittings are shown in Fig. 4.3 (b). (Note: one may question why a time-dependent property, η already exists in Eq. (4.1) even at $t = 0$ which is unrealistic. If we re-call what was mentioned in Chapter 2.2.5, an instantaneous step change from 0 to P_{max} is difficult to realize and therefore the term $\frac{c_v \cdot t_R}{2}$ where $c_v = 1/\eta$ and t_R is the 10 s rising time were included in the creep compliance equation Eq. (2.21) and also Eq. (4.1). Consequently, the term η already exists even at $t = 0$.) For the analysis of stress relaxation, the DM model (Eq. (2.23)) is found to yield better fitting than the KWW model (Eq. (2.22)). The fitting with the DM model generates a curve with R^2>0.99, examples are shown in Fig. 4.3 (c). The $1/C_0$, the viscosity, the instantaneous stress P_{m0} and the stress relaxation time constant of both regions show no statistically significant difference between the rod and interrod regions and are listed in Table 4.2.

Although load reduction occurred during the holding stage of the load-hold-unload profile (Fig. 4.2 (b)) due to the relaxation of the spring holding the transducer inside the nanoindenter, such load reduction happened with 486-491 μN at point A and dropped to 461-477 μN at point B, and is deemed insignificant in influencing the results in this study.

4.3. Discussion

Two values of elastic moduli are reported here, $E_{\mathrm{r,loading}}$ and $E_{\mathrm{r,unloading}}$. The initial loading curves are generally more accurate to calculate E_r than the unloading curves because an unloading curve might be influenced by creep resulting in an underestimate of the $E_{r,unloading}$ values. (In principle, the extend of the influence by creep could be estimated based on the comparison between the duration during unloading with the

time constant from the creep experiments. However, the time constants of stress relaxation in Table. 4.2 could not be used as a direct comparison here since they were calculated based on having a constant load of 500 μN whereas the unloading curves used for $E_{r,unloading}$ calculation in Tab. 4.1 were unloaded from 400 μN to 0 μN. Anyway, the nanoindentation curves in Fig. 4.2 (a) do not show significant round shape (a 'nose') at the beginning of the unloading curve), which sometimes round backward and gives a negative stiffness value and is typically found in materials of significant viscoelastic behaviors [140, 141]. Therefore the influence of creep on the $E_{\mathrm{r,unloading}}$, if exists, is not very remarkable.) E_{r} and H in the enamel rod regions are statistically significantly higher than the interrod region. The difference could be due to the difference of crystallite orientation or difference in protein contents. Knowing that E_{r} and H for a single crystal hydroxyapatite changes from E=162±1.9 GPa and H=14.8±0.1 GPa where the test direction was parallel to its c-axis and E=127.2±10.4 GPa and H=9.5±1.5 GPa for the test direction being perpendicular to its c-axis (P<500 μN with a Berkovich indenter) [122], the relatively smaller difference in Tab. 4.1 might be due to the difference of crystallite orientations between the enamel rod and interrod region, and not necessarily due to the different amounts of protein. The big differences reported by Ge et al. [139] with E and H being 50% lower in the interrod regions are not observed in our study. The reason might be related to the larger indentation area in our study thus not resolving the protein sheath as well. The residual impression of the indentation of Ge et. al on protein sheath can be approximated as an equilateral triangle with sides of 125 nm each, which makes a contact area of <7000 nm^2. The contact area in this study is at least $\pi\times$(200 nm)^2=125663 nm^2 and thus, is one order of magnitude larger.

The load-hold-unload loading function was able to observe significant different energy dissipation behaviors between enamel rod and interrod regions. The U_{Inel} in the interrod region is significantly higher than the enamel rod region. This could be

attributed to the unfolding and stretchings of the proteins or even their sliding between the crystallites as the interrod region is expected to have a higher amount of organics than the enamel rod region too. Compared to the load-unload profile, the U_{Inel} in the interrod region under the load-hold-unload profile with a dwell period increases more significantly than in the enamel rod region. Dislocation movement or fracture in hydroxyapatite is unlikely since the elastic/inelastic transition of hydroxyapatite for such a contact radius (≈200 nm) is 10 GPa [142], while the highest mean pressure in this study was only ≈5 GPa.

If the inelastic energy dissipation is attributed to protein bonds unfolding alone, the question that arises is how many protein bond openings were involved under the utilized loading profiles? For a simple calculation, the inelastic energy dissipation of the enamel rod region from the load-unload profile, U_{Inel}=2.4 pJ (Table 4.1) is used. It has been shown in a previous study that an applied load of 0 pN to 204 pN is necessary to open a single I27 protein bond by 20 nm [143]. Therefore, the energy used to open a single protein bond is $(0.5) \times (204pN) \cdot (20nm) \approx 2 \times 10^{-6}$ pJ. (Even though the single I27 protein bond opening did not exhibit linear elastic behavior, the calculation is reasonable to estimate the amount of energy under the load-displacement curve [143].) Assuming that the enamel's proteins exhibit similar protein bond opening behavior as I27 protein, the number of the protein bonds unfolded is then estimated as (2.4 pJ)/(2×10^{-6} pJ)=1.2×10^{6}. The volume fraction of enamel's organic matters is estimated as follows: assuming that the cross section of infinitely long enamel crystallites are 30-50 nm in diameter and are enveloped by a 1 nm thick organic layer, the area fraction of organic matters is 0.04-0.06. This organic matters area fraction of ≈0.05 can also be approximated as the volume fraction. Of these organic matters, ≈57% are peptides/proteins (Chapter 2.1.3.2), so the volume fraction of peptides/proteins are ≈0.03. Next, we are interested to calculate the number of protein bond openings per volume under the single load-unload profile

at the enamel rod region. We further estimate the volume displaced by an indenter with R=889 nm for a penetration depth of 30 nm by using the standard equation to calculate the volume of a partial sphere as $V = \pi \cdot {h_t}^2 \cdot (3 \cdot R - h_t)/3$=2485314 nm^3. So the number of protein bond openings per volume of proteins within material displaced by the indenter during the 10 s loading time is $1.2 \times 10^6/(0.03 \cdot 2485314 \cdot 10)$=1.6 protein bonds unfolding/(nm^3 proteins $\cdot$ s). This number might be lower when we consider the volume affected by the applied stress does not only involve the volume calculated above (displaced by the indenter) but also the volume just below and nearby the indenter. Besides part of the energy could have been used to cause sliding between crystallites. Nevertheless, this gives an estimation of the number of protein unfoldings which could happen that contribute to the inelastic energy dissipation.

The inelasticity index (U_{Inel}%) from the load-hold-unload profile is ≈70% and is found to be similar with the ≈70% reported by He and Swain when a 5 μm spherical indenter was used to load on enamel in 10 s to a P_{max} of 300 mN and unloaded again to 1 mN in 10 s [96]. When a material is stressed beyond its' elastic limit, its U_{Inel}% increases with the stress/strain level until it reaches a plateau value. Such relationship has been shown previously on a single tropocollagen [137]). Enamel is expected to exhibit the same materials behavior. The 70% in this study is either the maximum U_{Inel}% that could be achieved by enamel with increasing stress-strain level or an intermediate value.

Under the load-hold-unload profile, the calculation of U_{Inel} utilized every data points of each corresponding curve in Fig. 4.2 (b) and has observed statistically significant difference between the enamel rod and the interrod regions. For the calculation of creep, viscosities and stress relaxation behaviors, only the data from the dwell region from point A to point B (holding at P_{max}) are involved in the calculation and have not observed statistically significant difference between the two investigated regions. For creep, damage that can be attributed to microcracks and/or voids [144] is unlikely to

be a significant contribution to the measured creep. In a previous study [145], burnt and dry enamel specimens exhibited lower creep compared to sound enamel when held under a constant load of 250 mN for 900 s with a Berkovich indenter. If the increased penetration depth in that study was significantly caused by damage, burnt and dried samples should have exhibited higher creep compared to sound enamel which however was not the case.

The viscosities calculated when the creep responses were considered as a spring, a slider and dashpot in series (η_{rod}=6.4±2.2×10^{12} Pa.s; $\eta_{interrod}$=4.5±1.4×10^{12} Pa.s) are lower than the values recorded by Mencik et al. [99], whose studies involved a contact area of several enamel rods, probably because different values of viscosities prevail at different length scales. Under the contact conditions of our experiment (a length scale of ≈400 nm and a contact pressure of ≈5 GPa), viscoplastic process prevails, whereas viscoelastic and viscoplastic processes prevail at a bigger length scale and load level in the case investigated by Mencik et al. [99]. The viscoelastic values in this study were also found to be lower than the value of 1.1×10^{15} Pa.s by Schneider et al. [132], whose value was calculated based on a pure viscosity model.

4.4. Conclusions

This study used spherical indentation of ≈1 μm tip radius to probe the mechanical properties of enamel rod and interrod regions of enamel. The elastic modulus and hardness in the enamel rod regions are significantly higher than in the interrod region. When the applied stress was held for a longer period, the inelastic energy dissipation in the interrod region is significantly higher than in the enamel rod region. The increase in inelastic energy dissipation over time is significantly higher in the interrod region than in the enamel rod region. From the creep response, the calculated viscosity and the

time constant for stress relaxation of enamel rod and interrod regions are statistically similar.

5. Sub-10 μm toughening and crack tip toughness

Throughout our lifetime, mastication loadings result in a distribution of cracks in enamel [146, 147]. Despite this, enamel could be considered as a damage-tolerant material against crack propagation due to the following reasons. Small cracks in enamel of 40 μm deep and 8 μm wide were observed to be occluded by mineral deposition, proposed as a key phenomenon to repair tiny enamel cracks in vivo [148]. Studies of ex-vivo cracks over larger distances have shown that enamel exhibits R-curve behavior; the stress intensity increased from values between 0.5 and 1.5 MPa$\sqrt{m}$ up to 2.5 MPa$\sqrt{m}$ at 1.5 mm crack extension in human enamel [9] and up to 4.4 MPa$\sqrt{m}$ at 500 μm crack extension in bovine enamel [8]. The reported toughening mechanisms are crack bridging of tissue ligaments of 10 μm wide or bigger, microcracking, possible bridging by protein ligaments and crack deflection promoted by enamel rod decussations mainly existing in the inner enamel [149, 150]. The observed toughening mechanisms in enamel are summarized in Tab. 5.1. Although the smallest structural units of enamel are of nanometer-sized, toughening mechanisms of sub-10 μm-scale in enamel has never been investigated.

It is well-known from ceramic materials that toughness measurements with Single-

Edge-Notch-Beam (SENB) or Compact-Tension (CT) specimens are usually not able to measure the crack tip toughness, K_{I0}, in particular when steep crack resistance curves prevail [151–153]. In brittle materials the most commonly used method to measure K_{I0} is to measure the crack opening displacement (COD) in the crack tip region with high spatial resolution using an atomic force microscope (AFM) or scanning electron microscope (SEM) [154–157]. With this information, Irwin's crack tip solution [109, 110] is applied to evaluate K_{I0}.

In enamel, a crack tip toughness study based on COD measurements is missing which is the objective of this investigation. AFM is used as a high spatial resolution tool for COD measurement to calculate K_{I0} [109, 110]. The information is also used to apply a cohesive zone model developed by Goodier and Field [158–160] for the Dugdale-Muskhelishvili crack model [161, 162] to compute the closure stresses at the crack tip, the cohesive zone width and length, as well as the corresponding crack tip toughness. In addition to AFM, SEM is also used to investigate toughening mechanisms around and behind the crack tip.

In a number of other studies [8, 9, 149, 150] enamel's toughening mechanisms are already reported but not with a special focus on the different lengths scales. As enamel

Table 5.1.: Previously observed toughening mechanisms in enamel.

Crack bridges	- Uncracked ligaments of 10-20 μm in width [8, 9, 149, 150] - Crack bridging zone of 30-100 μm in length [150]
Microcracks	- Water droplets adjacent to a crack indicate microcracks [149] - 15% of the crack paths [9]
Protein bridging	- Observed to span across 700-900 nm crack opening [9]
Crack deflection	- Mostly in inner enamel due to rod decussations [9, 149, 150] - 70% crack deflection reduces >30% the crack tip stress intensity [9]

is hierarchically structured with nanometer-sized basic structural units, the objective is to identify the specific toughening mechanisms of sub-10 μm-scale for the first and second hierarchical level as defined in Section 2.1.1 using AFM and SEM.

This chapter is based on the following published manuscripts:

- Ang, S. F.; Schulz, A.; Pacher Fernandes, R.; Schneider, G. A. **Sub-10-micrometer toughening and crack-tip toughness of dental enamel.** *Journal of the Mechanical Behavior of Biomedical Materials*, 4(3), 423-432 (2011).

5.1. Materials and methods

5.1.1. Materials

Mature bovine incisors were used due to their larger amount of enamel compared to human teeth. The bovine teeth are stored in Hanks' Balanced Salt Solution (HBSS) before sample preparation. The rectangular prisms of $\approx 3 \times 2 mm^2$ were first cut out from the labial side of mature bovine incisors (Fig. 5.1 (a) by using a saw (Brüder Mannesmann 92571, Germany) under water irrigation. The cows were sacrificed between 3-4 years old. The specimen surface was first ground with an abrasive paper of grit 4000. It was further polished with diamond suspensions of 1 μm, 0.25 μm and finally 0.05 μm (Bühler, Germany). The polished tooth was then glued face-up on a steel plate with wax for subsequent investigation on the same day. A total of 15 specimens were investigated (13 specimens under AFM and 2 specimens under SEM).

5.1.2. Methods

The methodology for vickers indents and the AFM and SEM investigations are described here.

5.1.2.1. Vickers indents and AFM measurements

The freshly polished enamel surfaces were introduced with Vickers indents of 400 g for 10 s (3212, Zwick GmbH, Germany). An example is shown in Fig. 5.1 (b). Without the introduction of the Vickers indent, no cracks were observed on the specimens following the same polishing procedures and examined under AFM with the same experimental conditions. The weight of 400 g was selected because the induced crack lengths were long enough that the crack lengths to indentation size ratio was bigger than 3. Yet, they should not be too long; due to the fact that scanning of high resolution pictures with AFM is extremely time consuming, excessive crack lengths would lower the chance to find the crack tip within one day after sample preparation and therefore are undesirable. 3-5 indents were made on the polished surface of each specimen; they were at least 500 μm apart. Only one specimen was investigated within a day. No samples are re-used overnight because polished samples, if left immersed in HBSS solution for rehydration overnight, were covered with a layer of salt deposition that precludes nanoscale observation of the sample surface under AFM. Only one crack (from one specimen) could be investigated in one day. The indents were first observed under a light microscope (Aristome, Ernst Leitz Wetzlar, Germany). Then, the crack profiles were examined under AFM (Dimension 3100, Veeco, USA) in tapping mode. Cracks with insufficient crack lengths were discarded. We calculated the total crack lengths by summing up the lengths under the optical microscope attached with the AFM system and the AFM topography scans. All the measurements were carried out in an air environment.

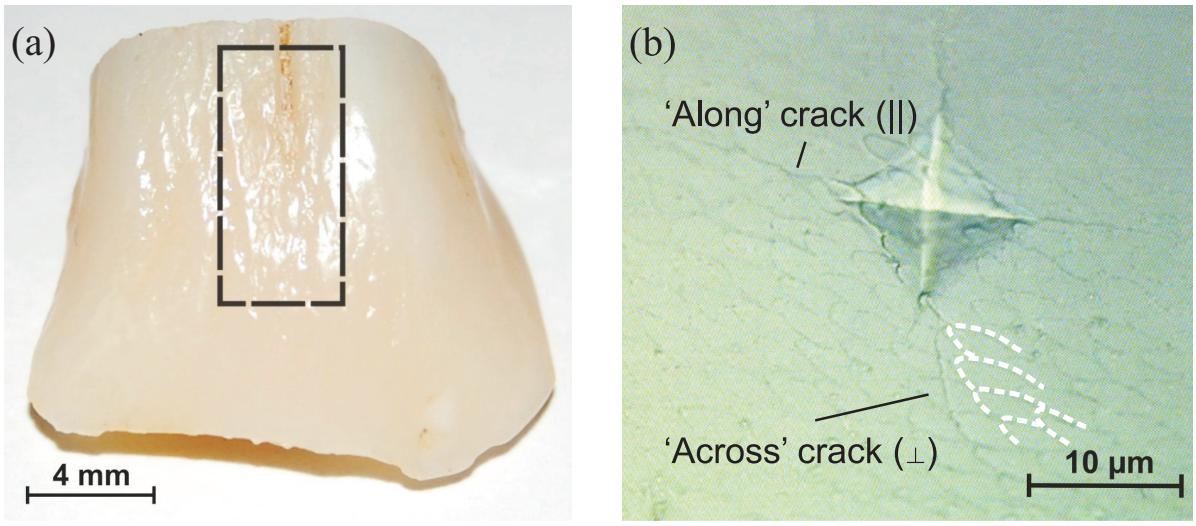

Figure 5.1.: (a) A bovine tooth. The indicated area was cut out and polished for investigation. (b) A Vickers indent observed under an optical microscope. The 'along' crack (going mainly along enamel rod boundaries) and the 'across' crack (going mainly across the enamel rods) are labeled. The results for both types of cracks are labeled with subscript '(||)' and '(⊥)' in the article.

As the darker contrast in the AFM topography images belongs to lower topography levels, the crack can be identified as a dark contrast due to the deeper position of the AFM tip. An X-Y sample stage was used to trace the cracks away from the Vickers indents as far as the crack tips. Super sharp tips with tip apexes <10 nm (SuperSharp-Silicon, Nanosensors, Switzerland) were used together with a slow scanning frequency of 0.2 Hz to acquire high resolution images (an example is shown in Fig. 5.2 (a)). The height profiles across the crack at the desired positions are later obtained from the topographical images to measure the COD between two opposing crack walls ($2u_I$) as well as the height difference ($2u_{\mathrm{III}}$) (Fig. 5.2 (c)), both as a function of the distance from the crack tip (X). The COD measurement was stopped when the crack could no longer be differentiated from the surface roughness, this position is taken as the zero position for X (Fig. 5.2 (d)). The lateral resolution of the AFM measurement primarily depends on the tip radius, which is <10 nm here [156]. Therefore the uncertainty in the COD measurement is ≤10 nm. The vertical resolution of the AFM measurement is of sub-

nanometer level [163].

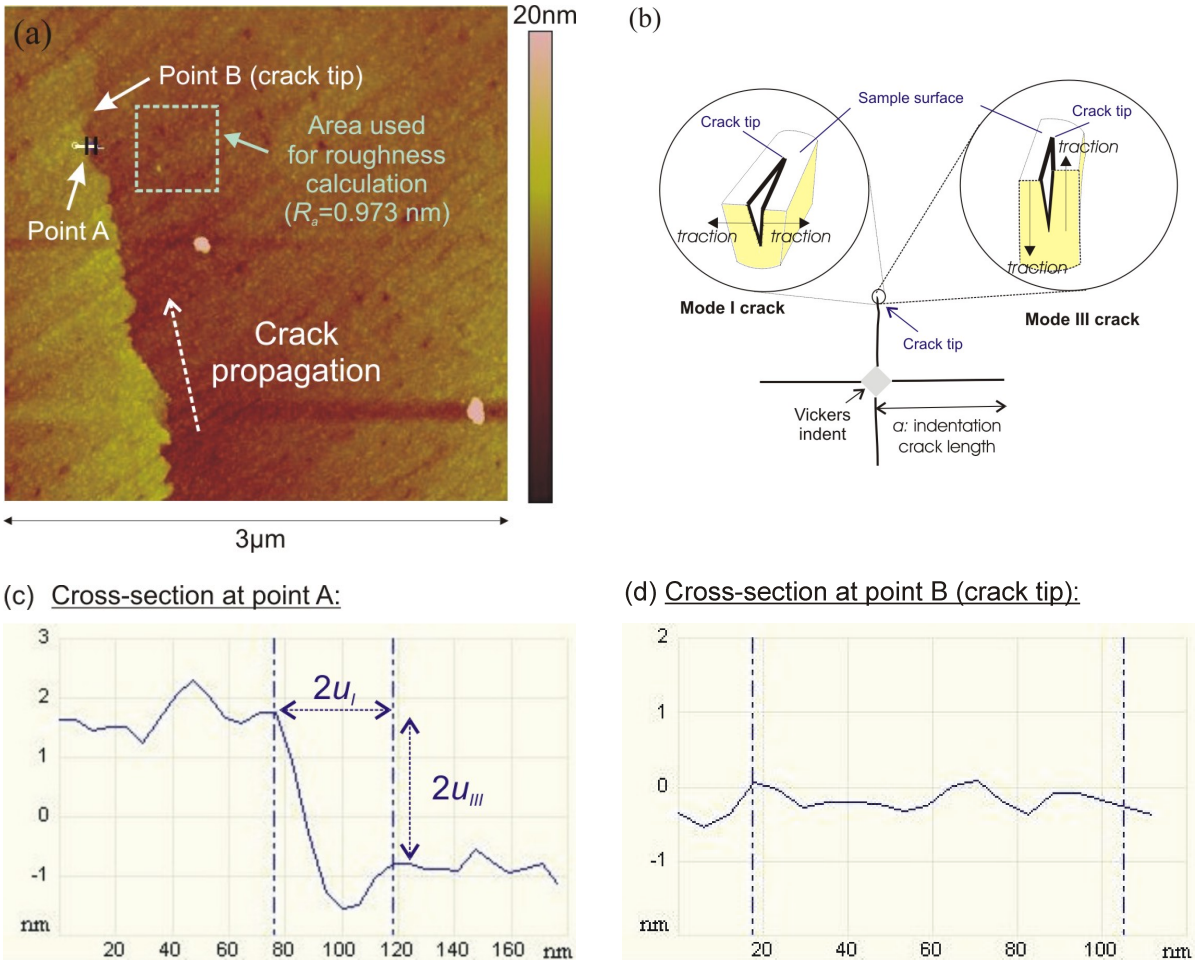

Figure 5.2.: COD measurements. (a) An AFM topography image of a well-polished enamel surface with a crack and its crack tip. The rectangular box is a chosen area for roughness analysis (R_a=0.973 nm). (b) Illustration of the mode I and mode III fracture at the crack tip of a Vickers indent. (c) A cross-sectioned topography profile corresponding to the white line at point A in (a), used to calculate u_I and u_{III} of that point, for the calculation of K_{I0} and K_{III0} respectively. (d) A similar cross-sectioned topography profile was done at point B in (a) where the crack could not be differentiated from the surface roughness and is defined as the crack tip for the crack. The AFM measurements have sub-nanometer vertical resolution [163].

5.1.2.2. SEM investigations

Vickers indents (1 kg, 10 s) were made on the 2 polished specimens. A higher weight of the Vickers indent load (1 kg) was chosen so that the resulting crack profiles are longer and clearer for observation under SEM. Two indents per specimen were made. The surface were cleaned with ethanol and dried for one day in a desiccator. The samples were contacted with silver paint at the edges and carbon pad at the bottom to avoid the build up of charges during the measurements. SEM images were recorded using the secondary electron signal with an acceleration voltage of 5 kV.

5.2. Results

The surface roughness, R_a of our enamel specimens over an area of 500×500 nm^2 is less than 1 nm (Fig. 5.2(a)). R_a is the arithmetic average of the absolute values of the surface height deviations measured from the mean plane. Out of the 13 specimens investigated under AFM, only 6 CODs are used (Tab. 5.2). For the other cracks, either the observed crack tips were too close to microcracks or bridges, the crack lengths were too long and the crack tips could not be traced until the end of the day, or when the crack tips were identified, the crack lengths were too small. The cracks propagating mainly along rod boundaries are termed 'along' (Fig. 5.1 (b), Fig. 5.6 (a)) whereas those propagating across the rods are termed 'across' (Fig. 5.1 (b), 5.6 (b), 5.7 (a)). The terms 'longitudinal' and 'transverse' [8] (also illustrated in Fig. 5.9) are not used because they usually describe the rod orientations relative to the cross-sectional plane but not the manner of crack propagation. The enamel rods in this study are oriented in an oblique orientation relative to the sample surface plane, judging from their prolonged shape in the pictures (Fig. 5.1 (b), 5.6 and 5.7), hence neither 'longitudinal' nor 'transverse'.

The 'along' and 'across' cracks are typically longer than 100 μm and 50 μm respectively. Cracks with insufficient crack lengths are discarded. The results for 'along' and 'across' cracks are labeled by subscripts '($\parallel$) ' and '($\perp$)' accordingly in this study.

5.2.1. Determination of crack tip toughness

The measured in-plane and out-of-plane displacements u_I and u_{III} (Fig. 5.2 (c)) are used to determine the mode I and mode III crack tip toughness respectively. Recall that mode I fracture is a tensile mode separation where the traction forces act to open crack surfaces directly apart from each other, whereas mode III fracture is a shear mode separation where the traction forces act parallel with the crack plane and also parallel with the crack front (Fig. 5.2 (b)).

The measured half crack opening profiles (u_I) versus crack length behind the crack tip (X) are plotted in Fig 5.3 (a). (The data of u_I versus X of all cracks are listed in Appendix C.) The u_I and X values are used to calculate $K_{\mathrm{I0,Ir}}$ by the following equation that describes the near-tip COD profile for a straight crack [109, 110],

$$u_I = \frac{K_{I0,Ir}}{E}\sqrt{\frac{8X}{\pi}}\left(1-\nu^2\right) \tag{5.1}$$

u_I is the half COD between two opposing crack walls (u_I=COD/2), X is the distance from the crack tip, E and ν are the elastic modulus and Poisson's ratio of enamel and are taken as E=87 GPa [164] and ν=0.23 [165]. (The lower case annotation 'Ir' indicates that the values are calculated based on Irwin's parabolic 'near-field' solution). The value of E=87 GPa is the average elastic modulus values derived from both the longitudinal and transverse orientations of enamel from Vickers indentation under comparable load as in our study [164]. The crack opening up to 10 μm behind the crack tip

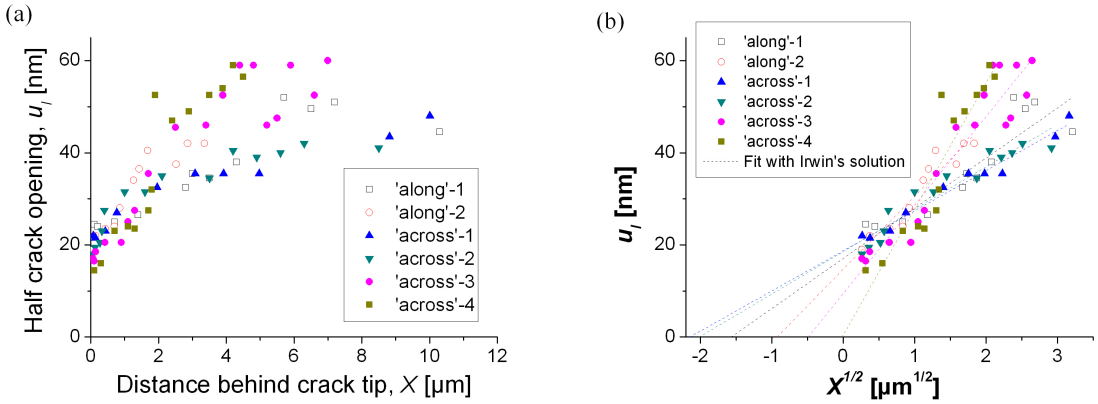

Figure 5.3.: The calculation of $K_{\mathrm{I0,Ir}}$. (a) u_I versus X profile for all cracks. The crack opening $2u_I$ is around 40 nm and does not lie within the measurement uncertainty of <20 nm. (b) u_I versus $\sqrt{X}$. The slopes are used to calculate $K_{\mathrm{I0,Ir}}$ with Eq. (5.1).

is not associated with observable ligament bridges and is used in the calculation. A key assumption in utilizing the Irwin's 'near-field' solutions is that the crack walls behind the tip remain free of traction [109, 110]. u_I versus $\sqrt{X}$ was plotted (Fig. 5.3 (b)); the slopes are used to calculate $K_{\mathrm{I0,Ir}}$ based on Eq. (5.1) but without forcing the intercept-y to zero. A total of 6 crack tip toughness measurements are reported here: 2 'along' cracks and 4 'across' cracks. Both of them show similar values with $K_{\mathrm{I0,Ir(\|)}}$=0.63-0.91 MPa$\sqrt{m}$ and $K_{\mathrm{I0,Ir(\perp)}}$=0.50-1.58 MPa$\sqrt{m}$ (Tab. 5.2).

Similar to Eq. (5.1), the mode III crack tip toughness, $K_{\mathrm{III0,Ir}}$ can be described by the following equation [109, 110], with u_{III} being the height difference of two crack walls (Fig. 5.2 (c)),

$$u_{III} = \frac{K_{III0,Ir}}{E}\sqrt{\frac{8X}{\pi}}\,(1+\nu) \tag{5.2}$$

Similarly, u_{III} versus $\sqrt{X}$ were plotted to calculate $K_{\mathrm{III0,Ir(\|)}}$=0.02-0.03 MPa$\sqrt{m}$ and $K_{\mathrm{III0,Ir(\perp)}}$=0.05-0.15 MPa$\sqrt{m}$. The results are summarized in Tab. 5.2 too. The $K_{\mathrm{III0,Ir(\perp)}}$, values are at least 50% higher than $K_{\mathrm{III0,Ir(\|)}}$. However, these values are an

order of magnitude smaller than the values of $K_{\mathrm{I0,Ir}}$, and could be deemed negligible.

Table 5.2.: The values of crack tip toughness ($K_{\mathrm{I0,Ir}}$ and $K_{\mathrm{III0,Ir}}$) based on Irwin's 'near-field' solutions [109, 110], and the crack closure stress near the crack tip ($\overline{\sigma_{\mathrm{br}}}$), the width ($\delta$) and length ($\lambda$) of the cohesive zone and the corresponding crack tip toughness based on cohesive zone solutions developed for the Dugdale-Muskhelishvili crack model by Goodier and Field [158–162].

Crack	**Irwin's solution**		**DM crack model's solution**			
	$K_{\mathrm{I0,Ir}}$	$K_{\mathrm{III0,Ir}}$	$\overline{\sigma_{\mathrm{br}}}$	λ	$\delta/2$	$K_{\mathrm{I0,cz}}$
	(MPa$\sqrt{m}$)	(MPa$\sqrt{m}$)	(MPa)	(μm)	(nm)	(MPa$\sqrt{m}$)
'along'-1	0.63	0.020	163	10.06	22	0.81
'along'-2	0.91	0.028	734	1.61	16	1.48
'across'-1	0.50	0.050	234	6.55	21	0.95
'across'-2	0.53	0.147	433	3.15	18	1.21
'across'-3	1.11	0.054	770	1.24	13	1.36
'across'-4	1.58	0.079	574	1.54	12	1.13

5.2.2. Cohesive zone

The u_I versus X plot (Fig. 5.3 (a)) seemingly shows a $u_I \approx 20$ nm half opening at the beginning of the measured COD (at $X=0$). This crack opening ($2u_I$) is around 40 nm and does not lie within the measurement uncertainties of $\leq$10 nm. We interpret this finite crack tip opening, δ as the end of a cohesive zone length λ with constant bridging stresses $\overline{\sigma_{\mathrm{br}}}$, (Fig. 5.4 (a) and (b)). The load-displacement solution developed by Goodier and Field for the Dugdale-Muskhelishvili crack model (Fig. 5.4(b)) [158–162] is used to calculate $\overline{\sigma_{\mathrm{br}}}$ and λ,

$$u_I = \frac{a\overline{\sigma_{\mathrm{br}}}}{\pi E'}\left(cos\phi \cdot \ln\frac{sin^2(\theta-\phi)}{sin^2(\theta+\phi)} + cos\theta \cdot \ln\frac{(sin\theta+sin\phi)^2}{(sin\theta-sin\phi)^2}\right) \tag{5.3}$$

where $\phi = \arccos\left(\frac{a-X-\lambda}{a}\right)$, $\theta = \arccos\left(\frac{a-\lambda}{a}\right)$ and $E' = \left(\frac{E}{1-\nu^2}\right)$.

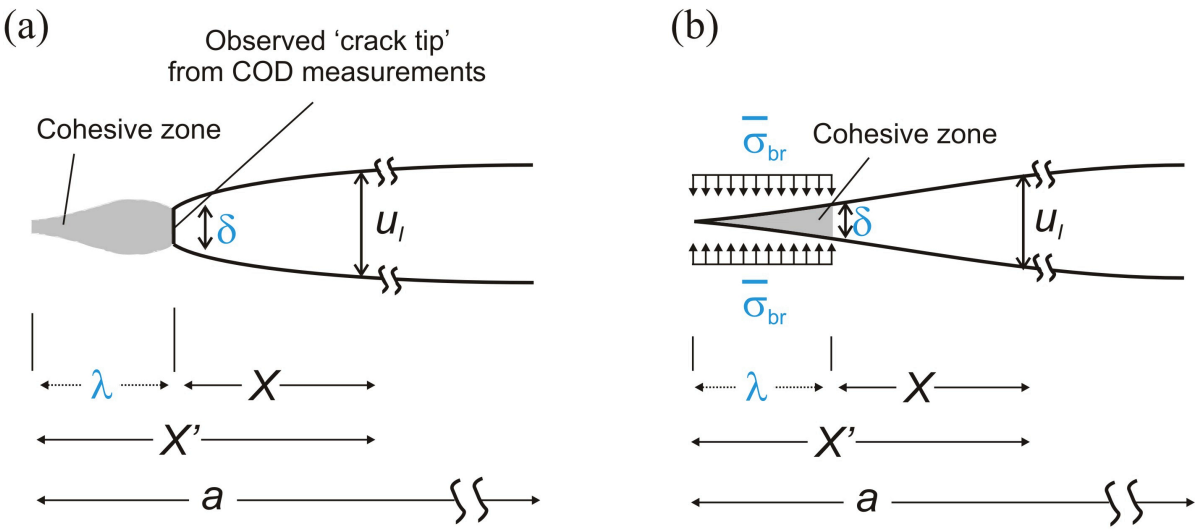

Figure 5.4.: Model of a Dugdale-Muskhelishvili (DM) crack. (a) The actual crack and the cohesive zone ahead of the crack tip. (b) the DM model.

The crack length a is taken as $a_{(\|)}$=100 µm for along cracks and $a_{(\perp)}$=50 µm for across cracks because these were the minimum crack lengths observed under the light microscope. (When the values of a differ by ±20 µm from the above values, the results of $\overline{\sigma_{\mathrm{br}}}$, λ, $\delta/2$ and $K_{\mathrm{I0,cz}}$ in Tab. 5.2 differ by <5%). Since the half CODs at X=0 in Fig. 5.3 (a) are interpreted as the finite crack tip opening of the cohesive zones δ, λ has been added as X-offset in Eq. (5.3) to locate the tip of the cohesive zone. The onset of the crack is shifted leftward and re-labeled with X' where $X' = X + \lambda$ (Fig. 5.4 (a) and (b)). Since the model is only valid for the region near the crack tip, only data points up to 4.3 µm behind the crack tip (the length scale of one enamel rod) are used for the fitting procedures. MATLAB's curve fitting toolbox with custom equations was used for the curve fitting. The fitting program iterates for the same values of $\overline{\sigma_{\mathrm{br}}}$ and λ within the huge range of input values of $\overline{\sigma_{\mathrm{br}}} \subseteq$ [1-2000 MPa] and $\lambda \subseteq$ [0.1-50 µm], resulting in $\overline{\sigma_{\mathrm{br}(\|)}}$=163-734 MPa, $\overline{\sigma_{\mathrm{br}(\perp)}}$=243-770 MPa and $\lambda_{(\|)}$=1.6-10.1 µm, $\lambda_{(\perp)}$=1.2-6.5 µm (Tab. 5.2). (The iterations gave the same values when wider range of starting values: $\overline{\sigma_{\mathrm{br}}} \subseteq$ [1-200,000 MPa] and $\lambda \subseteq$ [0.05-100 µm]. These ranges under consideration are sufficient because it is rather unrealistic for $\overline{\sigma_{\mathrm{br}}}$ to be smaller than 1 MPa or bigger than

200 GPa or for λ to be smaller than 50 nm (the diameter for a single enamel crystallite) or bigger than 100 μm, which is the maximum crack length.) The R^2 which defines the goodness of the fit is >0.84. $\delta/2$ is calculated from Eq. (5.3) by inserting X=0 and the corresponding values as $\delta/2$=12-22 nm (Tab. 5.2). So, $\delta/2_{(\parallel)}$=16-22 nm, $\delta/2_{(\perp)}$=12-21 nm. The data points together with the fitted curves based on Eq. (5.3) are plotted as u_I versus X' (Fig. 5.5 (a)).

The relationship

$$K_{I0} = \sqrt{\left(\frac{E}{1-\nu^2}\right) \cdot J_c} \tag{5.4}$$

with $J_c = 2\int_0^{u_I} \sigma(u_I) du_I$ for the near-tip zone [166] can be used to calculate crack-tip toughness based on the calculated $\overline{\sigma_{\mathrm{br}}}$ and δ values. Since the bridging stress, $\overline{\sigma_{\mathrm{br}}}$ in the applied cohesive model is constant, $J_c = 2 \cdot \overline{\sigma_{\mathrm{br}}} \cdot u_I = \overline{\sigma_{\mathrm{br}}} \cdot \delta$. Therefore, the crack tip toughness is calculated according to the equation,

$$K_{I0,cz} = \sqrt{\overline{\sigma_{\mathrm{br}}}\delta \frac{E}{1-\nu^2}} \tag{5.5}$$

as $K_{\mathrm{I0,cz}}$=0.8-1.5 MPa$\sqrt{m}$ (Tab. 5.2). (The lower case annotation 'cz' indicates that the values are calculated based on the cohesive zone solutions.) $\overline{\sigma_{\mathrm{br}}}$ and $K_{\mathrm{I0,cz}}$ are plotted versus λ for better visualization (Fig. 5.5 (b)). (Alternatively, the stress intensity contributed due to the bridging stress inside the cohesive zone can also be calculated based on the weight function [167]

$$\Delta K = \sqrt{\frac{2}{\pi}} f \int_0^{\lambda} \frac{\sigma(x)}{\sqrt{x}} dx \tag{5.6}$$

where f is the area fraction of the reinforcements on the crack plane [168]. The denomi-

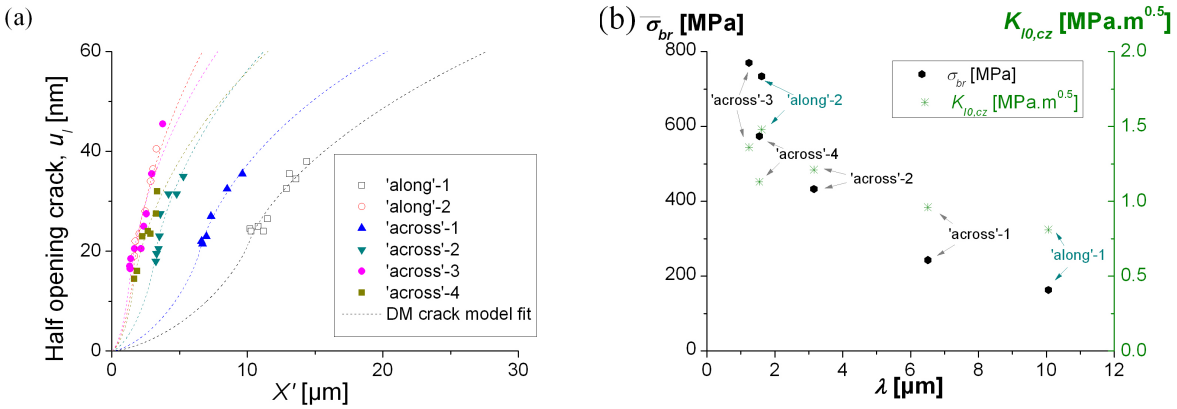

Figure 5.5.: Cohesive zone parameters fitting. (a) u_I versus X' profile for the original data points used for fitting with DM's cohesive zone solutions together with their fitted curves (dashed lines) ($X' = X + \lambda$). (b) $\overline{\sigma_{\mathrm{br}}}$ and $K_{\mathrm{I0,cz}}$ versus λ.

nator is replaced by some function of x but for $\lambda \ll a$, all formulae will lead to Eq. (5.6) as the limit. When traction is assumed to be uniform, $\sigma(x)=\overline{\sigma}$, integrating Eq. (5.6) gives

$$\Delta K = 2\overline{\sigma} f \sqrt{2\lambda/\pi}. \tag{5.7}$$

Eq. (5.7) is shown here because it will be used in the chapter of Discussion. Eq. (5.7) is not used to calcualte $K_{I0,cz}$ because f is not known. Eq. (5.5) and Eq. (5.7) are equivalent as long as they are used to calculate the stress intensity caused by the bridging stress in the cohesive zone. The selection would depend upon experimental or mathematical convenience.)

5.2.3. Toughening mechanisms

Crack bridging and microcracks of different lengths scales are identified. Crack bridges on the length scale of one enamel rod (≈3 μm), bundles of crystallite fibers (300-400 nm) and approximately one crystallite fiber (≈85 nm) were observed (Fig.

5.6). Similar to the bridges at multiple length scales, microcracks of ≈6 μm and 100-500 nm were detected (Fig. 5.7 (a) and (b)). Additionally, loosenings of groups of crystallite fibers (Fig. 5.7 (c)) are also observed. Fig. 5.7 (b) also shows possible indication of proteins. The crack paths show an undulatory pattern. The presence of crack bridging has been observed to significantly reduce mode III shear too (observed from the reduction of the surface level difference for both sides of the crack (Fig. 5.8)). In Fig. 5.8, the topography difference on both sides of the crack was bigger (indicated by the brightness difference) but the surface levels became similar towards the crack tip propagating across ligament bridges. This indicates that the mode III fracture was significantly reduced by the presence of crack bridging.

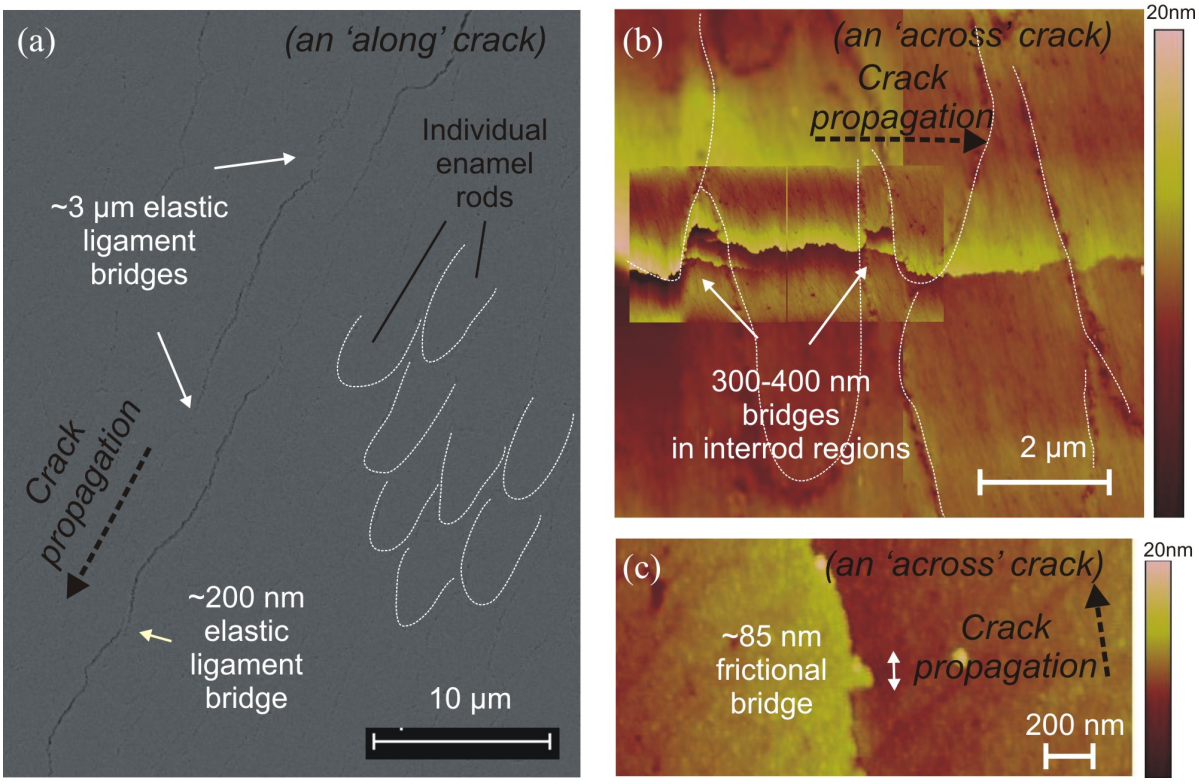

Figure 5.6.: Crack bridges in enamel. (a) ≈3 μm intact ligament bridges, (a) and (b) 200-400 nm bridges, (c) a nano-sized ≈85 nm frictional bridge corresponding to the length scale of one enamel rod, several enamel crystallites and approximately one crystallite respectively.

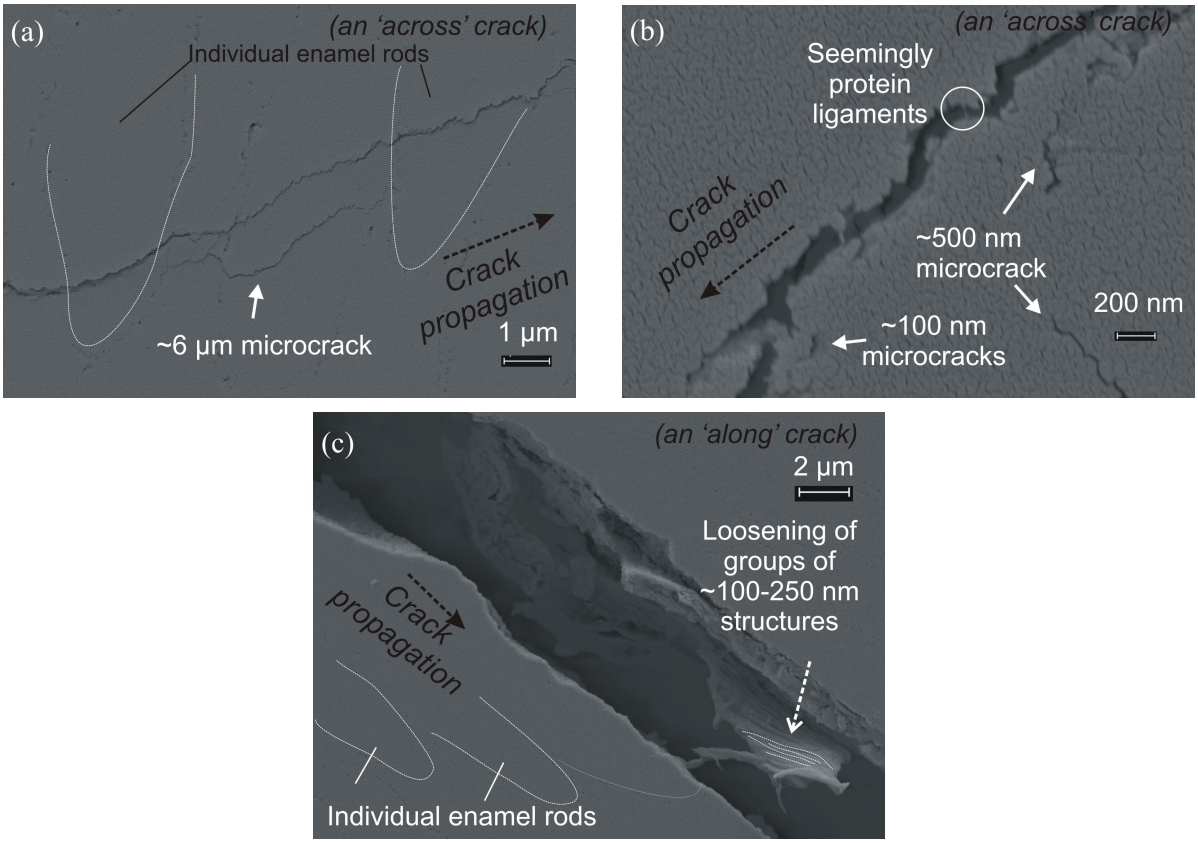

Figure 5.7.: Microcracks and seemingly protein ligaments. (a) A microcrack across a few enamel rods (≈6 µm) and (b) within an enamel rod at the interface of apatite crystallites (100-500 nm). The ligament inside the crack, circled in white in (b) is seemingly a protein ligament. (c) Loosening of groups of crystallites (≈100-250 nm) indicates the presence of microcracks.

5.3. Discussion

Enamel's crack tip toughness was reported as K_{I0}=0.5-0.8 MPa$\sqrt{m}$ in a previous study which is based on enamel CT specimens [9]. These lie at the lower range of our measured K_{I0}=0.6-1.6 MPa$\sqrt{m}$. The wide variations of our reported K_{I0} are hypothesized to be caused by different morphological surroundings around a crack tip and will be discussed in the second last paragraph of discussion.

A cohesive zone of 1-10 µm long and 24-44 nm wide with an average bridging stress of 163-770 MPa is calculated to occur at the crack tip. Inelastic processes prevail within

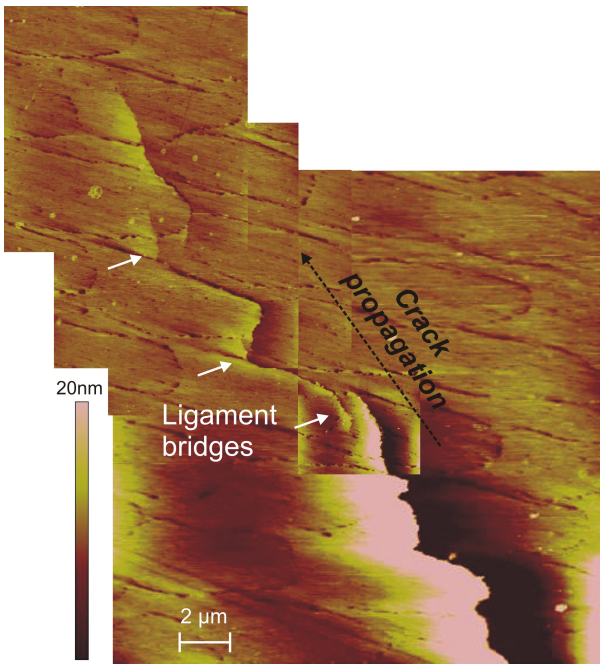

Figure 5.8.: The mode III fracture was significantly reduced by the presence of crack bridging. (The surface level difference of both side of the crack was bigger at the lower part of the image but the surface levels became similar towards the crack tip.

the cohesive zone which are decoupled from the linear-elastic field outside the zone [160]. Possible inelastic processes within the zone are the separation of the so-called 'sacrificial bonds' [13], protein bridging, protein breakage, microcracks, minerals ligament bridging and/or mineral fracture. An up to 10 μm long zone means that multiple crystallite nanofibers or even multiple enamel rods are included in the inelastic process and the bridging stress is not only caused by protein bridging alone. Experimental studies showed that the ultimate stress of proteins such as ligaments (mainly collagen), tendon (mainly collagen) and horn (mainly keratin) are 2.5-7 MPa, 70 MPa and 260 MPa respectively [5, 129, 130, 169] and are generally lower than the calculated 163-770 MPa. Secondly, the maximum stress intensity shielding contributed by the protein bridging can be estimated by using Eq. (5.7) with ΔK_{p} as the stress intensity due to protein bridging, $\overline{\sigma_p}$=2.5-260 MPa as the yield strength of protein, f_{p}=0.1 as the area fraction of protein bridging ligaments (estimated based on the volume fraction of protein in enamel), λ=1-10 μm

as the protein bridging zone length. ΔK_{p} is calculated as 0-0.13 MPa$\sqrt{m}$ and is much smaller than the crack tip toughness. Mineral fracture is unlikely to occur in the cohesive zone according to the following calculation. The theoretical strength of hydroxyapatite crystallites can be estimated by $\sigma_{\mathrm{m}} = E_{\mathrm{m}}/30$=4.3 GPa ($E_m$=129 GPa [142]). Assuming that a material's failure is due to the fracture of the mineral phase, the strength of different hierarchical levels can be calculated based on the formula $\sigma_{\mathrm{n+1}} = \psi \cdot \left(\frac{\sigma_{\mathrm{n}}}{2}\right)$, σ_{n} and $\sigma_{\mathrm{n+1}}$ the strength of the hierarchical structure n and n+1, ψ_{n} the volume fraction of minerals at hierarchical structure n [15]. ψ_{n} is assumed to be constant for all hierarchical levels and is taken as 0.9, ψ=0.9. Since a single crystallite fiber is level 0 [15], the strength of the first hierarchical structure level, multiple crystallites, can be estimated by using the formula $\sigma_1 = \psi \cdot \left(\frac{\sigma_0}{2}\right) = \psi \cdot \left(\frac{\sigma_{\mathrm{m}}}{2}\right)$=1.9 GPa. Similarly, the strength needed for mineral failure of the second hierarchical structure level, multiple enamel rods is $\sigma_2 = \psi \cdot \left(\frac{\sigma_1}{2}\right)$=0.9 GPa. Hence, the strength of the first hierarchical level is significantly higher than the calculated cohesive zone stresses, whereas the second hierarchical level has a strength close to the upper limit of the cohesive zone stresses.

Previous studies of enamel fracture have observed cracks more commonly along rod boundaries than running through rods [170]. 10-20 μm wide bridges in enamel have been observed in several previous experimental studies [8, 9, 149, 150]; they span across multiple rods. In this study, 3 μm wide bridges are observed along interrod regions which corresponds to the diameter of an enamel rod (Fig. 5.6 (a)). Approximately 200 nm long ligament bridges are also observed in the interrod region and encompass groups of crystallite fibers (Fig. 5.6 (a)). Even a single crystallite fiber in the enamel rod region is capable of forming nanoscale sized ≈85 nm bridges (Fig. 5.6 (c)).

Besides providing a weak interface to form bridges, interrod regions also reinforce enamel's structure by hindering crack propagation when a crack runs across them but not along them (Fig. 5.6 (b)). The rod-interrod boundaries are locations where an abrupt

change in crystallite orientation occurs [9, 89, 171], therefore crack propagation obstacles occur and a crack needs higher energy to propagate through them. The presence of crack bridging has proved to reduce mode III fracture too (Fig. 5.8).

Summarized, the presence of an organic phase as well as the abrupt change in crystallite orientations in the interrod region coupled with enamel's hierarchical structure are obviously advantageous for bridge formation at different length scales - several enamel rods (10-20 μm) (Tab. 5.1), one enamel rod (≈3 μm) (Fig. 5.6 (a)), groups of crystallite fibers around interrod regions (200-400 nm) (Fig. 5.6 (b)) and even one crystallite fiber (≈85 nm) (Fig. 5.6 (c)). Such ability of a material to form bridges from ≈20 μm down to ≈85 nm has neither been observed before in enamel nor in commercial ceramic materials.

Small droplets adjacent to the the crack in enamel are observed and are believed to be the result from the loosenings of the interrod spaces due to microcracks (the specimens were hydrated by using cotton swabs saturated with HBSS salt solution) [149]. In our study, we observed microcracks of the length scale of one to two enamel rods (≈6 μm) (Fig. 5.7 (a)) and multiple crystallites (100-500 nm) which occurred in the enamel rod region) (Fig. 5.7 (b)). Loosening of the crystallites structure (Fig. 5.7 (c)) along the crack path is also a trace of the presence of microcracks. One may argue that the observed microcracks under SEM (Fig. 5.7 (a) and (b)) are artifact crackings due to the SEM sample preparation procedures (for example, dehydration effect in a vacuum chamber). However, they were also observed under AFM investigation in ambient conditions.

The wide range of calculated K_{I0} values is hypothesized to be caused by different morphological surroundings at the crack tip. The cohesive zone could occur in at least 3 surroundings in the interrod/rod region: 'longitudinal orientation', 'transverse orientation' and 'mixed orientation' as illustrated in Fig. 5.9. Note that both 'longitudinal'

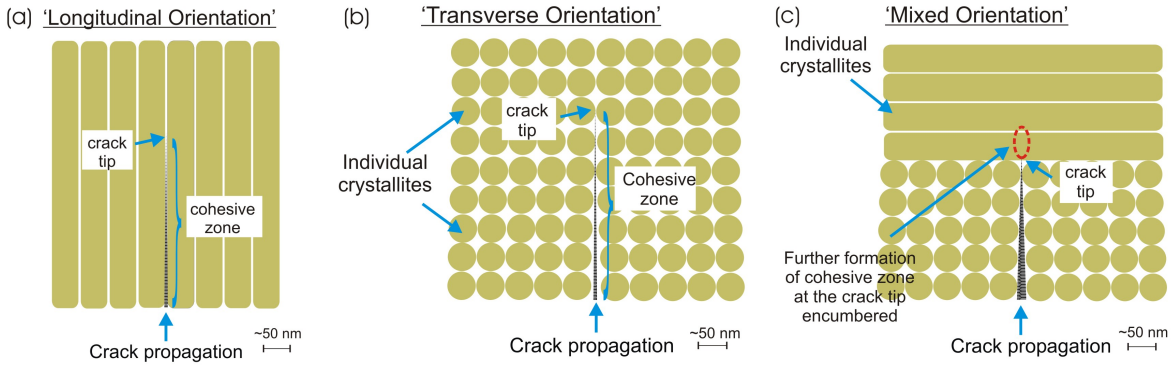

Figure 5.9.: (a)-(c) The hypotheses of 3 possible morphological surroundings at the crack tip.

or 'transverse' orientations could happen for both modes 'along' (mainly along interrod regions) and 'across' (mainly across enamel rod regions) crack propagation. The cohesive zone is expected to be different in three situations. In the case of 'longitudinal orientation' and 'transverse orientation', a cohesive zone is formed relatively easily in comparison to a 'mixed orientation', where the crack tip reaches a boundary with an abrupt change in crystallite orientations. The K_{I0} measured from both 'longitudinal orientation' and 'transverse orientation' is expected to be lower in comparison to 'mixed orientation'. For a longer cohesive zone (up to 10 µm), the situation in the cohesive zone would be a combination of the mentioned surroundings above. The limitation of this study is that the crack tip toughness could not be correlated to the crystallite orientation and in-situ crack propagation could not be observed. A potential method for such observation is utilizing in-situ etching procedures to reveal the crystallite orientations.

Fig. 5.10 illustrates toughening mechanisms in enamel of zero level (single crystallite nanofiber), first level (multiple crystallite nanofibers but within one enamel rod or interrod region) and second level (multiple enamel rods) hierarchical structures. Fig. 5.10 (a) shows an 'across' crack together with the observed crack bridging at interrod regions (first level; multiple crystallite fibers), crack bridging within one enamel rod (zero level; one enamel crystallite fiber); microcracks that span across two enamel rods

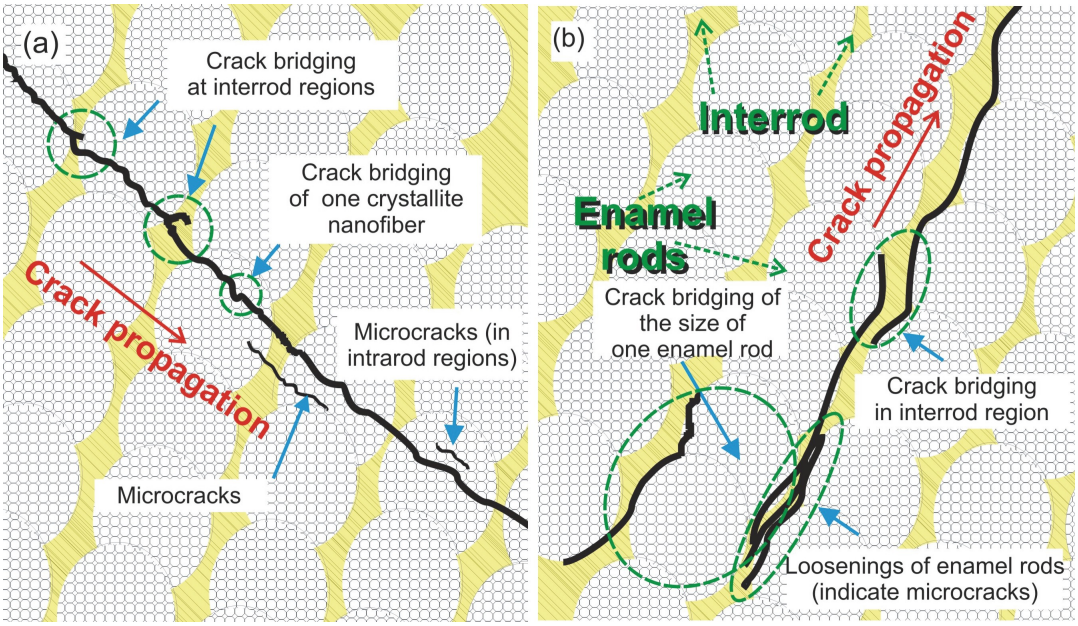

Figure 5.10.: Sub-10μm toughening in enamel observed for (a) an 'across' crack and (b) an 'along' crack.

(second level) and microcracks in enamel rod region (first level, multiple enamel crystallite fibers). Fig. 5.10 (b) shows an 'along' crack together with the observed crack bridging that involve one enamel rod (first level), crack bridging in interrod region (first level, multiple crystallite fibers), as well as loosenings of prism structures that indicated the presence of microcracks.

5.4. Conclusions

Irwin's 'near-field' solution is used to calculate the mode I and III crack tip toughness of enamel, $K_{\mathrm{I0,Ir}}$ as 0.5-1.6 MPa$\sqrt{m}$. The mode III crack tip toughness (0.02-0.15 MPa$\sqrt{m}$) is comparatively negligible. Besides, the cohesive zone model of a Dugdale-Muskhelishvili crack is used to calculate the closure stress near the crack tip, $\overline{\sigma_{\mathrm{br}}}$ as 163-770 MPa, with a cohesive zone size of 1.6-10.1 μm long and 24-44 nm wide, which might be attributed to the microcracks, the bridging of protein and apatite ligaments.

These parameters of the cohesive zone are used to calculate $K_{\mathrm{I0,cz}}$=0.8-1.5 MPa$\sqrt{m}$. Interrod regions reinforce enamel by bridge formation along interrod regions but also hinder crack propagation by a significant change in crystallite orientation compared to those in the enamel rod region. Crack bridges and microcracks were identified to occur across different length scales: the bridge sizes are from ≈85 nm to ≈3 μm and the microcracks are from 100-500 nm to ≈6 μm respectively in this study.

6. Conclusions

Enamel's elastic/inelastic transitions decreases from 17 GPa to 0.4 GPa with increasing hierarchical levels. Similarly, its elastic moduli measures up to 115 GPa for a single nanometer-sized construction unit (single crystallite fiber) but only 30 GPa for bulk enamel. These trends are attributed to an increasing volume of weak phases around each crystallite fiber and rod with additional hierarchical levels as well as an increasing volume of nanometer and micrometer scaled defects.

At a first glance, an increasing number of hierarchical structures is disadvantageous. However, investigation of enamel's sub-10μm fracture behavior indicates the contrary. The presence of weak phases provide pathways to crack bridges and microcracks formation, both are crack closure mechanisms. The presence of hierarchical structure allows enamel to form crack bridges and microcracks at different length scale: the bridges are from ≈85 nm to ≈3 μm in width (and up to 20 μm in width in previous studies (Tab. 5.1)) and the microcracks are from 100-500 nm to ≈6 μm in length. Such ability to form toughening mechanisms across different length scales from tens of nanometers to tens of micrometers has never been observed in other man-made materials.

Enamel has a low crack tip toughness, determined in this study as K_{I0}=0.5-1.6 MPa$\sqrt{m}$. The parameters for the cohesive zone at the crack tip were also calculated. The mean crack-closure stress at the crack tip was computed as 163-770 MPa with a cohesive

zone length and width of 1.6-10.1 μm and 24-44 nm respectively. This means that the cohesive zone encompasses multiple crystallite fibers or even multiple enamel rods. 3 possible morphological surroundings at the crack tip are presented as a hypothesis to explain the scattering of K_{I0} values and the cohesive zone parameters depending on the orientation between the crack propagation direction and crystallite fiber arrangements.

The significantly different crystallite fiber orientations in interrod regions compared to the intrarod regions was identified to encumber crack propagation. Besides, when longer time is allowed for deformation, the magnitude of inelastic energy dissipation in the interrod region is statistically significantly higher than in the enamel rod region, possibly due to protein unfoldings in the organics-rich sheath. An estimation shows that up to 1.6 protein unfoldings/(nm^3 proteins $\cdot$ s) could happen under the single loading-unloading profile with P_{max}=500 μN used in this study.

Summarized, the presence of hierarchical structures in enamel reduce its elastic moduli and elastic/inelastic transition with increasing hierarchical level but the weak interrod and inter-crystallite phases which come along with the hierarchical structure are in fact highly beneficial in making enamel damage-tolerant.

Appendices

A. Calibration of the used compression equipment and the indenters

Appendix A.1 outlines the calibration of the compression equipment to remove the equipment deformation effect on the result curves in Chapter 3. The calibration curves to obtain the indenter radii of the 3 indenters used in Chapter 3 (R=8.3 μm, R=0.86 μm and R=63 nm) and the R≈1 μm long shaft indenter used in Chapter 4 are presented in Section A.2.

A.1. Calibration of the compression equipment

The effect of the equipment deformation was measured in order to be subtracted from the specimen result curves. As explained in Chapter 3.1.2.1, an alumina specimen with ≈4-5 mm^2 in area was loaded up to 3 kN with a pressure of ≈150 MPa. By assuming that the alumina's compressibility is negligible at this pressure, the displacement-force response represents the equipment deformation under compression (Fig. A.1). The first loading curve is fitted and gives

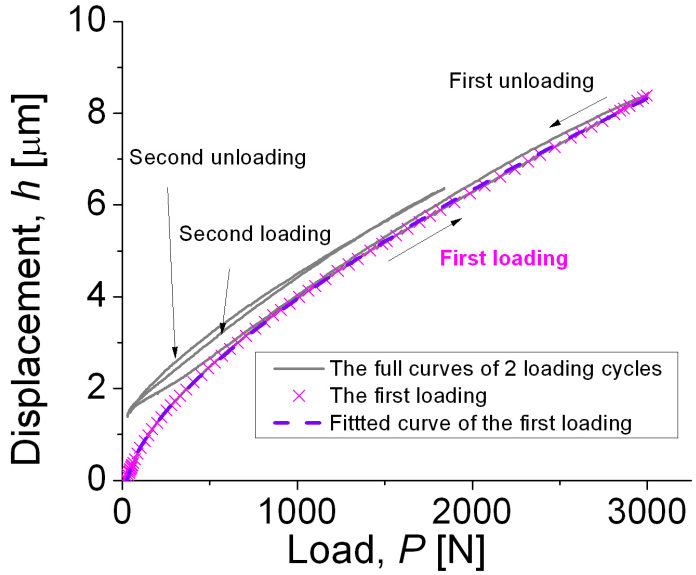

Figure A.1.: Displacement-force curve of the equipment deformation under compression. The compressibility of alumina is assumed to be negligible at the pressure of ≈150 MPa. The first loading curve is fitted as a $h = f(P)$ function (Eq. (A.1)) and is subtracted from the result curves with enamel specimen. The second loading cycle shows a hysteresis of <1 μm. The hysteresis below P=200 N is bigger but is not involved in the E calculation in Fig. 3.5 (a).

$$h = -3.097 + 0.636P^{1/2} - 5.017P^{1/3} + 6.652P^{1/4}. \tag{A.1}$$

This deformation effect was subtracted from the result curves with enamel specimen before it is presented it Fig. 3.5 (a).

A.2. Calibration of the indenter radii

The indenter radii of the 3 indenters used in Chapter 3 (R=8.3 μm, R=0.86 μm and R=63 nm) and the long shaft indenter used in Chapter 4 (R≈1 μm, suitable to be used for nanoindentation in liquid) were calibrated on a fused quartz sample (Hysitron, USA) (E_r=69.6 GPa) with loading curves of P_{max} ranging from 0.1 to 11 mN. More than 45 curves were used to calibrate each indenter. To obtain the radius, the initial

parts of these loading curves were fitted with Eq. (2.2), which were appropriate to h_t<20 nm for the 8.3 μm indenter, 15<h_t<60 nm for the 0.86 μm indenter, h_t<10 nm for the 63 nm indenter and 6<h_t<60 nm for the R≈1 μm long shaft indenter. These ranges were chosen because they displayed linear behavior and the limit of elastic range for the materials under investigation occurs in this region. For deeper indentations, the spheroconical shape of the tip leads to the deviation from linearity, especially for Eq. (2.2).

The indenter radii were calibrated as R=8.3±0.9 μm, R=0.86±0.03 μm and R=63±11 nm respectively for the 3 indenters used in Chapter 3 and is R=0.88±0.2 μm for the long shaft indenter used in Chapter 4.

A question might arise whether the deviation from linearity shown in Fig. A.2 is caused by the change of indenter radii or due to the inelastic deformation of the fused quartz. This verification is performed as the following. For the 8.3 μm indenter, with P=900 μN, h_t=20 nm, the contact pressure was $P/\pi a^2$=1.7 GPa, which is much lower than the indentation limit of elastic range of fused silica, observed as ≈9 GPa by using a R=1 μm, R=2.5 μm and R=7 μm spherical indenter [172]. Similarly, the contact pressure under the 0.86 μm at P=1400 μN, h_t=62 nm was ≈8.5 GPa, and for the 0.88 μm indenter at P=1400 μN, h_t=60 nm was ≈8.5 GPa too, which are also slightly smaller than the observed ≈9 GPa [172]. Therefore, the deviations of the measured data from the linear fit in Fig A.2 (a), (b) and (d) are interpreted as a change of the tip shape rather than inelastic deformation of fused silica. The contact pressure for the R=63 nm indenter at P=32 μN, h_t=11 nm is ≈15 GPa, higher than the typically observed limit of elastic range. The contact pressure under the same indenter at P=2 μN, h_t=1 nm is calculated as 10 GPa. The fused quartz sample was already deformed plastically under the indenter at such a small penetration depth. That is why the load-displacement curve shown as an inset in Fig. A.2 (c) has a hysteresis, and that the elastic response of Eq.

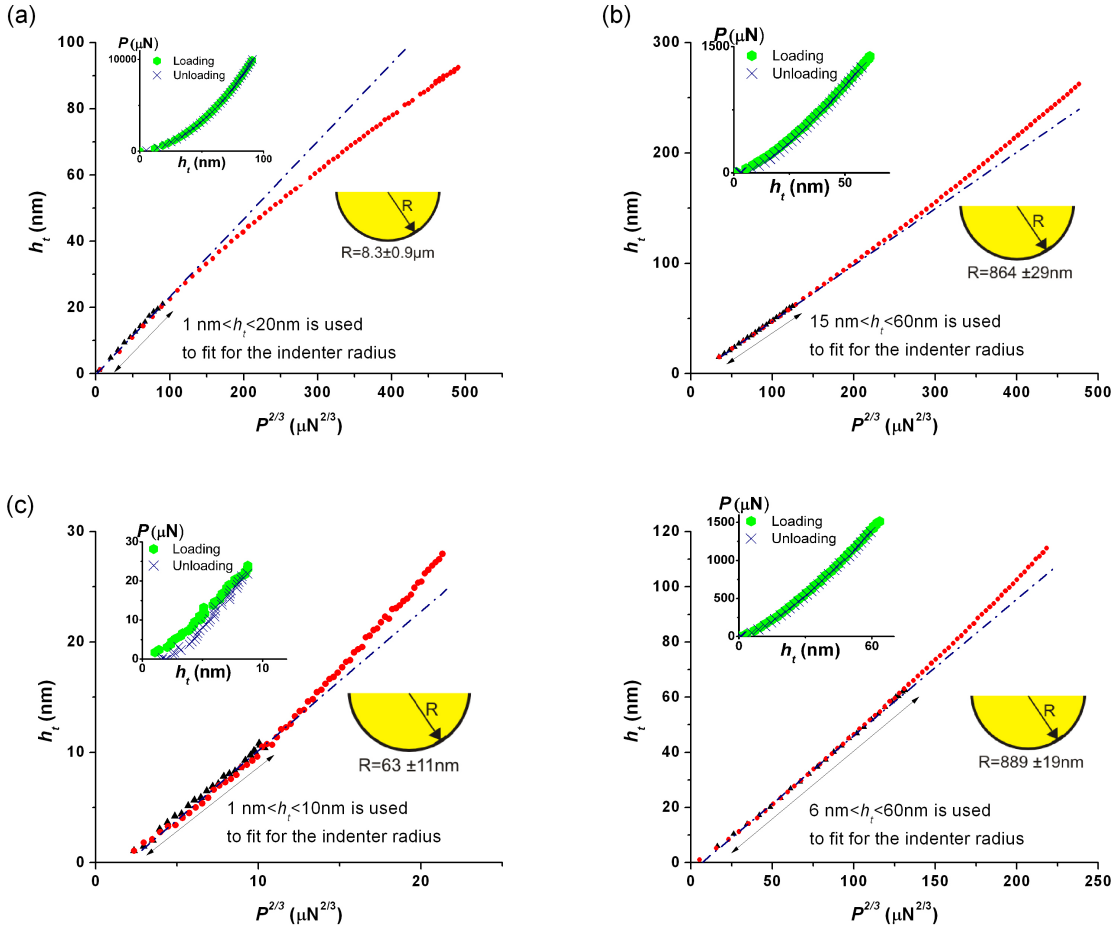

Figure A.2.: Indenter radii calibration on fused quartz. The range of h_t versus $P^{2/3}$ curves used for radii calibration for (a) R=8.3 μm indenter (h_t<20 nm), (b) R=0.86 μm indenter (15<h_t<60 nm), (c) R=63 nm indenter (h_t<10 nm), and (d) R≈1 μm long shaft indenter (6<h_t<60 nm), show linear behaviors. The indenters in (a)-(c) were used for the experiments in Chapter 3 whrereas the indenter in (d) was used for the study in Chapter 4. (Inset: The load-displacement curves that include the range of h_t used for radii calibration.)

(2.2) could no longer be assumed. Since the h_t versus $P^{2/3}$ curve in Fig. A.2 (c) displays reasonably linear behavior in the calibrated region, the calibrated 63±11 nm is believed not to be affected by the inelastic deformation of fused quartz.

The data of h_t<1 nm usually are associated with big fluctuations (noise) and are discarded from the analysis.

B. Load-displacement curves of enamel and synthetic HAP in Chapter 3

The load-displacement curves (raw data of nanoindentation experiments) used in Chapter 3 are presented.

B.1. Load-displacement curves of enamel

The enamel's P-h_t curves from which the data are extracted to plot P_m versus a/R curves in Fig. 3.5 are shown in Fig. B.1

B.2. Load-displacement curves of synthetic HAP

The synthetic HAP's P-h_t curves from which the data are extracted to plot P_m versus a/R curves in Fig. 3.6 are shown in Fig. B.2

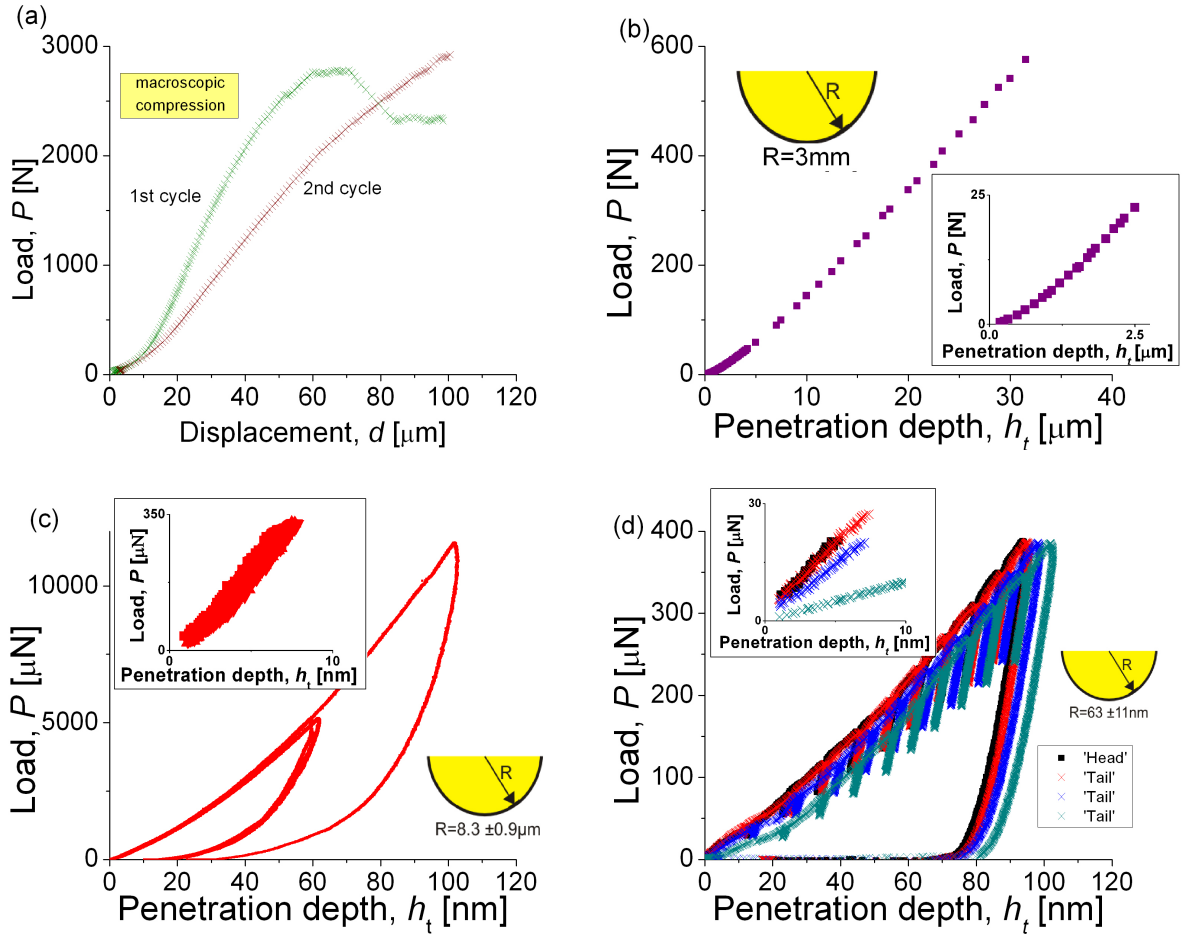

Figure B.1.: Enamel's load-displacement curves of (a) uni-axial compression tests, (b) R=3 mm indenter [118], (c) R=8.3 μm indenter and (d) R=63 nm indenter from which the data are extracted to plot the P_m versus a/R curves in Fig. 3.5. For indentation tests, the insets show the enlarged versions of the elastic portion up to the elastic/inelastic transition.

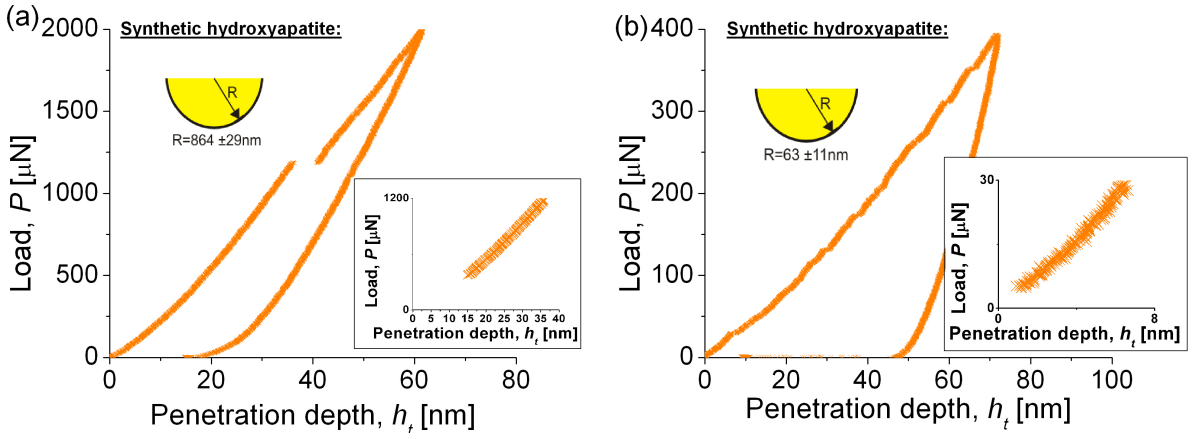

Figure B.2.: Synthetic HAP's load-displacement curves of (a) R=0.86 μm indenter and (b) R=63 nm indenter from which the data are extracted to plot the P_m versus a/R curves in Fig. 3.6. The insets show the enlarged versions of the elastic portion up to the elastic/inelastic transition.

C. Measured u_I versus X

The data of mode I half crack opening (u_I) versus crack length behind the crack tip (X) of each crack (to calculate K_{I0} in Chapter 5.1.2) are listed in Tab. C.1.

Table C.1.: u_I versus X of all cracks, used to calculate $K_{I0,Ir}$ in Chapter 5.1.2.

Crack 'along'-1		**Crack 'along'-2**		**Crack 'across'-1**		**Crack 'across'-2**	
X [µm]	u_I [nm]	X [µm]	u_I [nm]	X [µm]	u_I [nm]	X [µm]	u_I [nm]
0.07	22.5	0.07	19.0	0.07	22.0	0.07	18.0
0.10	24.5	0.14	22.0	0.14	21.5	0.13	19.5
0.14	24.0	0.4	23.5	0.4	23.0	0.27	20.5
0.2	24.0	0.7	24.0	0.8	27.0	0.33	23.0
0.7	25.0	0.9	28.0	2.0	32.5	0.4	27.5
1.1	24.0	1.3	34.0	3.1	35.5	1.0	31.5
1.4	26.5	1.4	36.5	3.9	35.5	1.6	31.5
2.8	32.5	1.7	40.5	5.0	35.5	2.1	35.0
3.0	35.5	2.5	37.5	8.8	43.5	3.5	34.5
3.5	34.5	2.9	42.0	10.0	48.0	4.2	40.5
4.3	38.0	3.4	42.0			4.9	39.0
5.7	52.0					5.6	40.0
6.5	49.5					6.3	42.0
7.2	51.0					8.5	41.0
10.3	44.5						

Table C.1(*continued*): u_I versus X of all cracks, used to calculate $K_{I0,Ir}$ in Chapter 5.1.2.

Crack 'across'-3		**Crack 'across'-4**	
X [µm]	u_I [nm]	X [µm]	u_I [nm]
0.07	17.0	0.07	14.0
0.1	16.5	0.10	14.5
0.14	18.5	0.14	16.5
0.4	20.5	0.3	16.0
0.9	20.5	0.5	20.5
1.1	25.0	0.7	23.0
1.3	27.5	1.1	24.0
1.7	35.5	1.3	23.5
2.5	45.5	1.7	27.5
3.4	46.0	1.8	32.0
3.9	52.5	1.9	52.5
4.4	59.0	2.4	47.0
4.8	59.0	2.9	49.0
5.2	46.0	3.5	52.5
5.5	47.5	3.9	54.0
5.9	59.0	4.2	59.0
6.6	52.5	4.5	56.5
7.0	60.0		

The data of mode III half crack opening (u_{III}) versus crack length behind the crack tip (X) of each crack (to calculate K_{III0} in Chapter 5.1.2) are not listed here since the calculated K_{III0} values are small and negligible.

Bibliography

[1] L H He and M V Swain. Understanding the mechanical behaviour of human enamel from its structural and compositional characteristics. *J Mech Behav Biomed Mater*, 1(1):18–29, Jan 2008.

[2] M Baldassarri, H C Margolis, and E Beniash. Compositional determinants of mechanical properties of enamel. *J Dent Res*, 87(7):645–9, Jul 2008.

[3] G A Gogotsi. Fracture toughness of ceramics and ceramic composites. *Ceram Int*, 29(7):777–84, 2003.

[4] K E Healy. *Dentin and enamel.* Handbook of biomaterials properties. Chapman and Hall, London, 1998.

[5] M A Meyers, P-Y Chen, A Y-M Lin, and Y Seki. Biological materials: Structure and mechanical properties. *Prog Mater Sci*, 53(1):1 – 206, 2008.

[6] V Imbeni, J J Kruzic, G W Marshall, S J Marshall, and R O Ritchie. The dentin-enamel junction and the fracture of human teeth. *Nat Mater*, 4(3):229–32, 2005.

[7] S F Ang, A Schulz, R Pacher Fernandes, and G A Schneider. Sub-10-micrometer toughening and crack tip toughness of dental enamel. *J Mech Behav Biomed Mater*, 4:423–32, 2011.

[8] S Bechtle, S Habelitz, A Klocke, T Fett, and G A A Schneider. The fracture behaviour of dental enamel. *Biomaterials*, 31(2):375–84, 2010.

[9] D Bajaj and D D Arola. On the R-curve behavior of human tooth enamel. *Biomaterials*, 30(23-24):4037–46, 2009.

[10] S N White, W Luo, M L Paine, H Fong, M Sarikaya, and M L Snead. Biological organization of hydroxyapatite crystallites into a fibrous continuum toughens and controls anisotropy in human enamel. *J Dent Res*, 80(1):321–6, 2001.

[11] B Ji and H Gao. Mechanical properties of nanostructure of biological materials. *J Mech Phys Solids*, 52(9):1963–90, 2004.

[12] P K Hansma, G E Fantner, J H Kindt, P J Thurner, G Schitter, P J Turner, S F Udwin, and M M Finch. Sacrificial bonds in the interfibrillar matrix of bone. *J Musculoskelet Neuronal Interact*, 5(4):313–5, 2005.

[13] G E Fantner, T Hassenkam, J H Kindt, J C Weaver, H Birkedal, L Pechenik, J A Cutroni, G A G Cidade, G D Stucky, D E Morse, and P K Hansma. Sacrificial bonds and hidden length dissipate energy as mineralized fibrils separate during bone fracture. *Nat Mater*, 4(8):612–6, 2005.

[14] A Nanci. *Ten Cate's Oral Histology: Development, Structure, and Function.* Mosby, Missouri, 7th edition, 2007.

[15] H J Gao. Application of fracture mechanics concepts to hierarchical biomechanics of bone and bone-like materials. *Int J Fracture*, 138(1-4):101–37, 2006.

[16] S Bechtle, S F Ang, and G A Schneider. On the mechanical properties of hierarchically structured biological materials. *Biomaterials*, 31(25):6378–85, 2010.

[17] H Gray, L H Bannister, M M Berry, and P L Williams. *Gray's Anatomy: The Anatomical Basis of Medicine and Surgery.* Churchill Livingstone, 38th edition, 1995.

[18] P D Frazier. Adult human enamel: an electron microscopic study of crystallite size and morphology. *J Ultrastruct Res*, 22(1):1–11, 1968.

[19] G Daculsi and B Kerebel. High-resolution electron microscope study of human enamel crystallites: size, shape, and growth. *J Ultrastruct Res*, 65(2):163–72, 1978.

[20] H J Orams, J J Zybert, P P Phakey, and W A Rachinger. Ultrastructural study of human dental enamel using selected-area argon-ion-beam thinning. *Arch Oral Biol*, 21(11):663–75, 1976.

[21] A H Meckel, W J Griebstein, and R J Neal. Structure of mature human dental enamel as observed by electron microscopy. *Arch Oral Biol*, 10(5):775–83, 1965.

[22] J Erausquin. The aspect of the bands of schreger in the horizontal sections of the enamel. *J Dent Res*, 28(2):195–200, 1949.

[23] J W Osborn. Directions and interrelationships of enamel prisms from the sides of human teeth. *J Dent Res*, 47(2):223–32, 1968.

[24] Z Skobe and S Stern. The pathway of enamel rods at the base of cusps of human teeth. *J Dent Res*, 59(6):1026–32, 1980.

[25] G Daculsi, J Menanteau, L M Kerebel, and D Mitre. Length and shape of enamel crystals. *Calcif Tissue Int*, 36(5):550–5, 1984.

[26] T G Bromage and M C Dean. Re-evaluation of the age at death of immature fossil hominids. *Nature*, 317(6037):525–7, 1985.

[27] S Hoffman, W S McEwan, and C M Drew. Scanning electron microscope studies of dental enamel. *J Dent Res*, 48(2):242–50, 1969.

[28] F C M Driessens and R M H Verbeeck. *Biominerals.* CRC Press, Florida, 2000.

[29] J H Bowes and M M Murray. The chemical composition of teeth: The composition of human enamel and dentine. *Biochem J*, 29(12):2721–7, 1935.

[30] J H Bowes and M M Murray. The chemical composition of teeth: The variations in chemical composition in relation to dental structure. *Biochem J*, 30(6):977–84, 1936.

[31] M J Bird, E Kelman, H Lerner, D Rosenfeld, V Totah, and H C Hodge. Chemical analysis of teeth showing unusual wear. *J Dent Res*, 27:629–34, 1948.

[32] M J Bird, H Gallup, J Gaudino, and H C Hodge. A comparison of two methods of ashing enamel and dentin. *J Dent Res*, 27:693–704, 1948.

[33] F J McClure. Fluorine in dentin and enamel of sound and carios human teeth. *J Dent Res*, 27:287–98, 1948.

[34] B Angmar, D Carlstrom, and J E Glas. Studies on the ultrastructure of dental enamel. IV. the mineralization of normal human enamel. *J Ultrastruct Res*, 8:12–23, 1963.

[35] M F Little, E S Cueto, and J Rowley. Chemical and physical properties of altered and sound enamel-I: Ash, Ca, P, CO_2, N, water, microradiolucency and density. *Arch Oral Biol*, 7(2):173 – 184,, 1962.

[36] M L Lefevre and Manly R S. Moisture, inorganic and organic contents of enamel and dentin from carious teeth. *J Am Dent Assoc*, 25(1938):233–42, 1938.

[37] R Z LeGeros, L M Silverstone, G Daculsi, and L M Kerebel. In vitro caries-like lesion formation in F^- containing tooth enamel. *J Dent Res*, 62:138–44, 1983.

[38] J Holager. Thermogravimetric experiments on tooth carbonates. *J Dent Res*, 51:102–6, 1972.

[39] M F Little. Studies on the inorganic carbon dioxide component of human enamel. II. the effect of acid on enamel co2. *J Dent Res*, 40:903–14, 1961.

[40] M F Little and F S Casciani. The nature of water in sound human enamel. a preliminary study. *Arch Oral Biol*, 11(6):565–71, 1966.

[41] W D Armstrong and P J Brekhus. Chemical constitution of enamel and dentin. I. principal components. *J Biol Che*, 120:677–87, 1937.

[42] S M Weidmann and D R Eyre. Amino acid composition of enamel protein in the fully developed human tooth. *Caries Res*, 1(4):349–55, 1967.

[43] R Naujoks, H Schade, and F Zelinka. Chemical composition of different areas of the enamel of deciduous and permanent teeth. (The content of Ca, P, CO_2, Na and N_2). *Caries Res*, 1(2):137–43, 1967.

[44] J E Eastoe. Organic matrix of tooth enamel. *Nature*, 187:411–2, 1960.

[45] A Savory and F Brudevold. The distribution of nitrogen in human enamel. *J Dent Res*, 38(3):436–42, 1959.

[46] F L Losee and Hess W C. The chemical nature of proteins from human enamel. *J Dent Res*, 28(5):512–7, 1949.

[47] D J Anderson. Nitrogen in human dental enamel. *Biochem J*, 45(1):31–2, 1949.

[48] R Z LeGeros, G Bonel, and R Legros. Types of "H_2O" in human enamel and in precipitated apatites. *Calcif Tissue Res*, 26(2):111–8, 1978.

[49] G T Vatassery, W D Armstrong, and L Singer. Determination of hydroxyl content of calcified tissue mineral. *Calcif Tissue Res*, 5(3):183–8, 1970.

[50] T Ockerse. The chemical composition of enamel and dentin in high and low caries area in south africa. *J Dent Res*, 22(6):441–6, 1943.

[51] A K Bose, R Q Blackwell, and L S Fosdick. The fractionation of human tooth enamel on the basis of density. *J Dent Res*, 39(1):141–9, 1960.

[52] H G McCann and F A Bullock. Reactions of fluoride ions with powdered enamel and dentin. *J Dent Res*, 34(1):59–67, 1955.

[53] E L Lakomaa and I Rytömaa. Mineral composition of enamel and dentin of primary and permanent teeth in finland. *Scand J Dent Res*, 85(2):89–95, 1977.

[54] M Ahlberg and R Akselsson. Proton-induced X-ray emission in the trace analysis of human tooth enamel and dentine. *Int J Appl Radiat Isot*, 27(5-6):279–90, 1976.

[55] R Soeremark and K Samsahl. Gamma-ray spectrometric analysis of elements in normal human enamel. *Arch Oral Biol*, 6 (Suppl.):275–83, 1961.

[56] R Lappalainen, M Knuuttila, and R Salminen. The concentrations of Zn and Mg in human enamel and dentine related to age and their concentrations in the soil. *Arch Oral Biol*, 26(1):1 – 6, 1981.

[57] J Haataja, P Pohto, E Kleemola-Kujala, and L Hansson. On the macrominerals of deciduous teeth. *Proc Finn Dent Soc*, 68(2):67–72, 1972.

[58] D H Retief, P E Cleaton-Jones, J Turkstra, and W J De Wet. The quantitative analysis of Sr, Au, Br, Mn and Na in normal human enamel and dentine by neutron activation and high resolution gamma-spectrometry. *J Dent Assoc S A*, 26:63–9, 1971.

[59] N L Derise, S L Ritchey, and A K Furr. Mineral composition of normal human enamel and dentin and the relaton of composition to dental caries. i. macrominerals and comparison of methods of analyses. *J Dent Res*, 53(4):847–52, 1974.

[60] P R Patel and W E Brown. Thermodynamic solubility product of human tooth enamel: powdered sample. *J Dent Res*, 54(4):728–36, 1975.

[61] F L Losee, T W Cutress, and R Brown. Natural elements of the periodic table in human dental enamel. *Caries Res*, 8(2):123–34, 1974.

[62] M Anwar Chaudhri and T Ainsworth. Applications of PIXE to studies in dental and mental healths. *Nucl Instrum Methods*, 181(1-3):333–6, 1981.

[63] M Anwar Chaudhri and A Crawford. The influence of trace elements of fluoride uptake by teeth. *Nucl Instrum Methods*, 181(1-3):327–31, 1981.

[64] G Cho, Y Wu, and J L Ackerman. Detection of hydroxyl ions in bone mineral by solid-state nmr spectroscopy. *Science*, 300(5622):1123–7, 2003.

[65] J D Pasteris, B Wopenka, J J Freeman, K Rogers, E Valsami-Jones, J A M van der Houwen, and M J Silva. Lack of oh in nanocrystalline apatite as a function of degree of atomic order: implications for bone and biomaterials. *Biomaterials*, 25(2):229–38, 2004.

[66] T Yanagisawa and Y Miake. High-resolution electron microscopy of enamel-crystal demineralization and remineralization in carious lesions. *J Electron Microsc (Tokyo)*, 52(6):605–13, 2003.

[67] T Leventouri. Synthetic and biological hydroxyapatites: crystal structure questions. *Biomaterials*, 27(18):3339–42, 2006.

[68] A A Odutuga and R E Prout. Effect of essential fatty acid deficiency on the fatty acid composition of individual lipids from enamel and dentine of the rat. *Arch Oral Biol*, 19(10):911–20, 1974.

[69] J E Eastoe. Enamel protein chemistry–past, present and future. *J Dent Res*, 58(Spec Issue B):753–64, 1979.

[70] W C Hess, C Y Lee, and B A Neidig. The amino acid composition of enamel protein. *J Dent Res*, 32(4):585–7, 1953.

[71] G C Battistone and G W Burnett. Studies of the composition of teeth: IV. the amoni acid composition of human enamel protein. *J Dent Res*, 35(2):260–2, 1956.

[72] A Belcourt and S Gillmeth. Edta soluble protein of human mature normal enamel. *Calcif Tissue Int*, 28(3):227–31, 1979.

[73] J P Klein, M Schöller, and R M Frank. Soluble and insoluble proteins of normal human mature enamel. *Arch Oral Biol*, 27(2):133–9, 1982.

[74] Y Açil, A E Mobasseri, P H Warnke, H Terheyden, J Wiltfang, and I Springer. Detection of mature collagen in human dental enamel. *Calcif Tissue Int*, 76(2):121–6, 2005.

[75] D Carlstrom, J E Glas, and B Aangmar. Studies on the ultrastructure of dental enamel. V. the state of water in human enamel. *J Ultrastruct Res*, 8:24–9, 1963.

[76] C L Davidson and J Arends. Thermal analysis studies on sound and artificially decalcified tooth enamel. *Caries Res*, 11(6):313–20, 1977.

[77] D W Holcomb and R A Young. Thermal decomposition of human tooth enamel. *Calcif Tissue Int*, 31(3):189–201, 1980.

[78] J T Corcia and W E Moody. Thermal analysis of human dental enamel. *J Dent Res*, 53(3):571–80, 1974.

[79] J Holager. Thermogravimetric examination of enamel and dentin. *J Dent Res*, 49(3):546–8, 1970.

[80] S Ferguson and D B Chesnut. A magnetic resonance spin label study of human dental enamel. *Arch Oral Biol*, 23(2):85 – 90, 1978.

[81] G H Dibdin. The stability of water in human dental enamel studied by proton nuclear magnetic resonance. *Arch Oral Biol*, 17(3):433–37, 1972.

[82] E C Moreno and R T Zahradnik. The pore structure of human dental enamel. *Arch Oral Biol*, 18(8):1063–8, Aug 1973.

[83] G W Burnett and J Zenewitz. Studies of the composition of teeth. VII. the moisture content of calcified tooth tissues. *J Dent Res*, 37(4):581–9, 1958.

[84] G M Brauer, D J Termini, and C L Burns. Characterization of components of dental materials and components of tooth structure by differential thermal analysis. *J Dent Res*, 49(1):100–10, 1970.

[85] R A Young, M L Barlett, S Spooner, P E Mackie, and G Bonel. Reversible high temperature exchange of carbonate and hydroxl ions in tooth enamel and synthetic hydroxyapatite. *J Biol Phys*, 9(1):1–26, 1981.

[86] Y Nishimura, Y Tsubota, and S Fukushima. Influence of cyclic loading on fiber post and composite resin core. *Dent Mater J*, 27(3):356–61, 2008.

[87] N D Ruse, D C Smith, C D Torneck, and K C Titley. Preliminary surface analysis of etched, bleached, and normal bovine enamel. *J Dent Res*, 69(9):1610–3, 1990.

[88] R P Sanches, C Otani, A J Damiao, and W Miyakawa. AFM characterization of bovine enamel and dentine after acid-etching. *Micron*, 40(4):502–6, 2009.

[89] M J Glimcher, E J Daniel, D F Travis, and S Kamhi. Electron optical and X-ray diffraction studies of the organization of the inorganic crystals in embryonic bovine enamel. *J Ultrastruct Res*, 50:Suppl 7:1–77, 1965.

[90] A C Fischer-Cripps. *Nanoindentation (Mechanical Engineering Series)*. Springer, New York, 3rd edition, 2011.

[91] H R Hertz. *Miscellaneous papers*. Macmillan, London, 1896.

[92] W C Oliver and G M Pharr. An improved technique for determining hardness and elastic modulus using load and displacement sensing indentation experiments. *J Mater Res*, 7(6):1564–83, 1992.

[93] J S Field and M V Swain. A simple predictive model for spherical indentation. *J Mater Res*, 8(2):297–306, 1993.

[94] K L Johnson. *Contact mechanics*. Cambridge University Press, Cambridge, 1985.

[95] D Tabor. *The hardness of metals*. Clarendon Press, Oxford, 1951.

[96] L H He and M V Swain. Energy absorption characterization of human enamel using nanoindentation. *J Biomed Mater Res*, 81A:484–92, 2006.

[97] E H Lee and J R M Radok. The contact problem for viscoelastic solids. *Trans. ASME, Ser E, J Appl Mech*, pages 438–44, 1960.

[98] M L Oyen. Spherical indentation creep following ramp loading. *J Mater Res*, 20(8):2094–100, 2005.

[99] J Mencik, L H He, and M V Swain. Determination of viscoelastic-plastic material parameters of biomaterials by instrumented indentation. *J Mech Behav Biomed Mater*, 2:318–25, 2009.

[100] L H He and M V Swain. Nanoindentation creep behavior of human enamel. *J Biomed Mater Res A*, 91A(2):352–9, 2008.

[101] G Williams and D C Watts. Non-symmetrical dielectric relaxation behaviour arising from a simple empirical decay function. *Trans Faraday Soc*, 66:80–5, 1970.

[102] M Berberan-Santos, E N Bodunov, and B Valeur. History of the kohlrausch (stretched exponential) function: Focus on uncited pioneering work in luminescence. *Annalen der Physik*, 17(7):460–461, 2008.

[103] K L Dorrington. The theory of viscoelasticity in biomaterials. *Symp Soc Exp Biol*, 34:289–314, 1980.

[104] A A Griffith. The phenomena of rupture and flow in solids. *Philos Trans R Soc London, Ser A*, 221:163–198, 1921.

[105] F Erdogan. Fracture mechanics. *Int J Solids Struct*, 37:171–183, 2000.

[106] G R Irwin. Fracture dynamics. *In: Fracturing of Metals. Amer Soc For Metals*, pages 147–166, 1948.

[107] E Orowan. Fracture and strength of solids. *Reports on Progress in Physics XII*, pages 185–232, 1948.

[108] G R Irwin. Analysis of stresses and strains near the end of a crack traversing a plate. *ASME J Appl Mech*, 24:361–364, 1957.

[109] G R Irwin. *Fracture, in Handbuch der Physik*, volume 6. Springer-Verlag, Berlin, 1958.

[110] B Lawn. *Fracture of brittle solids*. Cambridge University Press, Cambridge, 2nd edition, 1993.

[111] T Fett. *Stress Intensity Factors, T-Stresses, Weight Functions. Supplement Volume*. KIT Scientific Publishing, Karlsruhe, 2009.

[112] G I Barenblatt. The mathematical theory of equilibrium cracks in brittle fracture. *Advan Appl Mech*, 7:55–129, 1962.

[113] H Warshawsky, K Josephsen, A Thylstrup, and O Fejerskov. The development of enamel structure in rat incisors as compared to the teeth of monkey and man. *Anat Rec*, 200(4):371–99, Aug 1981.

[114] L J Oesterle, W C Shellhart, and G K Belanger. The use of bovine enamel in bonding studies. *Am J Orthod Dentofacial Orthop*, 114(5):514–9, 1998.

[115] S Habelitz, G W Marshall, M Balooch, and S J Marshall. Nanoindentation and storage of teeth. *J Biomech*, 35(7):995–8, 2002.

[116] H Jelitto, F Felten, M V Swain, and H Balke. Measurement of the total energy release rate for cracks in PZT under combined mechanical and electrical loading. *J Appl Mech*, 74(6):1197–211, 2007.

[117] T Scholz, K K McLaughlin, F Giuliani, W J Clegg, F J Espinoza-Beltran, M V Swain, and G A Schneider. Nanoindentation initiated dislocations in barium titanate ($BaTio_3$). *Appl Phys Lett*, 91(6):062903, 2007.

[118] M Staines, W Robinson, and J A A A Hood. Spherical indentation of tooth enamel. *J Mater Res*, 16:2551–6, 1981.

[119] L H He and M V Swain. Enamel - a "metallic-like" deformable biocomposite. *J Dent*, 35(5):431–7, 2007.

[120] W D Nix and H Gao. Indentation size effects in crystalline materials: A law for strain gradient plasticity. *J Mech Phys Solids*, 46(3):411–25, 1998.

[121] J G Swadener, E P George, and G M Pharr. The correlation of the indentation size effect measured with indenters of various shapes. *J Mech Phys Solids*, 50(4):681–94, 2002.

[122] B Viswanath, R Raghavan, U Ramamurty, and N Ravishankar. Mechanical properties and anisotropy in hydroxyapatite single crystals. *Scr Mater*, 57(4):361–4, 2007.

[123] Z-H Xie, M V Swain, G Swadener, P Munroe, and M Hoffman. Effect of microstructure upon elastic behaviour of human tooth enamel. *J Biomech*, 42(8):1075–80, 2009.

[124] J Zhou and L L Hsiung. Biomolecular origin of the rate-dependent deformation of prismatic enamel. *J Biomech*, 89:051904, 2009.

[125] K Tai, M Dao, S Suresh, A Palazoglu, and C Ortiz. Nanoscale heterogeneity promotes energy dissipation in bone. *Nat Mater*, 6(6):454–62, 2007.

[126] L H He and M V Swain. Contact induced deformation of enamel. *Appl Phys Lett*, 90:171916, 2007.

[127] S F Ang, T Scholz, A Klocke, and G A Schneider. Determination of the elastic/plastic transition of human enamel by nanoindentation. *Dent Mater*, 25(11):1403–10, 2009.

[128] M J Buehler and S Y Wong. Entropic elasticity controls nanomechanics of single tropocollagen molecules. *Biophys J*, 93(1):37–43, 2007.

[129] L U Bigliani, R G Pollock, L J Soslowsky, E L Flatow, R J Pawluk, and V C Mow. Tensile properties of the inferior glenohumeral ligament. *J Orthop Res*, 10(2):187–97, 1992.

[130] M Druhala and M Feughelman. Dynamic mechanical loss in keratin in low temperatures. *Colloid Polym Sci*, 252(5):381–91, 1974.

[131] Z Xie, M V Swain, and M J Hoffman. Structural integrity of enamel: experimental and modeling. *J Dent Res*, 88(6):529–33, 2009.

[132] G A Schneider, L H He, and M V Swain. Viscous flow model of creep in enamel. *J Appl Phys*, 103:014701, 2008.

[133] G M Guidoni, L H He, T Schoeberl, I Jaeger, G Dehm, and M V Swain. Influence of the indenter tip geometry and environment on the indentation modulus of enamel. *J Mater Res*, 24:616–25, 2009.

[134] C Tromas, J Colin, C Coupeau, J C Girard, J Woirgard, and J Grilhe. Pop-in phenomenon during nanoindentation in mgo. *Eur Phys J: Appl Phys*, 8(2):123–8, 1999.

[135] J S Field, M V Swain, and R D Dukino. Determination of fracture toughness from the extra determination of fracture toughness from the extra penetration produced by indentation-induced pop-in. *J Mater Res*, 18(6):1412–1419, 2003.

[136] D R Carter and W C Hayes. The compressive behavior of bone as a two-phase porous structure. *J Bone Joint Surg Am*, 59(7):954–62, 1977.

[137] C R Carlisle, C Coulais, and M Guthold. The mechanical stress-strain properties of single electrospun collagen type I nanofibers. *Acta Biomater*, 6(8):2997 – 3003, 2010.

[138] S Habelitz, S J Marshall, G W Marshall, and M Balooch. Mechanical properties of human dental enamel on the nanometre scale. *Arch Oral Biol*, 46(2):173–83, 2001.

[139] J Ge, F Z Cui, X M Wang, and H L Feng. Property variations in the prism and the organic sheath within enamel by nanoindentation. *Biomaterials*, 26(16):3333–9, 2005.

[140] B J Briscoe, L Flori, and E Pelillo. Nano-indentation of polymeric surfaces. *J Phys D: Appl Phys*, 31(19):2395–405, 1998.

[141] B Tang and A H W Ngan. Accurate measurement of tip-sample contact size during nanoindentation of viscoelastic materials. *J Mater Res*, 18(5):1141–8, 2003.

[142] S F Ang, E L Bortel, M V Swain, A Klocke, and G A Schneider. Size-dependent elastic/inelastic behavior of enamel over millimeter and nanometer length scales. *Biomaterials*, 31(7):1955–63, 2010.

[143] L Dougan, A S R Koti, G Genchev, H Lu, and J M Fernandez. A single-molecule perspective on the role of solvent hydrogen bonds in protein folding and chemical reactions. *Chemphyschem*, 9(18):2836–47, 2008.

[144] J Zhang, M M Michalenko, E Kuhl, and T C Ovaert. Characterization of indentation response and stiffness reduction of bone using a continuum damage model. *J Mech Behav Biomed Mater*, 3(2):189–202, 2010.

[145] L H He and M V Swain. Influence of environment on the mechanical behaviour of mature human enamel. *Biomaterials*, 28(30):4512–20, 2007.

[146] C F Bodecker. Enamel lamellae and their origin. *J Dent Res*, 32(2):239–45, 1953.

[147] H Chai, J J W Lee, P J Conatantino, P W Lucas, and B R Lawn. Remarkable resilience of teeth. *PNAS*, 106(18):1–5, 2009.

[148] Y Hayashi. High resolution electron microscopy of a small crack at the superficial layer of enamel. *J Electron Microsc*, 43(6):398–401, 1994.

[149] D Bajaj and D Arola. Role of prism decussation on fatigue crack growth and fracture of human enamel. *Acta Biomater*, 5(8):3045–56, 2009.

[150] D Bajaj, A Nazari, N Eidelman, and D D Arola. A comparison of fatigue crack growth in human enamel and hydroxyapatite. *Biomaterials*, 29(36):4847–54, 2008.

[151] T Fett, S Fuenfschiling, M J Hoffman, R Oberacker, H Jelitto, and G A Schneider. R-curve determination for the initial stage of crack extension in si_3n_4. *J Am Ceram Soc*, 91(11):3638–42, 2008.

[152] S Fuenfschiling, T Fett, M J Hoffman, R Oberacker, H Jelitto, G A Schneider, M Haertelt, and Riesch-Oppermann H. Bridging stresses of R-curves silicon nitrides. *J Mater Sci*, 44(14):3900–3904, 2009.

[153] H Oezcoban, H Jelitto, and G A Schneider. Influence of finite notch root radius and optically determined crack length on the measured fracture toughness of brittle materials. *J Eur Ceram Soc*, 30(7):1579–83, 2010.

[154] B Kounga Nijwa, T Fett, D C Lupascu, and J Roedel. Crack-tip toughness of a soft lead zirconate titanate. *J Am Ceram Soc*, 86(11):1973–5, 2003.

[155] J Roedel, J F Kelly, and B R Lawn. In situ measurements of bridged crack interfaces in the scanning electron microscope. *J Am Ceram Soc*, 73(11):3313–8, 1990.

[156] F Meschke, P Alves-Ricardo, G A Schneider, and N Claussen. Failure behavior of alumina and alumina/silicon carbide nanocomposites with natural and artificial flaws. *J Mater Res*, 12(129):3307–15, 1997.

[157] F Meschke, O Raddatz, A Kolleck, and G A Schneider. R-curve behavior and crack-closure stresses in barium titanate and (Mg,Y)-PSZ ceramics. *J Am Ceram Soc*, 83:353–61, 2000.

[158] J N Goodier and F A Field. *Fracture of solids*. Interscience, New York, 1963.

[159] H G Hahn. *Bruchmechanik: Einfuehrung in die theoretischen Grundlagen*. Teubner, Stuttgart, 1976.

[160] G T Hahn and A R Rosenfield. Local yielding and extension of a crack under plane stress. *Acta Metall*, 13(3):293 – 306, 1965.

[161] D S Dugdale. Yielding of steel sheets containing slits. *J Mech Phys Solids*, 8(2):100–4, 1960.

[162] N I Muskhelishvili. *Some basic problems of the mathematical theory of the elasticity*. Noordhoff, Gronigen, 1953.

[163] J K Hobbs, C Vasilev, and Humphris A D L. Video afm - a new tool for high speed surface analysis. *Analyst*, 131:251–6, 2006.

[164] H H Xu, D T Smith, S Jahanmir, E Romberg, J R Kelly, V P Thompson, and E D Rekow. Indentation damage and mechanical properties of human enamel and dentin. *J Dent Res*, 77(3):472–80, 1998.

[165] N E Waters. *Some mechanical and physical properties of teeth*. In: The mechanical properties of biological materials. Cambridge University Press, Cambridge, 1980.

[166] B N Cox and D B Marshall. Concepts for bridged cracks in fracture and fatigue. *Acta Metall Mater*, 42(2):341–63, 1994.

[167] G C Sih. *Handbook of stress intensity factors*. Lehigh Univ. Press, 1973.

[168] A G Evans and R M McMeeking. On the toughening of ceramics by strong reinforcements. *Acta Metall*, 34(12):2435–41, 1986.

[169] T A Sikoryn and D W Hukins. Mechanism of failure of the ligamentum flavum of the spine during in vitro tensile tests. *J Orthop Res*, 8(4):586–91, 1990.

[170] S T Rasmussen, R E Patchin, D B Scott, and A H Heuer. Fracture properties of human enamel and dentin. *J Dent Res*, 55(1):154–64, 1976.

[171] S Bechtle, T Fett, G Rizzi, S Habelitz, and G A Schneider. Mixed-mode stress intensity factors for kink cracks with finite kink length loaded in tension and bending: application to dentin and enamel. *J Mech Behav Biomed Mater*, 3(4):303–12, 2010.

[172] A J Bushby and D J Dunstan. Plasticity size effects in nanoindentation. *J Mater Res*, 19(1):137–42, 2004.